POLITECNICO DI MILANO

Facoltà di Ingegneria Industriale

Corso di Laurea in
Ingegneria Meccanica

Control of segmented deformable mirrors for future large telescopes

Relatore: Prof. Francesco BRAGHIN

Co-relatore: Prof. André PREUMONT

Tesi di Laurea di:

Edoardo BELLONI Matr. 782714

Anno Accademico 2012 - 2013

Acknowledgements

First of all, I would like to express my gratitude to Professor André Preumont. Thanks for having accepted me at the Active Structure Laboratory (ASL) of Université Libre de Bruxelles, and for continuously challenging and guiding me through the topic of this thesis. His example taught me the meaning of doing research.

I'm grateful to all my colleagues at ASL. Special thanks to Renaud Bastais, my supervisor at ASL. Without his scientific and pedagogic competence, his meticulousness and willingness also, and in particular, during problematic situations, this work would be probably impossible to be completed. I am indebted to him for encouraging me, for all his precious remarks starting from the first concepts of optics until the last weeks of the thesis draft. It was a honor to work shoulder to shoulder with him, and his contribution to this thesis should not be forgotten.

It's a pleasure to thank Professor Francesco Braghin, supervisor at my home university Politecnico di Milano. Although from afar, his prompt help and remarks were always helpful and stimulating, also regarding matters not connected with this thesis.

Thanks to my family for the support, the patience and for more than can be expressed by words. To my mother and my father. To my brother. To my grandmother, my aunts, uncles and cousins.

I want to thank my friends. Paolo Barizza and all my friends of La Spezia. Thanks to my friends in Milano, they are too many to list here but I'm carrying them all in my heart. It's impossible then to forget my Erasmus mates in Bruxelles: I thank them for all the good times spent together and I'm looking forward to see them soon.

And last, but certainly not the least, thanks to Priscilla:

I wanna hurry home to you
Put on a slow, dumb show for you
And crack you up
So you can put a blue ribbon on my brain
God I'm very, very frightening
I'll overdo it
(The National - Slow Show)

Contents

List of Figures

List of Tables

Keywords

English

- Segmented mirror
- Piezoelectricity
- Active and adaptive optics
- Shape control
- Phasing of segments

Italiano

- Specchio segmentato
- Piezoelettricità
- Ottica attiva ed adattiva
- Controllo di forma
- Messa in fase dei segmenti

Abstract

English

Both space and ground-based modern telescopes need active control to achieve better image quality. It takes two different forms: *active optics* deals with the correction of the aberrations related to the shape and position of the mirrors; the goal of *adaptive optics* is to compensate the aberrations of the light beam due to atmospheric turbulence. Deformable mirrors are a widespread technology for active control in optics: their shape can be modified thanks to a network of suitable actuators, to compensate for aberrations by reflection.

The deformable mirrors considered in this text for applications for future telescopes need many degrees of freedom and high resonance frequencies, as well as reliability, low cost, high optical quality, ... To comply with all these requirements together, the concept of *segmentation* is used: instead of building a large, unique mirror, a set of co-phased smaller mirrors (segments) is preferred.

In this thesis, we first describe the prototype of an hexagonal segmented deformable mirror developed at Active Structure Laboratory of ULB and its numerical model. Then, the principles of control are presented: *morphing*, that is the local deformation of segments to compensate for the aberrations, and *co-phasing* of the segments, to achieve the continuity of the surface formed by the segments. These concepts are applied to two different approaches of control that are studied and compared numerically to understand the influence on the results of the actuator network and of the sensing method.

Finally, a parametric study is conducted to compare the performances and advantages of different configurations of deformable mirrors, starting from a single mirror and gradually increasing the degree of segmentation. This parametric study shows that the concept of segmented deformable mirror is an interesting alternative to the common architecture based either on a single deformable mirror or on a segmented mirror with only rigid-body actuation.

Italiano

Al giorno d'oggi nei telescopi spaziali e terrestri il controllo attivo è fondamentale per ottenere alta qualità delle immagini. Si può suddividere in due casi: l'*ottica attiva* si occupa di correggere le aberrazioni legate a forma e posizione degli specchi; l'obiettivo dell'*ottica adattiva* è compensare le aberrazioni del fascio di luce dovute alla turbolenza atmosferica. Gli specchi deformabili sono una tecnologia diffusa per il controllo attivo in ottica: la loro forma può essere modificata grazie ad una appropriata configurazione di attuatori, in modo da compensare le aberrazioni tramite la riflessione.

Gli specchi deformabili qui studiati, per applicazioni in telescopi di nuova generazione, necessitano di un alto numero di gradi di libertà ed alte frequenze di risonanza, ma allo stesso tempo di affidabilità, basso costo, alta qualità ottica, ... Per soddisfare tutte queste richieste, si utilizza il concetto di *segmentazione*: invece di costruire un grande ed unico specchio, si preferisce un insieme di specchi più piccoli (segmenti), coordinati tra loro.

In questa tesi, si descrive innanzitutto il prototipo di un specchio esagonale segmentato sviluppato presso il Laboratorio di Strutture Attive dell'ULB, e il suo modello numerico. Si presentano quindi i principi del controllo: *controllo di forma*, ovvero la deformazione locale dei segmenti per compensare le aberrazioni, e *messa in fase* dei segmenti, in modo che i segmenti formino una superficie continua. Questi concetti sono applicati a due differenti approcci al controllo, che sono studiati e analizzati numericamente per comprendere in che modo i risultati sono influenzati della rete di attuatori e del metodo di misura.

Infine viene condotto uno studio parametrico per mettere a confronto prestazioni e vantaggi di differenti configurazioni di specchi deformabili, partendo da un singolo specchio e alzando gradualmente il livello di segmentazione. Questo studio parametrico mostra che il concetto di specchio deformabile segmentato è una interessante alternativa alla comune architettura basata o su un singolo specchio deformabile o su uno specchio segmentato con con attuazione a soli moti rigidi.

Estratto in lingua italiana

Fondamenti di ottica

Per *telescopio* si intende un insieme di lenti o di specchi (talvolta coesistenti), che hanno lo scopo di ricevere un fascio luminoso e di estrarre da esso, in modo chiaro ed efficiente, l'immagine di un oggetto posto a grande distanza dall'osservatore. Grandezza, forma e posizione degli specchi vengono scelti in base a un'ottimizzazione tra costi, performance e realizzabilità. Più grande è lo specchio primario del telescopio (M1), maggiore sarà l'energia luminosa raccolta e sarà quindi più semplice osservare oggetti posti a distanza maggiore, ed in modo più nitido.

Per evitare aberrazioni nel fascio luminoso riflesso e conseguente decadimento della qualità delle immagini, forma e posizione degli specchi devono essere mantenuti con elevata precisione. Al giorno d'oggi, per avere standard qualitativi elevati nelle immagini fornite dai telescopi si fa largo uso del controllo attivo, che richiede una rete di attuatori e di sensori e si divide in due categorie: ottica attiva e ottica adattiva.

- L'*ottica attiva* può essere utilizzata per coordinare un insieme di specchi, ed anche per correggere le deformazioni dello specchio primario, permettendo di semplificare la struttura di supporto e il montaggio, riducendo di conseguenza i costi. Importanti poi le sue applicazioni nella correzione degli effetti dovuti al vento incidente sulla struttura, dei gradienti termici e della gravità. In generale possiamo affermare che si vanno a correggere difetti a bassa frequenza e con ampiezze (per telescopi di nuova generazione) fino a qualche millimetro.
- Con *ottica adattiva* si intende invece la correzione dei disturbi nel fascio luminoso dovuti alla turbolenza atmosferica. Essa è dunque più propria dei telescopi terrestri, piuttosto che di quelli spaziali. A differenza dell'ottica attiva il range di frequenze in cui opera è più elevato, mentre le ampiezze in gioco sono tipicamente nell'ordine del micrometro.

Come già accennato, lo specchio primario (M1) gioca un ruolo chiave per quanto riguarda le qualità del telescopio: il diametro D di M1 condiziona la risoluzione e il contrasto delle immagini, stabilendo un limite per l'oggetto identificabile posto più lontano. Obiettivo non trascurabile è poi focalizzare tutto questa luce entrante in una piccola area, per migliorare la qualità ottica. Specchi più grandi implicano strutture portanti più complesse, nonchè maggiormente affette da gravità e gradienti termici. Tutto ciò ha portato a sviluppare soluzioni innovative per le strutture, spesso di controllo passivo, come un opportuno sviluppo di sottostrutture o una scelta ottimizzata dei materiali.

La costante crescita del diametro dello specchio primario è andata incontro a un limite tecnologico: per diametri superiori ad 8 metri la realizzazione di un unico specchio risulta difficoltosa. Vari i problemi: qualità della superficie, frequenza propria bassa, trasporto, ... Per ovviare al problema, una diffusa soluzione è quella di ricorrere a **specchi segmentati**, ovvero comporre uno specchio di diametro richiesto utilizzando un insieme di piccoli specchi (possono avere varie forme, in questa tesi sarà analizzato uno dei casi più diffusi, cioè con geometria esagonale). In questo caso si deve ricorrere al controllo attivo per garantire la continuità dell'insieme degli specchi.
Come già detto, oltre al fatto di ricevere più luce ingrandendo il diametro dello specchio primario, va tenuta in considerazione la focalizzazione di tale fascio luminoso. In particolare esso, a causa di turbolenze atmosferiche (se si tratta di telescopi terrestri) o per imprecisioni dello specchio stesso (presenti in ogni tipo di telescopio), va corretto e mantenuto in un range qualitativo accettabile. Una diffusa tecnologia per realizzare tali correzioni, che fa parte del controllo attivo, è quello degli **specchi deformabili**. Il concetto base di tale tecnologia (più avanti si vedrà come è applicato in questa tesi) è quello di servirsi di un insieme di attuatori, di svariata tipologia, per ottenere deformazioni locali della superficie dello specchio. Queste deformazioni hanno lo scopo di variare il fascio di luce riflesso, incrementandone la qualità.

Qualità ottica

Introduciamo ora due indicatori di qualità del fronte d'onda: l'ampiezza picco-valle (**PV**) e l'errore quadratico medio (**RMS**, root mean square). Il primo fornisce una stima della differenza tra il picco massimo e minimo ottenuti nella superficie: l'errore PV sarà quindi la differenza locale tra i picchi risultanti nella superficie ottenuta e quella di riferimento. Si noti che questo parametro non fornisce indicazioni sulla curvatura della superficie e non è influenzato dall'area sulla quale è calcolato. L'errore RMS fornisce invece una stima basata su un set di punti posti sulla superficie, per i quali viene di fatto calcolata la deviazione standard. E' possibile e conveniente esprimere l'errore del fronte d'onda come combinazione lineare di opportuni *polinomi di Zernike* (polinomi definiti su una superficie circolare e molto utilizzati in ottica, si veda la trattazione in Appendice A e alcune applicazioni nel Capitolo 2).
Anche l'atmosfera contribuisce al decadimento della qualità ottica del fascio: ciò è dovuto agli effetti della turbolenza negli strati atmosferici. Il modello di turbolenza qui utilizzato si rifà alla teoria di Kolmogorov. Ancora una volta i polinomi di Zernike sono utili: possono essere sfruttati per esprimere il fronte d'onda e per stimare gli effetti della correzione attuata dal controllo attivo (si veda il Capitolo 2).

Gli strumenti di misura

Il controllo applicato al nostro sistema opera su due aspetti differenti: controllo della forma dello specchio per compensare aberrazioni ed effetti della turbolenza, e coordinazione tra i segmenti per garantire la continuità della superficie. Per soddisfare tali requisiti sono necessari dei sensori per creare un anello in retroazione.

Il sensore **Shack-Hartmann** (SH) è un sensore ottico molto utilizzato, e fornisce informazioni sul fronte d'onda in maniera semplice ed efficiente: esso stima il gradiente locale del

fronte d'onda, misurato su un insieme discreto di punti. Acquisisce tramite una telecamera i punti in cui si focalizza il fascio luminoso attraverso un set di micro-lenti: il punto di convergenza del fascio attraverso una lente dipenderà dalla forma locale del fronte d'onda in corrispondenza di ciascuna lente. Tramite questo spostamento del punto di convergenza del fascio rispetto al centro di ogni lente è possibile ricostruire i gradienti locali della superficie.

Il sensore visto sopra è utilizzato (in questa tesi) per eseguire il controllo di forma. E' necessario però servirsi di un altro sensore per coordinare tutti i segmenti tra loro e realizzare una superficie continua. Si analizzano due casi differenti.

Il primo tipo di sensore utilizzato è detto **Edge Sensor** (ES). A fronte di diverse tecnologie costruttive (capacitivo, piezoelettrico,...), il concetto di base resta il medesimo. Tale sensore è composto da due parti, una posta sul bordo di un segmento e l'altra sul bordo del segmento adiacente: ciò che si misura è la distanza relativa tra le due parti (se ad esempio viene utilizzato un condensatore, la distanza tra le due piastre genera una differenza di potenziale proporzionale alla distanza tra esse). Sensore molto semplice ma non utilizzabile nel nostro sistema a causa di dimensioni e peso, verrà comunque sfruttato come termine di paragone per il secondo sensore che andremo ad utilizzare.

Il secondo tipo di sensore utilizzato per coordinare i segmenti tra loro è il **Zernike Phase Contrast Sensor** (ZPCS). Questo sensore è di tipo ottico (quindi non crea problemi di carico sui segmenti ed è di minore ingombro) e si basa su tecniche interferometriche: di fatto si ricava la distanza tra i bordi di due segmenti adiacenti sfruttando (con una relazione proporzionale) la differenza di fase tra due segnali, riferiti ciascuno ad un segmento. Per quanto riguarda l'implementazione di tale sensore nel nostro sistema, si suppone di conoscere il valore di questa differenza in 8 punti su ciascun bordo dei segmenti. Viene calcolato il valor medio di essi, che sarà quindi utilizzato nell'algoritmo di controllo. Vari metodi per il calcolo della media sono stati testati (in particolare con più punti di misura e con due valori medi per bordo), ma non sono state rilevate importanti differenze con la configurazione sopra descritta, che verrà pertanto utilizzata in questa tesi.

Il sistema

Ci si propone ora di presentare il modello (con relativo prototipo) analizzato in questa tesi. Per maggiori informazioni, immagini e risultati sperimentali si faccia riferimento al Capitolo 3.

Il punto di partenza è uno specchio circolare di Silicio: su un lato di esso viene applicato un sottile rivestimento in Alluminio al fine di garantirne la conduttività. Sul lato con il rivestimento, viene incollata una rete di attuatori piezoelettrici esagonali (nel prototipo sono 37). Proprietà fondamentale dei materiali piezoelettrici è quella di rispondere con una deformazione a fronte di una applicazione di tensione (per maggiori dettagli si veda Appendice C): tale rete di attuatori sarà allora utilizzata per creare opportune deformazioni locali della superficie dello specchio. Su ogni attuatore è, in un secondo momento, saldato un cavo di collegamento alla rete elettrica, e sono inoltre previsti 3 collegamenti a terra per poter esercitare una differenza di potenziale.

L'incollaggio degli attuatori avviene mediante particolari colle, dispensate con una pipetta calibrata. Inoltre lo specchio durante tale operazione è mantenuto su una superficie curva.

A questo punto del processo, lo specchio con gli attuatori incollati viene tagliato: si utilizza un processo laser per incidere la superficie, ma la rottura finale è eseguita a mano. La forma del segmento risultante è, come precedentemente accennato, esagonale.
Ogni segmento è quindi connesso alla struttura di base tramite 3 appoggi. Essi non sono solo un supporto, ma trasmettono (tramite opportuna attuazione) moti rigidi allo specchio. Sono incollati anch'essi, e la loro posizione viene scelta in modo da massimizzare la prima frequenza propria del sistema. Inoltre il particolare montaggio scelto permette di realizzare un sistema di vincoli isostatico.

E' stato sviluppato un modello ad elementi finiti (semplificato) del sistema in analisi. Il software utilizzato per le simulazioni è SAMCEF. Tale modello è stato inoltre validato confrontando i risultati delle simulazioni FEM con una formula analitica (*formula di Stoney*) per il calcolo della curvatura di una piastra sottoposta a un carico dato da un sottile film applicato: si ottiene un'ottima corrispondenza tra i due approcci per il sistema studiato in questa tesi (differenza inferiore all' 1.5%).

La verifica sperimentale viene effettuata su un prototipo di $90mm$ di diametro. Viene applicata di volta in volta una tensione di $60V$ ad un attuatore piezoelettrico, mentre tutti gli altri sono mantenuti a $0V$. I risultati (mostrati per una serie di attuatori nel Capitolo 3) sono abbastanza concordi con il modello numerico. Le differenze possono essere imputate a differenze di caratteristiche meccaniche tra i materiali reali e quelli simulati, imperfezioni nell'elettronica di controllo e infine non precisa modellazione delle condizioni di bloccaggio del segmento (condizioni al bordo).

Le tecniche di controllo: controllo di forma

Analizziamo ora il primo tipo di controllo che opera sul sistema, ovvero il controllo di forma: l'obiettivo è calcolare i voltaggi da applicare agli attuatori (di ogni tipo) per cambiare forma e orientazione di ogni segmento *indipendentemente* in modo da ricreare una specifica superficie obiettivo.
L'equazione base lega i voltaggi applicati agli attuatori alle deformazioni sulla superficie:

$$w = \mathbf{J}v$$

dove w è il vettore delle misure fornite dal sistema di misura, v è il vettore dei voltaggi e $\mathbf{J}$ è la matrice (*Jacobiano*) che lega le due quantità, e si noti che, in generale, è una matrice rettangolare (ovvero numero di misure e numero di attuatori sul segmento sono differenti).

Note misure e Jacobiano, bisogna ricavare i voltaggi da applicare. Per farlo è necessario invertire la matrice Jacobiana: essendo essa rettangolare è necessario calcolare la matrice pseudo-inversa. Esistono metodi differenti per eseguire il calcolo, in questa tesi si utilizza una tecnica basata sulla *Singular Value Decomposition* (SVD): tale algoritmo scompone una matrice in un prodotto tra 3 matrici (il simbolo $\mathbf{J}^+$ indica la matrice pseudo-inversa).

$$\mathbf{J} = \mathbf{U}\Sigma\mathbf{V}^T \;\rightarrow\; \mathbf{J}^+ = \mathbf{V}\Sigma^{-1}\mathbf{U}^T$$

Ha inoltre un importante significo fisico: le colonne di $\mathbf{U}$ sono i modi orto-normalizzati dei sensori, le colonne di $\mathbf{V}$ sono i modi orto-normalizzati degli attuatori e la matrice diagonale

Σ^{-1} contiene l'inverso dei valori singolari associati a ciascun modo, σ_i^{-1}.

Avere accesso diretto ai valori singolari della matrice permette di vedere quali modi sono maggiormente influenti, e consente di filtrare una parte di essi per migliorare il condizionamento della matrice, fatto che si rivelerà di importanza fondamentale ai fini del controllo e dei risultati ottenuti.
Si può scrivere la matrice pseudo-inversa come:

$$\mathbf{J}^{+} = \sum_{i=1}^{r} \sigma_i^{-1} u_i^T v_i$$

dove r è il rango della matrice Jacobiana. Con questa formula è possibile trascurare dalla somma uno o più valori singolari, non considerati rilevanti poichè associati a modi con scarsa autorità. Di fatto si analizza la distribuzione dei modi normalizzati σ_i/σ_{max}, eliminando quelli al di sotto di un certo valore limite scelto di volta in volta a seconda del sistema, del tipo di controllo e delle performance richieste.

Le tecniche di controllo: coordinamento dei segmenti

Coordinare, mettere in fase tutti i segmenti che compongono lo specchio per creare una superficie continua è il secondo passo del controllo. In particolare il termine che più va compensato per garantire la continuità della superficie è la differenza tra i segmenti in direzione normale al piano di riferimento, il cosiddetto piston, usando il linguaggio dei polinomi di Zernike. Solo in un secondo momento viene migliorata anche la pendenza globale di ogni segmento per ottimizzare la continuità (sempre usando i polinomi di Zernike tali termini sono detti tip-tilt). Come spiegato poco sopra, si utilizzerà lo Zernike Phase Contrast Sensor (ZPCS) per eseguire questo step del controllo. Svariate prove sono state effettuate anche seguendo l'approccio con edge sensors, ma in generale restituendo risultati meno performanti.

In questo caso l'equazione fondamentale è:

$$S_s = \mathbf{J}_s^{gl}\, v^{gl}$$

dove S_s è il vettore con i segnali relativi, associati ad ogni bordo lato di ogni segmento, v^{gl} contiene i voltaggi associati a tutti gli attuatori e $\mathbf{J}_s^{gl}$ è la matrice Jacobiana generica che li lega. Dallo Jacobiano è possibile estrarre una nuova matrice Jacobiana che si riferisce al solo termine piston (si tratta in questo caso di matrici globali, che comprendono quindi tutti i segmenti insieme, a differenza del controllo di forma, che opera a livello locale). Eseguendo la matrice pseudo-inversa di questo nuovo Jacobiano otteniamo i valori di tensione che servono per correggere i voltaggi applicati agli attuatori lineari in modo da compensare il termine piston.
In un secondo momento, è possibile affinare ulteriormente questi nuovi valori di tensione correggendo anche i termini tip-tilt. La procedura è simile alla precedente, cambia di fatto solo il nuovo Jacobiano (si ottiene tramite opportune combinazioni lineari di alcune colonne di $\mathbf{J}_s^{gl}$).

Applicazioni del controllo

Vediamo una prima applicazione dei concetti teorici del controllo visti nei punti precedenti. Si suppone di utilizzare un sensore *ideale* in grado di fornire i **valori di spostamento** per un set di punti posti sui segmenti. Con tali valori è possibile calcolare lo Jacobiano per il controllo di forma e procedere con la strategia di controllo precedentemente descritta.
Molto importante il ruolo del filtraggio dei valori singolari della matrice pseudo-inversa (si ricorda che sono facilmente ricavabili dalla matrice diagonale Σ, e che vengono normalizzati). Si dimostra matematicamente che per tale tipo di controllo è possibile trovare un livello per il filtraggio (nel nostro caso si filtrano valori singolari normalizzati inferiori a 10^{-3}) in grado di ridurre il range di voltaggi da applicare agli attuatori, e al contempo di mantenersi su bassi livelli di errore RMS: è un valore di ottimo. Importante caratteristica di questo tipo di sensore è che tale valore di ottimo risulta piuttosto robusto alle variazioni.
Questo approccio è stato testato per molte superfici di riferimento, solitamente scelte tra i primi polinomi di Zernike. Da sottolineare anche l'uso di una superficie turbolenta, creata tramite una opportuna combinazione di modi di Zernike: costituisce un valido esempio realmente esistente di applicazione di correzione del fronte d'onda.
L'approccio (si faccia riferimento al Capitolo 5) è presentato per una configurazione con 7 segmenti esagonali, ma è stato verificato numericamente che si può applicare a configurazioni con più segmenti.

Si è poi analizzato il caso di controllo mediante l'uso di un sensore Shack-Hartmann (SH): questa volta l'output del sensore non è un vettore di spostamenti, ma **curvature locali**, gradienti. Importante la scelta della griglia di micro-lenti del sensore: se il numero di tali lenti non è sufficiente, possiamo incontrare fenomeni di sotto-campionamento per alcuni segmenti che compongono il sistema. Il controllo ne risente, e anche il condizionamento della matrice Jacobiana ne è affetto. In alcuni casi si può anche ottenere un effetto di aliasing spaziale, che provoca errate ricostruzioni della superficie misurata.
Importante caratteristica del sensore SH è che non è in grado di rilevare il termine piston: ciò si traduce nel fatto che lo Jacobiano presenterà un valore singolare associato a tale termine pari a 0. Ciò rende pesantemente mal condizionata la matrice, e per eseguire l'inversione è in ogni caso necessario filtrare tale valore.
Importante anche in questo caso è il filtraggio dei valori singolari (il valore singolare pari a 0 descritto sopra viene sempre considerato filtrato in ogni caso). Per questo tipo di sensore non si riesce a trovare un valore robusto per il filtraggio dei valori singolari (fatto probabilmente dovuto al numero di punti di misura molto inferiore rispetto al caso precedente). Una strategia che consente di abbassare i voltaggi applicati e al contempo mantenere basso l'errore RMS è quella di impostare il filtro poco sotto l'ultimo valore (non nullo) del segmento centrale: ciò consente di preservare tutti gli autovalori del segmento centrale, mentre esclude parte dei valori singolari dei segmenti esterni. Si dimostra (anche qui è stato fatto su varie superfici, tra cui quella turbolenta) che la procedura è valida anche per più di 7 segmenti.

Studio parametrico

Fino ad ora si è analizzato un singolo sistema per quanto riguarda performance e sistemi di controllo. Quello che ci si propone infine di fare, mantenendo costanti il diametro della pupilla ottica, il numero di gradi di libertà del sistema e la superficie obiettivo, è vedere come si modi-

ficano le performance del sistema cambiando numero di segmenti e di attuatori per segmento. Come superficie obiettivo viene scelta la superficie turbolenta descritta precedentemente. Le configurazioni studiate passano da un singolo specchio con una ampia rete di attuatori ad un insieme di segmenti dotati di puro moto rigido (quindi privi di attuatori). Come strumento di misura per il controllo di forma viene scelto il sensore SH, mentre per mettere in fase in segmenti si usa lo ZFCS.

Si vede dai risultati numerici (Capitolo 6) che per configurazioni con molti segmenti il trend per l'errore RMS è crescente. Tali configurazioni hanno però un vantaggio: avendo dei segmenti con dimensioni inferiori presentano la prima frequenza di risonanza ad un livello più alto. Tale parametro riveste un ruolo importante (utile per il controllo e per motivi strutturali), e porta a giudicare non buone le scelte con un singolo (o pochi) specchi perchè la prima frequenza propria è troppo bassa.

Anche altri parametri variano tra una configurazione e l'altra. Un esempio analizzato in questa tesi è il calcolo del numero di Strehl. Parametro molto importante per gli astronomi (ma non comodo da utilizzare in quanto fortemente dipendente dalla lunghezza d'onda della luce che si sta analizzando), identifica la quantità di energia riflessa e fornisce al contempo informazioni sulla qualità dello specchio (si faccia riferimento al Capitolo 6 per i risultati numerici).

Capitolo 1

Introduction

1.1 Basics

A telescope is an arrangement of lenses, mirrors, or both that collects light, and is designed to image objects located at large distances from the observer, in order to allow astronomers to study the light beam in an efficient way. The size, shape and relative position of the mirrors are defined from a trade-off study between cost, performance and feasibility. The telescope aperture, that is the primary mirror (M1), collects the light energy. The larger the aperture, the more energy gathered and the fainter the objects that can be observed.

During operation, the shape and position of the mirrors must be maintained with a high precision, that is solely a function of the wavelength of interest (whatever the diameter): errors in the shape and position result in aberrations that modify the wavefront, which leads to a degradation of the quality of the observations. Errors in the output wavefront may arise from several different sources. Typical sources of these errors are: design and manufacturing process (but also maintenance and aging), gravity, temperature changes (which induce dilatations and turbulence due to the thermal exchange between the mirror and the air), wind effects on the structure and tracking errors. This is an overall list of the most relevant ones, a more detailed description is provided in Chapter 2. Each source has a typical bandwidth and amplitude. Referring to a wavelength λ, Table 1.1 summarizes all these effects.

1.2 Active and adaptive optics

The goal of active control, in both cases of active and adaptive optics, is the automatic reshaping of the wavefront, and this requires sensors and actuators. Active control monitors the respective position of individual optical elements (or measures the errors in the final wavefront) and then applies correction adjusting the position. So, active optics control can be used to coalign and cophase an array of mirror segments, as in the Keck telescopes. It's only thanks to active optics if these particular telescopes are feasible. Active control can be applied to correct deformations of the primary mirror, thus permitting to use thinner, hence lighter, mirrors supported on lighter, hence less expensive, mechanical mounts.
A further advantage is the ability to correct the effects of wind buffeting. In the modern approach of dome-seeing control, the wind can flow across the mirror surface to maximize heat exchange and thus reduce temperature differences. In fact temperature variations in

large telescopes strongly affect the overall quality of the telescope image basically because structural deformations induced by temperature gradients may be transferred to the mirrors and because temperature differences of the mirrors with respect to the ambient temperature lead to convection disturbances causing serious degradation of the image. The drawback is the effect of wind buffeting of the telescope, an effect that active control can compensate if the frequency bandwidth is high enough.

Source	Bandwidth [Hz]	Typical amplitude
Design, manufacture, operation, maintenance and aging	$[\,0\,,\,10^{-6}\,]$ (fixed$\rightarrow$ weeks)	$\gg 100\lambda$
Gravity (pointing and tracking) and thermal deformations	$[\,10^{-4}\,,\,10^{-3}\,]$ (hours $\rightarrow$ minutes)	$\gg 100\lambda$
Wind-induced deformations	$[\,10^{-2}\,,\,10\,]$	$\gg 100\lambda$
Site, dome and mirror seeing	$[\,10^{-4}\,,\,10\,]$	$< 20\lambda$
Tracking errors (vibrations)	$[\,1\,,\,10^{2}\,]$	

Tabella 1.1: This table (adapted from [42] and [41]) shows the bandwidth and the typical amplitudes of the main sources of image degradation. Phenomena relying on elasticity of massive solids, like gravity and temperature, are slower processes involving larger amplitudes and lower spatial frequencies. The seeing effect is more related to the physics of air, so on the contrary it involves shorter time constants and smaller amplitudes, but a very extended spatial frequency range.

If the wavefront surface can be corrected quickly enough, it's also possible to reduce or eliminate the effects of atmospheric turbulence: in this case we call this approach adaptive optics (an example of feedback control loop for adaptive optive can be found in [23]).
To summarize, one can say that [[3],[1]]:

- *active optics* generally refers to the figure control of optical elements at low bandwidth (DC to a few Hertz) to correct residual aberrations, gravity and thermal effects. Typical aberration amplitudes up to a few millimeters are expected for future ELTs (see further in this chapter);
- *adaptive optics* refers to the correction of high-frequency wavefront disturbances (above a few Hertz) such as those created by atmospheric turbulence. Typical aberration amplitudes up to a few microns are expected for future ELTs.

Figure 1.1 shows the typical bandwidths for the control. As already mentioned, active optics will correct aberrations up to a few millimeters in future ELTs, while adaptive optics will correct aberrations up to a few microns.

1.3 Telescopes and active control

This section mainly refers to [1], [3] and [37].

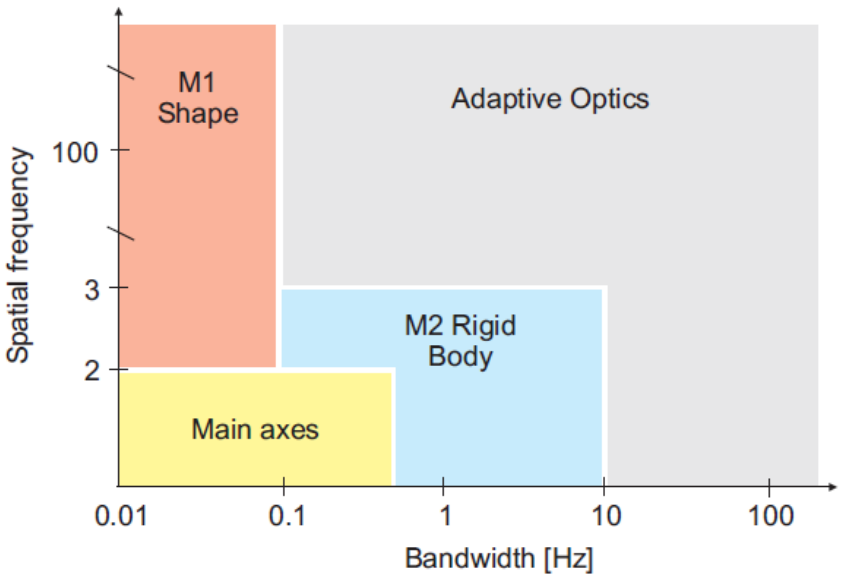

Figura 1.1: Temporal and spatial frequency distribution of the various control layers of a large telescope [1].

1.3.1 Historical background

Astronomy needs observations and instruments to really exploit the full potential of the sky: most part of astronomic discoveries would be impossible by naked-eye.
During the XVI^{th} century the first refracting telescope was created, and later improved by Galileo. That instrument allowed to push back the limits of observation of objects in the sky, by focusing more light than what the naked eye is capable of, and by magnifying the image. Around 1670 Isaac Newton devised the first refracting telescope, based on the use of a parabolic mirror, exempt of chromatic aberrations (that are typical of refractive elements). The primary mirror (M1) has a leading role for the performances of telescope: the diameter D of M1 affects the resolution and contrasts characteristics of the images formed by a telescope in ideal conditions. Moreover the effective area of M1 limits the brightness of the faintest object that a given telescope can observe. For apertures larger than 1m the reflecting telescopes have proved the most efficient.
As the optical elements grew up in size, their support structure also became larger, leading to an increase in its sensitivity to changes of gravity and temperature. These effects encouraged the development of innovative solutions, often *passive*, like new designs for sub-structures or an optimized choice of materials. The challenge is not only to collect more light (so, to build bigger telescopes), but also to focus this light in a smallest area, in order to get an improved optical accuracy.

1.3.2 Modern-days telescopes

The orientation of telescopes of the *altitude-azimuth* type (Figure 1.3) is based on a vertical (azimuth) axis and on a horizontal (altitude or elevation) axis. The rotation of the axes at variable speed, non-linearly dependent on telescope's orientation, makes the tracking intrinsi-

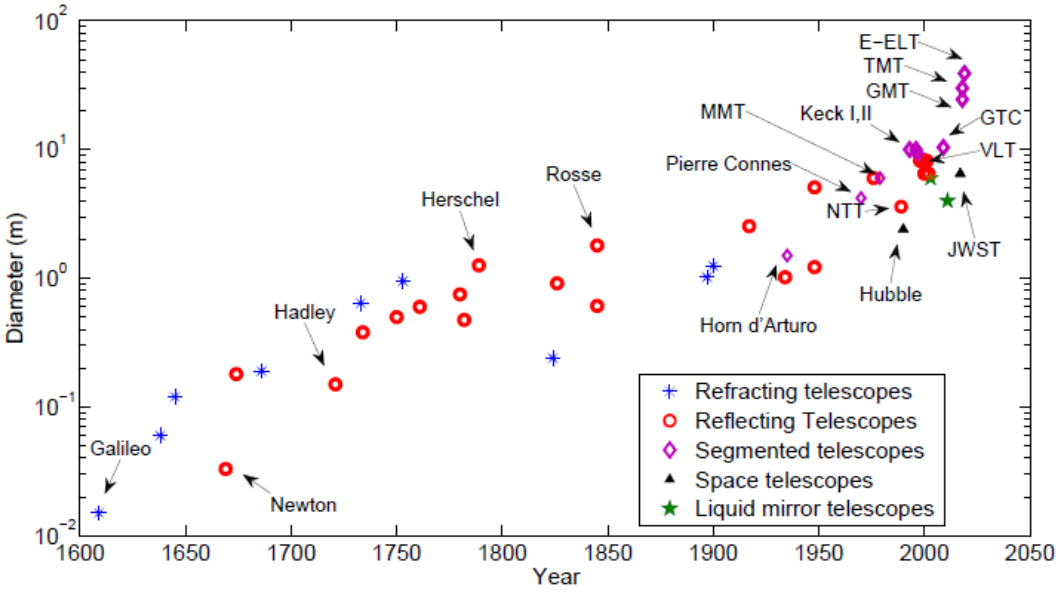

Figura 1.2: Evolution of telescope aperture diameter in time [37].

cally more complicated. Computer control has avoided this drawback, and the more compact and lighter structure implies a significant cost saving with respect to equatorial type. Moreover, the implementation of feedforward corrections to correct in a continuous way the light beam (via lookup tables) is easier, because the orientation of altitude and azimuthal axes do not change with respect to the orientation of gravity field.

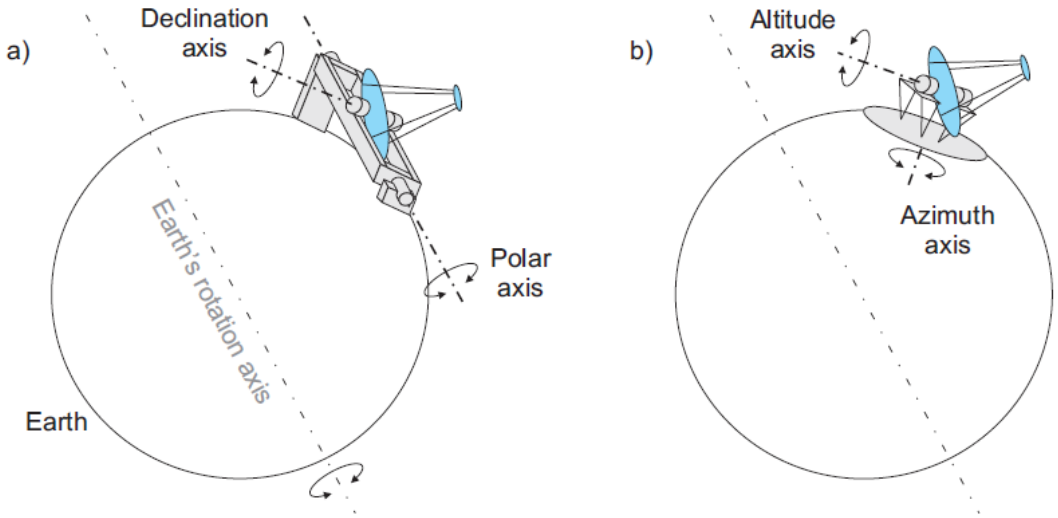

Figura 1.3: (a) Equatorial mount - (b) Altitude-Azimuth mount [1].

Before 1980, the biggest telescopes were of *equatorial* type (Figure 1.3), in which the initial pointing towards an object is allowed by rotations around the polar axis (parallel to Earth rotation axis) and around the declination axis (perpendicular to the polar axis). So, only with the rotation around the polar axis, at constant speed, it was possible to compensate the Earth rotation and to do a good tracking of objects in the skies. In telescopes of growing dimensions, this technique, while elegant, is unpractical: the biggest problems are related to the heaviness and to the impossibility of external disturbances correcting.

In the 1980s and 1990s, many technological advances have been made that allowed scientists to build larger telescopes. We can mention: computerized design (CAD), faster and improved optical figuring techniques, a faster focal ratio of the primary mirrors for smaller domes and buildings and the use of the altitude-azimuth configuration to reduce the mass and cost of telescope mounts.

While building a primary mirror with a diameter of 3.5m, the limits of passive techniques became evident, mainly from the point of view of the required optical tolerances. In fact, complex periodical readjustments of mirrors became necessary and they even took weeks to be completed. The goal of *active optics* is to automate that optical maintenance procedure, during observations, on much shorter time scales (from a few tens of seconds to a few minutes).

This technology has been tested for the first time on the 3.5 m primary mirror of the New Technology Telescope in 1989. The fundamental advantage of active optics implementation was that the residual intrinsic stiffness, which was required in passive telescopes to cope with the inaccuracies of the forces applied by the self-balanced passive supports, could now be reduced even further, which made the fabrication of telescopes with mirror diameters of 8 m feasible and affordable. It also allowed a significant relaxation of the requirements on the low spatial frequency quality of the meniscus mirrors made active, letting the manufacturer focus on mid- and high spatial frequencies that also are of practical importance.
Finally, adaptive optics is to be able to correct optical aberrations induced by the continuous local changes in the index of refraction of the atmosphere.

1.3.3 Segmented mirrors

The successful results of the technology developed for the NTT served as the basis for the design of the Unit Telescopes of ESO's Very Large Telescope (VLT): four active telescopes with a M1 of 8.2m (completed successively between 1998 and 2001). Building a giant telescope from a monolithic mirror presents many difficulties. These difficulties typically grow rapidly with the increasing size, and quickly make monolithic mirrors unpractical.
One solution to build telescopes with primary mirror diameters larger than 8 meter is to construct segmented primary mirrors. Segments are much easier to fabricate, transport, install, and maintain than large monolithic mirrors. Segments in the 1- to 2-m-diameter range can be designed to exhibit individual deformation under gravity lower than optical tolerances, while still providing a mass per unit surface much lower than that of equivalent monolithic mirrors. However, active control is required to maintain the overall shape and continuity of the surface formed by the segments due to the deformations of the supporting structure. So new problems arise, like diffraction effects due to gaps between segments edges and the increasing complexity

of control in view of the augmented number of degrees of freedom.

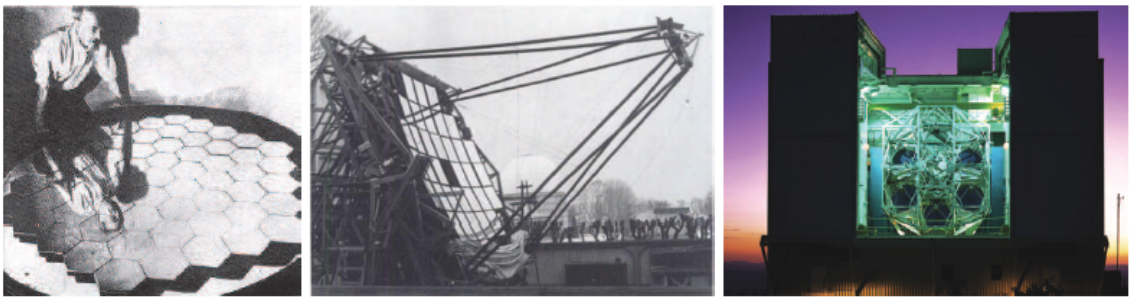

Figura 1.4: The first three segmented telescopes: the mirror of Horn d'Arturo, the segmented telescope of Pierre Connes and the MMT [37].

Different attempts to build segmented telescopes had been undertaken before reaching good results (Figure 1.4):

- in 1932, Horn d'Arturo in Italy made a 1.5 m mirror, which could only be used facing zenith
- Pierre Connes in France made in the seventies a 4.2 m segmented mirror telescope for infrared astronomy. Unfortunately, the optical quality was too low to be useful for astronomy.
- The MMT (Multiple Mirror Telescope), before the conversion of its primary mirror to a monolithic one, has been in operation between 1979 and 1998 with 6 mirrors, each with a diameter of 1.8 m.

One of the the most sophisticated segmented mirrors technology implementation is in the optical/near IR Keck II telescope (1996). With an effective aperture of approximatly 10m, the primary mirror is made of 36 hexagonal 1.8m-diameters segments. Each segment presents 3 actuators to correct the position (piston and tilts) and a set of sensors to measure the relative normal displacements between two adjacent sensors.
The Southern African Large Telescope, which saw first light in 2005, uses a rectangular segmented primary mirrors of 11x9.8 meters, made up of 91 hexagonal segments.

1.3.4 Deformable mirror

Deformable mirrors (DM) are one of the most mature means of wavefront correction in Adaptive Optics. This concept could be applied to a big number of different technologies, moving from micro-electromechanical devices (MEMS) with only a few *mm* of diameter to large secondary mirrors larger than 1 meter. Their actuators can be magnetic, electrostatic or piezoelectric.
Bimorph mirrors are formed by two or more layers of different materials. Two (or more) active layers, each coated by electrodes on both faces, are bonded together, and an electrical field E is applied through them in the direction perpendicular to the plane of the mirror. With a suitable choice of polarization direction and electrodes connectivity, it is possible to impose in-plane elongations in opposite directions for the two active layers. The compatibility of the

displacements at the interface will induce the bending of the bimorph mirror. The out-of-plane bending of the mirror originating from in-plane actuation can also be effectively achieved by utilizing one active layer adherent to a passive substrate. That's the *monomorph configuration*, which preserves the advantages of the previous one, that is simplicity, low-cost, robustness and low weight. The production of monomorph mirrors becomes particularly interesting, due to its greater simplicity, when the active layer consists of a thin film deposited on the back of an optical substrate.

To characterize the main concepts it's necessary to introduce the most important parameters of a DM [30].

- **Number of Actuators:** the number of actuators, or number of degrees of freedom (N), establishes the spatial resolution of a DM and the complexity of the shape that it is able to generate. The bigger the diameter D of the primary mirror, the numerous the required actuators. On the contrary the number of actuators decreases with the wavelength λ. For the particular case of Adaptive Optics this relation stands:

$$N \propto \frac{D^2}{\lambda^{12/5}} \tag{1.1}$$

  The first deformable mirror used in astronomy was installed at the ESO 3.6 m telescope: it possessed only 19 actuators for performing corrections in the infrared.

- **Stroke:** it's the maximum deformation of a deformable mirror. The required stroke is not dependent on the wavelength of observation and increases with the size of the primary mirror. The stroke of a DM is strongly related to the actuation principle and the boundary conditions of the DM.

- **Size:** a collimated beam of light with the diameter of the primary mirror, D, is transformed in a collimated beam of light with the diameter of the deformable mirror D_{ap}, by means of the optical train of the telescope. Figure 1.5 which refers to a refractive telescope, totally equivalent to a reflective one for this purpose, illustrates the concept of *Lagrange Invariant* (see [39]).

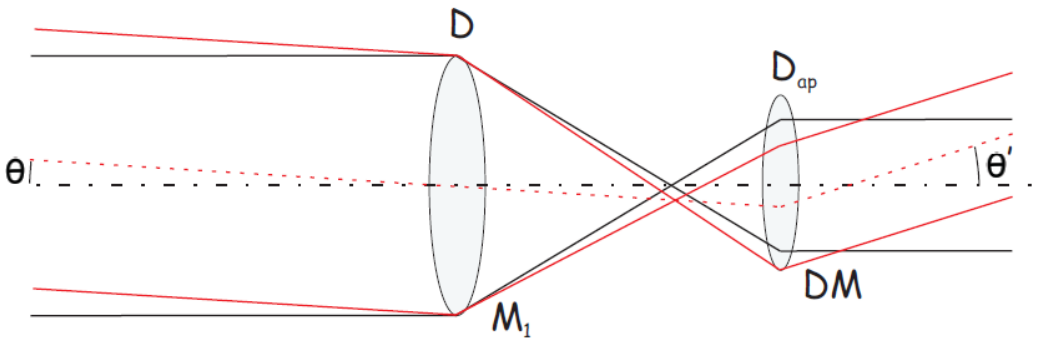

Figura 1.5: Magnification of the incidence angles due to Lagrange Invariant [30].

When applied to a telescope, it states that the product of the deviation angle θ (with relation to the optical axis), and the diameter of the collimated beam remains constant, therefore:

$$\theta D = \theta' D_{ap} \tag{1.2}$$

The maximum deviation θ accepted by the telescope defines its Field of View (θ_{max}).

$$\theta'_{max} = \theta_{max} \frac{D}{D_{ap}} \tag{1.3}$$

A lower limit to the DM diameter is imposed by the design of the optical train and the packing of all the components, which becomes really complicated for high deviation angles, θ'. Similarly, increasing the size of M_1 proportionally increases the minimum acceptable diameter of the DM.

- **Temporal Bandwidth:** the bandwidth of correction required by the atmospheric turbulence depends only on the wavelength of observation and on the speed of the wind. In the visible it can attain about 400 Hz and in the NIR 60 Hz (see [30, 32-34]). Guaranteeing that mechanical resonances remain high enough and providing enough damping, it's possible to passively achieve a high bandwidth of the deformable mirror.
- **Hysteresis and linearity:** the linearity of a DM can always be improved by calibration based on a lookup-table. Hysteresis, a significant effect in PZT actuators, is automatically corrected in closed-loop despite involving some loss of bandwidth.

1.3.5 Extremely Large Telescopes

On April 1 2009, the *Thirty Meters Telescope* (TMT, see Figure 1.6 and [6]) officially entered in early construction phase and is expected to see first light in 2018, on Mauna Kea, in Hawaii.

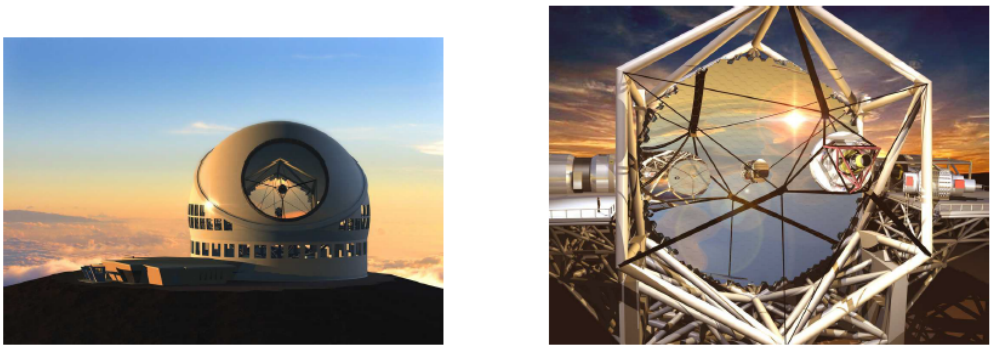

Figura 1.6: The TMT telescope on Mauna Kea, Hawaii. On the right the segmented primary, the secondary and the tertiary mirrors [38].

The optical design of the telescope is a folded Ritchey-Chretien (it has a hyperbolic primary mirror and a hyperbolic secondary mirror designed to eliminate optical errors like coma, see Figure 1.7).

The thirty meter primary mirror consists of 492 hexagonal segments with diameters of 1.44 meter from corner to corner. The segments are closely spaced, with gaps between the segments of only 2.5 mm. The secondary mirror has a diameter of 3.1 meters and converts the focal ratio of 1 of the primary mirror to a focal ratio of 15 for science instruments. The elliptical tertiary mirror has diameters of 3.6 and 2.5 meters. The M3 mirror can be rotated around a vertical axis to direct the light beam into the scientific instruments mounted on the Nasmyth Platforms.

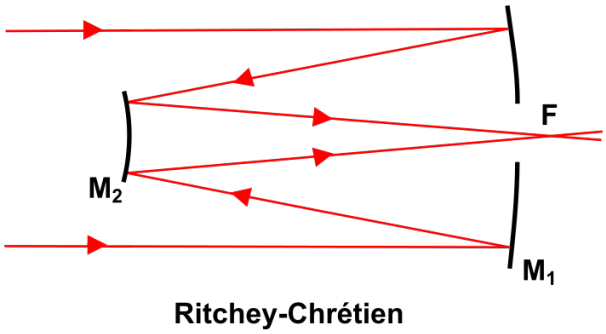

Figura 1.7: The Ritchey-Chretien configuration for telescopes [31].

The design of the Giant Magellan Telescope (GMT, see Figure 1.8) is unique within the class of Extremely Large Telescopes.

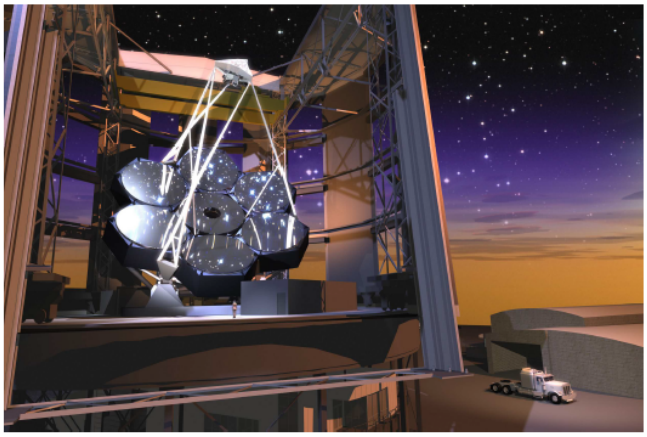

Figura 1.8: The GMT and its primary mirror [10].

The optical design is based on a Gregorian telescope (Figure 1.9) with a primary mirror made up of six off-axis circular mirrors and a central on axis mirror. This Gregorian telescope (Figure 1.9) consists of two concave mirrors; the primary mirror (a concave paraboloid) collects the light and brings it to a focus before the secondary mirror (a concave ellipsoid) where it is reflected back through a hole in the center of the primary, and thence out the bottom end of the instrument where it can be viewed, in the GMT with modern display devices, in

the past with the aid of the eyepiece (or ocular lens, is a type of lens that is attached to a variety of optical devices, placed near the focal point of the objective to magnify this image, where the amount of magnification depends on its focal length). Each circular segment has a diameter of 8.4 meters. The equivalent collecting area is that of a 21.4 meters telescope and the resolving power is that of a 24.5 meters aperture. The secondary mirror (M2) is also segmented with seven adaptive thin shells for adaptive optics operation. Each of the seven 1.1 meter M2 segments maps to a single primary mirror segment. This arrangement greatly simplifies the alignment of the telescope optics: the primary mirror segment misalignments will be compensated by the motions of the more agile M2 shells. The GMT is expected to see first light in 2018. It will be erected in the Las Campanas Observatory, in Chile.

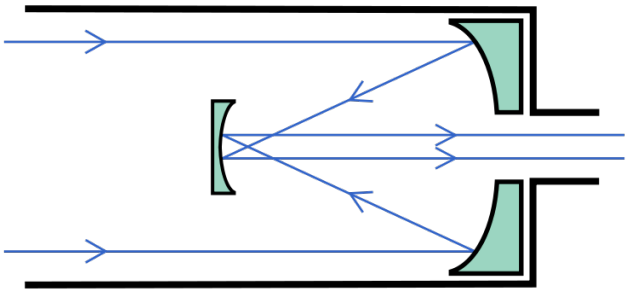

Figura 1.9: The Gregorian telescope [31].

ESO studied the concept of the Overwhelmingly Large Telescope (OWL), with primary and secondary mirrors respectively segmented with 3048 and 216 segments (see [7]). Substantial technical risks were identified, associated especially with the large segmented secondary mirror and the estimated costs too high. It was then decided to proceed with a detailed design phase aiming for a smaller primary diameter, a less complex and less risky telescope. In 2007, a new concept was born, with a primary mirror of 42 meters, the European Extremely Large Telescope (E-ELT). The segmented aspheric primary mirror will measure 42 meter with 984 hexagonal segments of 1.45-m (corner to corner). A new option with a 39 meters primary mirror (the two external rings would be removed) has substituted the old concept, because of technological constraints. The pupil of the telescope is the primary mirror. The convex secondary mirror will measure six meters (and only 4 meters for the 39 meters design) and the tertiary mirror four meters. Adaptive optics is embedded inside the telescope by means of M4 which is a deformable mirror of 2.6 meters (for further information see [24]).

Capitolo 2

Optics fundamentals

In this Chapter we discuss the basic concepts to achieve the two goals of the control (the first one is to compensate the aberrations due to residual errors on lenses surfaces and the turbulence effects on the light, the second one is to co-phase all the segments). Theoretical and mathematical bases are provided, furthermore two basic devices for the control will be analyzed.

2.1 Aberrations

It is the function of a mirror to collect light from a point on the object and to focus that light at a corresponding point on the image. In nearly all cases, the mirror will fail at this task, in that there will be some residual error in the precision with which it collects, reflects and focuses the light [40]. The so-called *lens aberrations* are these errors in the lens ability to form a perfect image, and together with *diffraction* of light through the telescope cause a not precise result (Figure 2.1).

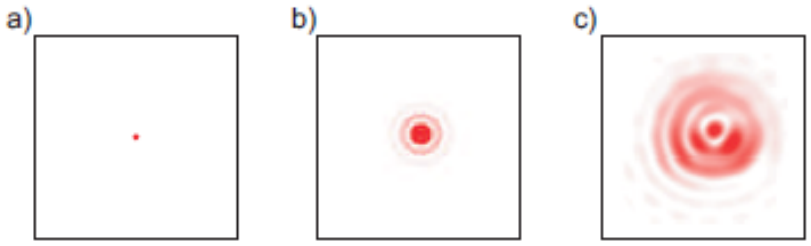

Figura 2.1: (a) Point object; (b) Image spot subject to diffraction; (c) Image spot subject to aberrations and diffraction [1].

Two common ways of visualizing the effect of aberrations on the optical quality are the spot diagram and the radial energy distribution calculation [40]. A *spot diagram* is generated by tracing a relatively large number of rays (usually 200 to 300) from a common object point, through the lens system, and plotting the spot that results due to the intersection of those rays with the image plane. Neglecting the diffraction effects, the spot diagram of an hypothetical perfect lens were a single point. When residual aberrations are present, the spot takes on

a finite size and shape. An analysis of the spot reveals information on the lens quality. If, starting from the center of the spot and gradually increasing its radius, we count the number of rays inside it, we can get a curve showing the percent of energy encircled vs. the spot radius, commonly known as *radial energy distribution*.

Aberrations could be grouped in three basic types: on-axis, off-axis and chromatic. By nature, reflecting telescopes are not affected by chromatic aberrations [40]. Historically, a classification of five primary aberrations has been established, namely spherical aberration, coma, astigmatism (Figure 2.2), field curvature and distortion.

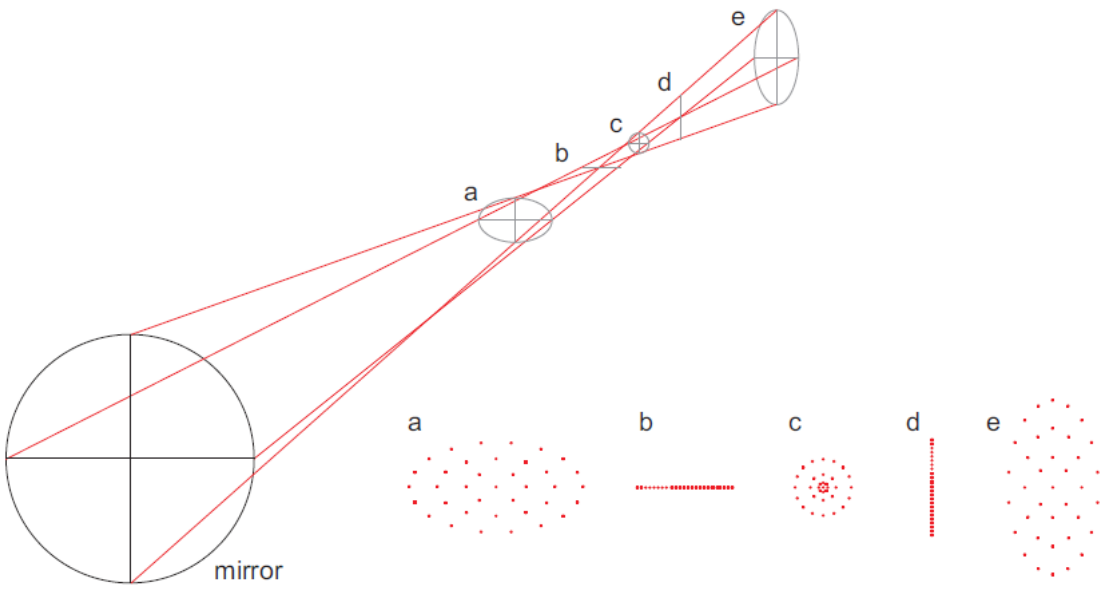

Figura 2.2: Left, ray trace of a wavefront subjected to astigmatism after reflection on a mirror. A mirror subjected to astigmatism sees its radius of curvature varying from a minimum along one of its diameters, to a maximum along the diameter perpendicular to it. Right, spot diagrams corresponding to particular locations along the axis of propagation. Location (c) corresponds to the minimum blur; when the image plane il located elsewhere, the spot has a characteristic elliptic shape that degenerates in straight lines at the focuses corresponding to the minimum and maximum radii of curvature of the mirror [1].

2.1.1 Quantifying the wavefront error

The wavefront error can be expressed as a function of space coordinates $W(r)$. It is calculated with respect to its reference sphere (or plane): this quantity is subtracted to the absolute value of the error in order to get all the values referring to the same plane.
Two main indicators to quantify the quality of the wavefront could be introduced. The first one is the *Peak-to-Valley* (PV) wavefront error: is the difference between the highest and the lowest parts on the surface of the optic, those top and bottom being defined as the local difference between the actual optic and the ideal one. Of course this ignores the curvature of the optics, which is not a defect. In this case it can potentially mislead because it gives no

information about the area over which the error is occurring. A much better measurement is the RMS (Root Mean Square) value of the flatness. This indicator involves measuring a substantial amount of the optic surface at many points and then calculating the standard deviation of the surface from the ideal form [26]. The basic definition is found by defining the $n-th$ power average of the wavefront $W(x,y)$ over the area A of the pupil and then specifically defining W_{rms} or, in words, the RMS wavefront error is the square root of the mean square error minus the square of the mean wavefront error (see Equation 2.1, [33]).

$$\begin{aligned} \bar{W}^n &= \frac{1}{A}\int W(x,y)^n dxdy \\ W_{rms} &= \sqrt{[\bar{W}^2] - [\bar{W}]^2} \end{aligned} \tag{2.1}$$

Conventionally, a system is considered as nearly perfect if the RMS wavefront error of the output beam is less than $\lambda/14$.

It is convenient and easy to express the wavefront error as a linear combination of a set of orthogonal functions defined over the aperture. The Zernike polynomials (see Appendix A) originate one of the most common representation for the wavefront (see [21] and [43]):

$$W(r,\theta) = \sum_{i=1}^{n} a_i Z_i(r,\theta), \tag{2.2}$$

where $W(r,\theta)$ and $Z_i(r,\theta)$ are respectively the wavefront and the i^{th} Zernike polynomial expressed in polar coordinates. The coefficients a_i results from the projection of W on Z_i, and may be computed either by direct integration over the unit circle or by least squares fitting [1].

The first 3 modes (piston, tip and tilt) have no impact on the image quality, because they correspond respectively to a constant and to a linear phase shift all over the wavefront. Defocus is a changing of the overall radius of curvature of the wavefront, the shapes of astigmatism, coma and spherical aberrations as polynomials are close to those of the corresponding primary aberrations.

With the normalized Zernike polynomials (see Appendix A), it's possible to express the RMS error in an easy fashion:

$$W_{rms} = \sqrt{\sum_{i=4}^{n} a_i^2}. \tag{2.3}$$

Equation 2.3 does not include the first 3 Zernike polynomials because they do not affect the image quality.

2.2 Atmospheric effects

Aberrations are not the only causes of the decrease of optical quality. Light propagating through the atmosphere encounters turbulent regions in which the air temperature, density and index of refraction vary. [17] suggested that the kinetic energy in the largest structures

of the turbulence is transferred successively to smaller and smaller structures (Figure 2.3). If the product of the characteristic size L of the small structure and its velocity v is too small to keep the *Reynolds number*[1] in the turbulent regime the break up process stops and the kinetic energy is dissipated as heat by viscous friction.

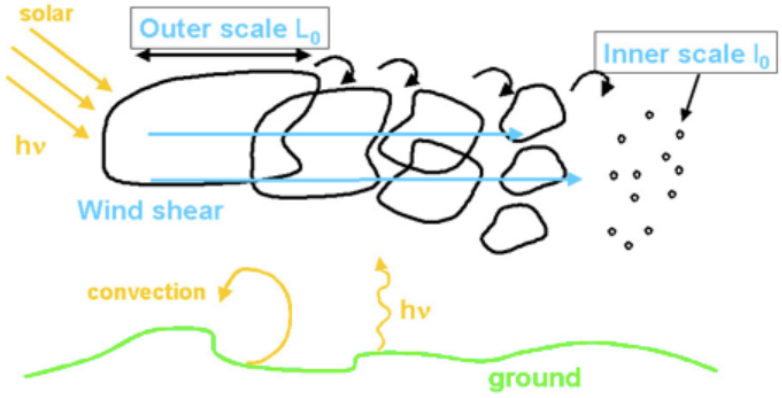

Figura 2.3: The cascade of turbulent energy to smaller and smaller scales according to Kolmogorov theory [14].

The energy flow, in stationary state, from larger structures L to smaller l must be constant. This means that all the energy injected into the largest structures must be equal to the energy dissipated as heat. Supposing $E(l)dl$ the kinetic energy of a structure with a size between l and $l + dl$ and a typical transfer time given by l/v, the energy flow rate, ϵ_0, can be written as [9]:

$$\epsilon_0 = \frac{E(L)dL}{t(L)} = \frac{E(l)dl}{t(l)} = \frac{\frac{1}{2}\rho v^2}{l/v} = const. \tag{2.4}$$

So $v(l)$, turbulent velocity on a scale l, could be expressed as:

$$v \propto (\epsilon l)^{1/3} \tag{2.5}$$

Considering isotropic the turbulence, in the Fourier domain the turbulent energy at wave number $k \sim 2\pi/l$ depends only on the magnitude κ in the range $d\kappa$. From dimensional analysis the energy per unit mass is

$$E(\kappa)d\kappa \propto v^2 \propto k^{2/3} \tag{2.6}$$

Thus,

$$E(\kappa) \propto \kappa^{-5/3} \tag{2.7}$$

which is known as *Kolmogorov's law*. For the isotropic turbulence the three dimensional case can be calculated by integrating over the unit sphere:

[1]It is defined as $Re = \frac{L_0 v_0}{k_v}$, where L_0 is the characteristic size of the flow, v_0 is the characteristic velocity and k_v is the kinematic viscosity

$$E(\kappa) = 4\pi\kappa^2 E(\overrightarrow{\kappa}) \Rightarrow E(\overrightarrow{\kappa}) \propto \kappa^{-11/3} \tag{2.8}$$

This relationship expresses the Kolmogorov spectrum. It holds in the inertial range of turbulence for $L_0^{-1} \ll \kappa \ll l_0^{-1}$ where L_0 is the outer scale of turbulence, generally the size of the largest structure that moves with homogeneous speed, and l_0 is the inner scale at which the viscous dissipation starts. The outer scale of turbulence varies between a few meters close to the ground where the largest structure is determined by the height over the ground, and a few hundred meters in the free atmosphere which is the thickness of the turbulent layer. The inner scale of turbulence is in the range of a few millimeters near the ground to about 1cm near the tropopause [9], a layer of the atmosphere, set at 15km from the ground, which separates the troposphere from the stratosphere.

Again the Zernike polynomials (see Appendix A) are useful. The polynomial expansion of an arbitrary wavefront $\phi(\rho, \theta)$ over the unit circle is defined as

$$\phi(\rho, \theta) = \sum_{i=1}^{\inf} a_i Z_i(\rho, \theta) \tag{2.9}$$

and the coefficients, using the orthogonality, are given by

$$a_i = \int_{aperture} \phi(\rho, \theta) Z_i(\rho, \theta) \rho d\rho d\theta \tag{2.10}$$

Following the Kolmogorov statistics, it's possible to determine individually the power associated to every single mode[2]. One can immediately estimate the residual aberration after correcting a specified number of modes with an adaptive optical system. The variance of the residual aberration is expressed as the variance of the difference between the uncorrected phase and of the removed modes. It can be expressed as:

$$\Delta_J = \int\int_{aperture} < [\phi(\rho, \theta) - \phi_J(\rho, \theta)]^2 > \rho d\rho d\theta \tag{2.11}$$

where $\phi_J(\rho, \theta)$ is the aberration due to the first J Zernike polynomials. It's possible to note that this variance is infinite if the piston term is not neglected.

$\Delta_1 = 1.030(D/r_0)^{5/3}$	
$\Delta_2 = 0.582(D/r_0)^{5/3}$	$\Delta_2 - \Delta_1 = 0.448$
$\Delta_3 = 0.134(D/r_0)^{5/3}$	$\Delta_3 - \Delta_2 = 0.448$
$\Delta_4 = 0.111(D/r_0)^{5/3}$	$\Delta_4 - \Delta_3 = 0.023$
$\Delta_3 = 0.0880(D/r_0)^{5/3}$	$\Delta_5 - \Delta_4 = 0.023$
$\Delta_3 = 0.0648(D/r_0)^{5/3}$	$\Delta_6 - \Delta_5 = 0.023$
$\Delta_3 = 0.0587(D/r_0)^{5/3}$	$\Delta_7 - \Delta_6 = 0.0062$
$\Delta_3 = 0.0525(D/r_0)^{5/3}$	$\Delta_8 - \Delta_7 = 0.0062$

Tabella 2.1: The residual variance Δ_j of Kolmogorov turbulence after the first j Zernike modes are removed [9].

[2]For further information [9], [14] and [30]

The residual variances (see Table 2.1) are given in terms of[3] $(D/r_0)^{5/3}$ and the Zernike polynomials are defined in the telescope aperture D.

2.3 Sensors

The control applied to the system works on two different aspect: the shape control of the mirror to compensate aberrations and turbulence effects, and the co-phasing of the mirrors (Figure 2.4). To conform these requirements different sensors are needed to create a feedback control system. Basically a sensing method for the surface shape and another for the relative distance between segments are required.

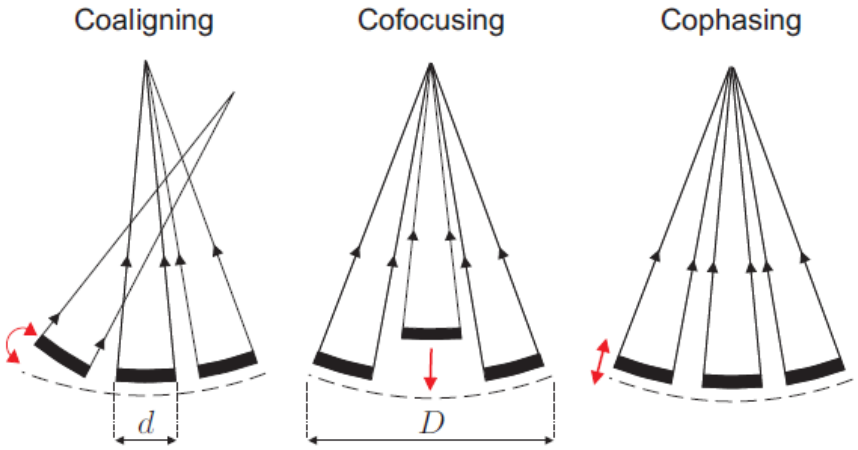

Figura 2.4: Three main requirements of the control system between the mirror. Adapted by [3].

2.3.1 The Shack-Hartmann sensor

Atmospheric turbulence and the optical train of the telescope disturb the collected beam of light by delaying the wavefront in a non-uniform manner over its aperture. A correction of the beam must be performed by the deformation of the mirror, and Shack-Hartmann sensors are commonly used to provide measurements of the wavefront with minimal measurements processing and in a photon-efficient way (moreover it's achromatic, that is independent of wavelength [9]). They provide the measurements of the gradient of a wavefront in an array of discrete points ([12] provides a detailed discussion about this sensor and its practical implementations).

The major components of these sensors are an array of lenslets and a parallel camera located at their focal distance (Figure 2.5).

[3]The r_0 parameter is called Fried parameter of Fried's coherence length and measures the quality of the optical transmission through the atmosphere due to random inhomogeneities in its refractive index. It is defined as the diameter of the circular area over which the rms wavefront aberration due to the passage through the atmosphere is equal to 1 radian. The Fried parameter has units of length and is typically expressed in centimeters. To get more details [30] and [14].

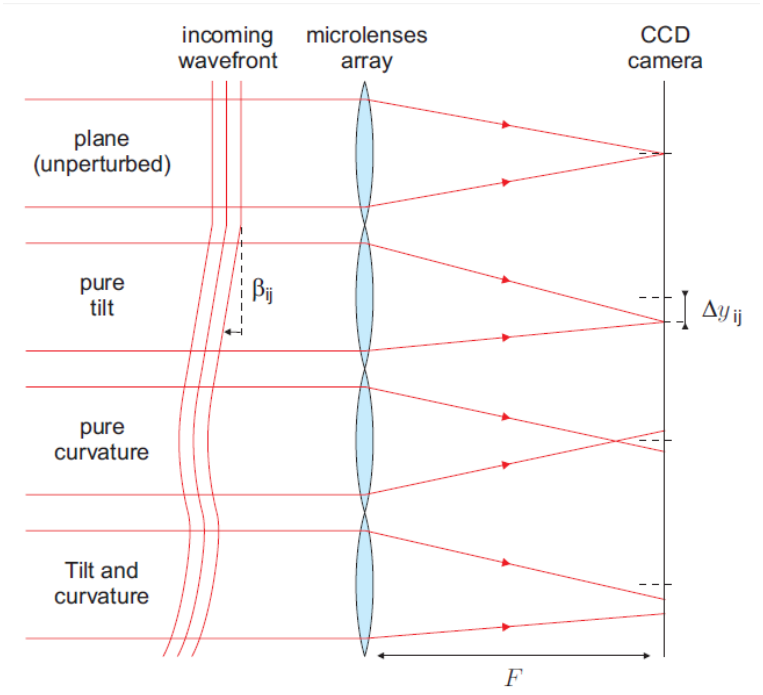

Figura 2.5: Convergence of beams within the sub-apertures of the Shack-Hartmann sensor for different shapes of the wavefront [1].

The converging point of the incoming light depends on the shape of the wavefront within the respective sub-aperture and the image formed on the focal plane is recovered by a camera consisting of a Charge Couple Device (CCD), that is an array of semiconductive elements that produces an electrical change proportional to the intensity of incident light. Different situations occur [1]:

- a collimated wavefront, propagating parallel to the optical axis of the microlens, is focused on its focal point.
- the focus of a collimated wavefront that is slightly tilted with respect to the optical axis of the microlens is shifted laterally on the focal plane. This shift is linearly proportional to the tilt angle.
- local curvature of the wavefront results in a longitudinal shift of the focus with respect to the focal plane (upward or downward, depending on the sign of the curvature). It results in a spreading of the image at the level of the CCD detector. The centroid of that spot is used to measure the local slope similarly as above.

The centroid, or first-order moment M, of the image intensity $I(u, v)$ with respect to x-direction in the image, is related to the partial derivative of the wavefront in the sub-aperture:

$$\begin{aligned} M_x &= \frac{\int\int_{image} I(u,v)ududv}{\int\int_{image} I(u,v)dudv} \\ &= \frac{\lambda f}{2\pi}\int\int_{subaperture}\frac{\partial\phi}{\partial x}dxdy = \frac{\lambda f}{2\pi}\int_0^{d/2}\int_0^{2\pi}\frac{\partial\phi}{\partial x}\rho d\rho d\theta \end{aligned} \tag{2.12}$$

with f the lenslet focal length. A centroid algorithm analyzes the image frames captured by

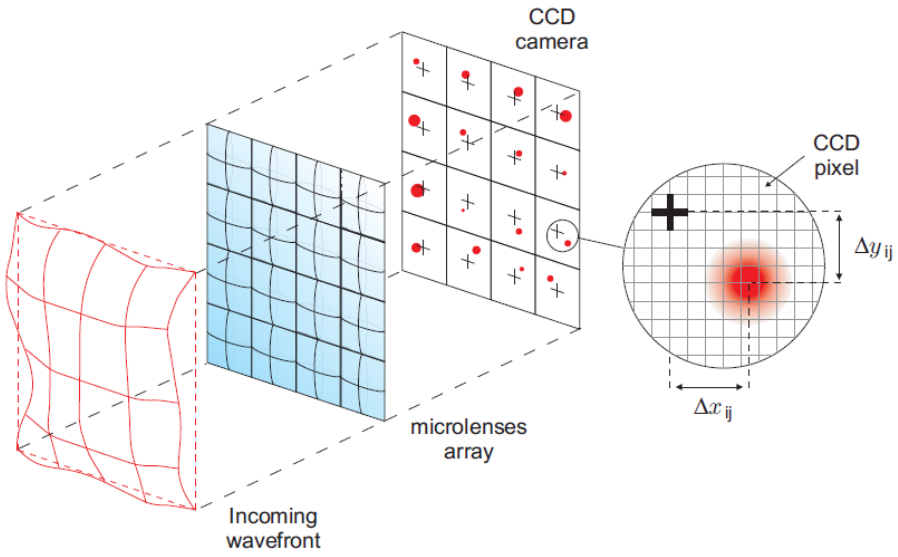

Figura 2.6: The image of the Shack-Hartmann appears as an array of spots of various sizes shifted laterally from the nominal foci of the microlenses. A centroid algorithm determines those lateral deviations from the signals of the CCD camera [1].

the CCD to determine the lateral deviations of each spot with respect to the nominal foci of an unperturbed wavefront. This allows the determination of the local slopes of the wavefront over each microlens, projected along two directions (Figure 2.6):

$$\begin{aligned} \alpha_{ij} &= \frac{\Delta x_{ij}}{f} \\ \beta_{ij} &= \frac{\Delta y_{ij}}{f} \end{aligned} \tag{2.13}$$

where Δx_{ij} and Δy_{ij} are the lateral deviations of the centroid with respect to the nominal foci. Various post-processing algorithms then allow the reconstruction of the shape of the wavefront from the array of local slopes.

It must be emphasized that SH sensors are totally insensitive to the piston term. As a consequence if a (single) Shack-Hartmann sensor is used to measure a set of mirrors together, the result will not be correct from the point of view of segments co-phasing (see Figure 2.7).

2.3.2 Edge sensors

For this and the following sensor the focus of the control shifts now to the co-phasing of the segments.

An intuitive way to do this is the use of edge sensors: these are devices able to measure the *relative* distance between adjacent surfaces. We can mention the capacitive technology for the edge sensors, which is one of the most common ones (other technologies are related for

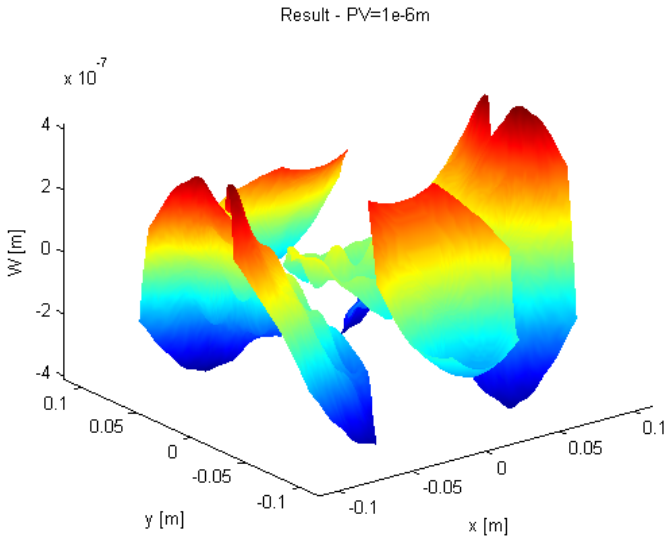

Figura 2.7: The Shack-Hartmann sensor used to measure an astigmatism over 7 segments. The piston term is not measured by the sensor, so the segments are not co-phased. The little bumps in the central segment are due to a sensing error that will be discussed in Chapter 5.

example to semiconductors). It is based on a capacitor (or condenser), in which the two plates are one linked to a segment and the other linked to an adjacent segment. The changing of the relative distance between the two plates causes a potential difference as output, which could be correlated to the relative displacement using suitable conversions. A real implementation could be found in [15].

It is important to stress that these devices cannot be installed on the system studied in this thesis, and described in Chapter 3. This is basically due to two factors: the weight and the dimensions of the device. The weight originates local undesired deformations and stresses, in consequence of them the measurements could be strongly affected and potentially the system itself could be locally damaged. The big dimensions of the device complicate the assembly of the mirrors and create troubles in case of interventions on the system because of faults or maintenance.

A control algorithm based on edge sensors measurements is proposed in Chapter 4.2. The goal is to demonstrate which results this technique could bring, that is how the control works when the relative distance between segments in certain points of the mirror's edge is known. Specifically 2 edge sensors per edge are supposed (for details see Chapter 4). The measure in these specific points could be provided by suitable optical sensors or also from a specific edge sensors not already available.

Finally, it is useful to underline that the use of edge sensors could be susceptible to possible mounting errors if the effective measure point is not located in the gap between segments, that is the device is not exactly on the edge of a segment.

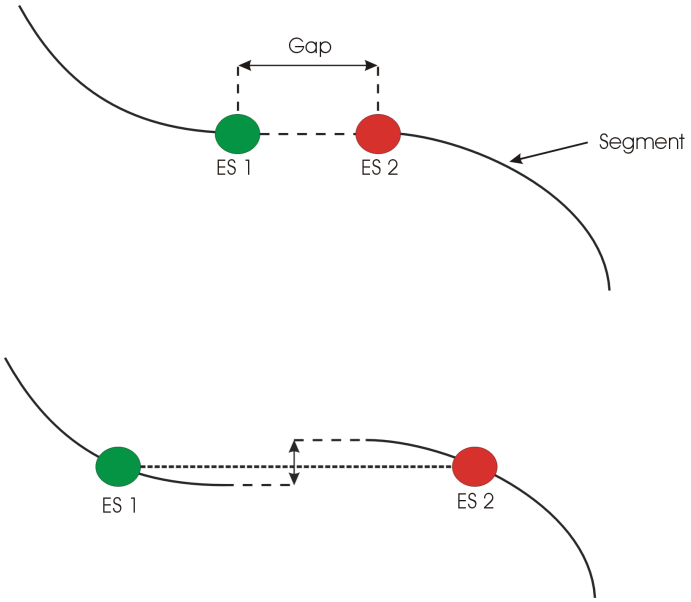

Figura 2.8: In the figure the effect of a little distance of the sensor from the edge: the control loop cannot reach a good co-phasing, because the measure is not the real one, but it's shifted inside.

2.3.3 Zernike Phase Contrast Sensor

A complete description of the sensor is provided in [37], and most of this section is based on it.

The Zernike Phase Contrast Sensor finds its origins in interferometric techniques (in particular the Mach-Zehnder interferometer) and thanks to a simple *phase mask* (Figure 2.9) it is used to evaluate the piston differences between two adjacent segments.

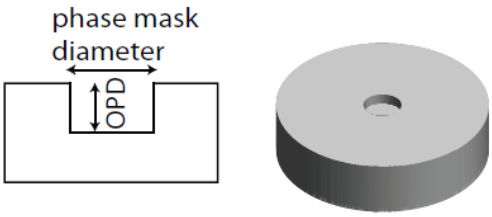

Figura 2.9: The phase mask consists of a cylindrical pellet, etched within a substrate, with a depth corresponding to the OPD and with a diameter noted as phase mask diameter in the figure [37].

Mathematically, let $\mathbf{r}$ be the position vector in the pupil plane (with rectangular coordinates (x, y)) and let ρ the position vector in the focal plane (in polar coordinates (x, y)). Comparing with Figure 2.10 $U_1(\rho)$ is defined as the complex amplitude in the plane of the entrance pupil, in front of the phase mask, and $U_2(\mathbf{r})$ as the complex amplitude in a pupil plane after the phase mask.

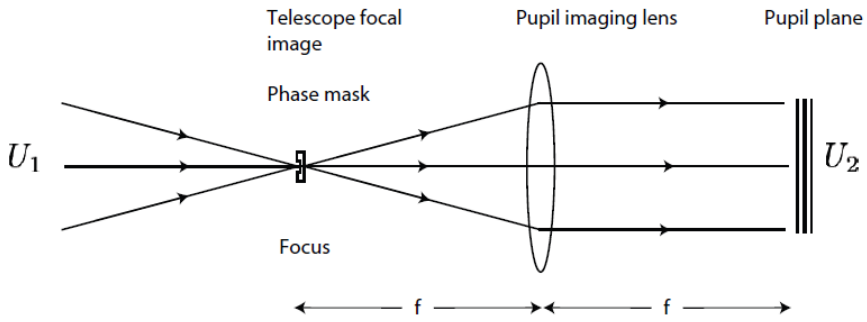

Figura 2.10: Zernike phase contrast sensor layout: After the filtering of the incoming wavefront U1 by the phase mask in the focal plane, the pupil is re-imaged on the detector plane, U2, by a pupil re-imaging lens of focal length f [37].

The phase mask is described by the following expression:

$$b(\rho) = 1 + [exp(i\psi_0) - 1]\Pi(\rho), \tag{2.14}$$

where $\Pi(\rho)$ is:

$$\begin{cases} 1 & if\ |\rho| \leq a/2 \\ 0 & if\ |\rho| > a/2 \end{cases}$$

and ψ_0 is the phase shift induced by a mask with diameter a. This mask is commonly defined as sharp edge pinhole. It is possible to define a phase mask with apodized edges with a Gaussian function:

$$\Pi(\rho) = exp[-(\frac{\rho}{(2\sqrt{ln2})^{-1}a})^2] \tag{2.15}$$

The complex amplitude in the plane of the exit pupil can be expressed as the convolution of the complex amplitude in the plane of the entrance pupil and the Fourier transform T(ρ) of the transmission function of the phase mask $\Pi(\rho)$:

$$U_2(\mathbf{r}) = U_1(\mathbf{r}) + (exp(i\psi_0) - 1)\frac{1}{\lambda^2}\int U_1(\mathbf{r'})T(\mathbf{r} - \mathbf{r'})d\mathbf{r'} \tag{2.16}$$

For the expressions of T(ρ) in both mask cases see [37].
The intensity in the plane of the exit pupil, that is the signal of the Zernike Phase Contrast Sensor, is given by

$$S(\mathbf{r}) = |U_2(\mathbf{r})|^2. \tag{2.17}$$

With a local coordinate system centered on the edge between two segments (the x-axis being perpendicular to the edge as shown in Figure 2.11), and with φ_1 and φ_2 being the piston phase values of two segments, the complex amplitude $U_1\mathbf{r} = U_1(x)$ in the plane of the entrance pupil depends only on the x-coordinate and can be expressed as

$$\begin{cases} exp(i\varphi_1) = exp(ikp_1)\ if x < 0 \\ exp(i\varphi_2) = exp(ikp_2)\ if x > 0 \end{cases}$$

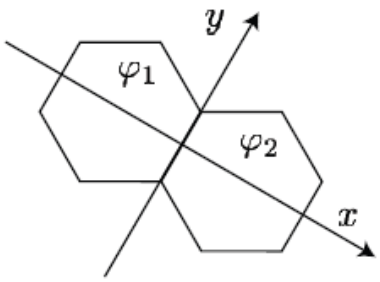

Figura 2.11: Cartesian coordinate system at the boundary between two segments and the phases ϕ_1 and ϕ_2 due to piston in each segment [37].

where p_1 and p_2 are the piston values of the two segments, λ is the wavelength of the light and $k = 2\pi/\lambda$ is the wavenumber.
$\Delta\phi$ is defined as the phase jump generated by the phase difference $\phi_2 - \phi_1$ and Δp as the piston step generated by the piston difference $p_2 - p_1$, therefore $\Delta\phi = k\Delta p$. Δp is the piston step measured on the wavefront, which is twice the value of the piston step measured on the surface of the mirror.

Further details about the sensor and the mathematical concepts which are behind it are provided in [37] .

To simulate this sensor inside our system, we suppose that we know the (absolute) displacement of a certain number of points on the edge of each segment (normally 8, results are not affected if this number is doubled). Then the mean value of these points is calculated and it's used in the control loop. The possibility of spreading the points on the edge in two sub-groups and so to get two mean values per edge was investigated, but the results are not improved in a relevant way.

Capitolo 3

The model

3.1 Concept and design

For the segmentation of telescope mirrors, several solutions are feasible. In particular two of them are commonly envisioned to achieve a dense tessellation: the honeycomb-type and the keystone-type (Figure 3.1).

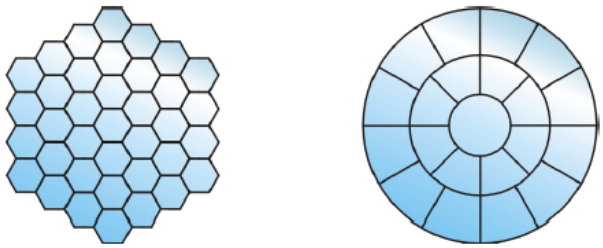

Figura 3.1: Tessellation geometries: honeycomb on the left, keystone on the right [1]

Between the two the most interesting for large telescopes is the hexagonal one. Hexagonal segments are in fact more simple to fabricate and to polish, and moreover the position of sensors and supports is the same for all the segments, an important advantage to make the control easier.

An hexagonal segmented geometry is used for the system here studied. In the following sections the components of the segmented mirror will be discussed (in Figure 3.2 the cross section of the mirror). Moreover the *ad hoc* technological processes developed to abide by tolerances, quality and system resistance are here illustrated.

3.1.1 Mirror and coating

The starting mirror is a circular Silicon wafer (Figure 3.1). In the image the mirror is not a complete circle, but there is a rectilinear side. That's a widespread convention of mirror suppliers: it helps to handle and to place the mirror, and moreover specifies the principal

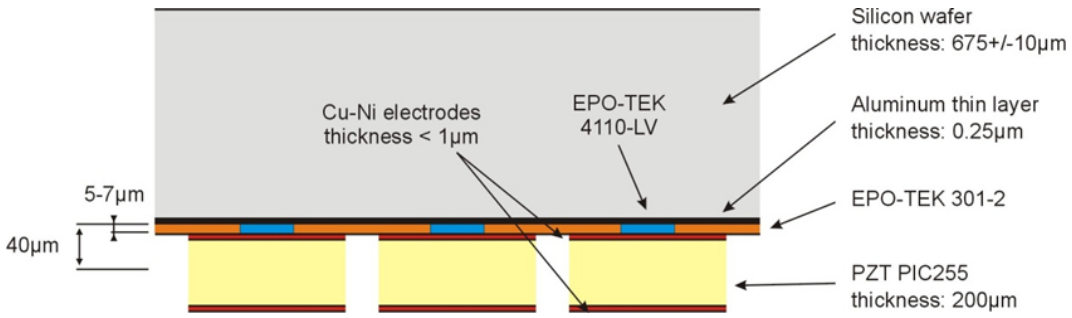

Figura 3.2: The mirror cross section. From the top to the bottom: Silicon wafer, Aluminium layer, glue and piezoelectric actuators.

direction of material's fibers (it's an orthotropic material).

At a later stage, an aluminium coating is applied to the mirror: the layer's thickness is $150nm$ (Figure 3.3). The Aluminium coating provides a good conductivity. Moreover it was verified that the coating did not affect too much the surface quality (from the point of view of RMS and PV, basically if it induced some deformation). As further control the resistance to peeling forces induced by the adhesive tapes used in the manufacturing process was tested. In fact this resistance has to guarantee the resistance to piezoelectric actuators forces.

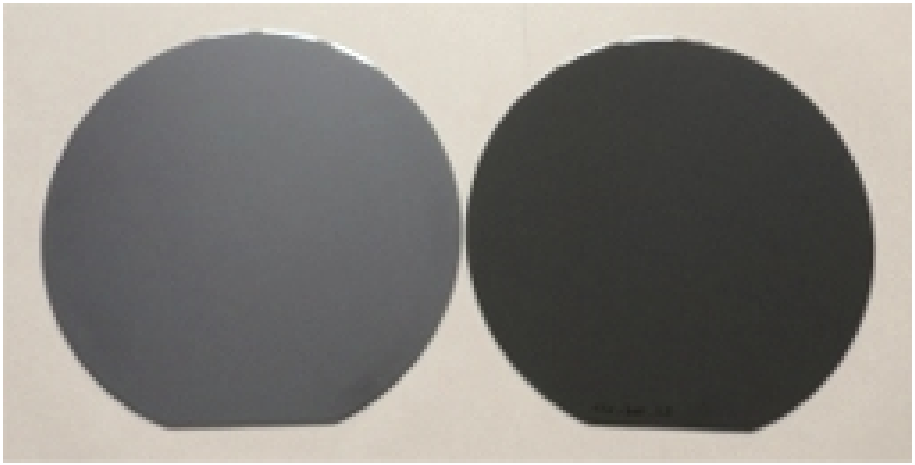

Figura 3.3: The mirror with the Aluminium coating, left; the mirror without coating, right.

3.1.2 Piezoelectric actuators and ground electrodes

If a piezoelectric material is subjected to a stress state, an electric charge is generated on the material surface. Also the vice versa is true, that is when an electric field is applied, this material changes shape and dimensions.

Due to their internal stiffness, *if their natural expansion is limited*, piezoelectric elements are able to create substantial forces: so they could be used as *actuators*. In a dual way the could act as *sensors*: if they are connected to a deforming material, they generate a measurable

electric tension.

Their internal atomic structure is anisotropic, and they can be polarized following well-defined orientations. In particular the so called *inverse piezoelectric effect* (discovered by Pierre and Marie Curie in 1880) asserts that the application of an electric field, parallel to the polarization direction, produces an expansion of the material. The first sensors/actuators made by piezoelectric materials were introduced between the 40's and the 50's. Examples of piezoelectric materials nowadays used are polymeric (PVDF, polyvinylidene difluoride) or ceramics PZT (lead zirconium titanate).

For a mathematical treatise of piezoelectric system properties refer to Appendix C.

PZT actuators are chosen for this system: hexagonal patches (Figure 3.4) are glued to the back of the mirror. A layer of 37 PZT hexagonal patches is created (Figure 3.5) and a cutting

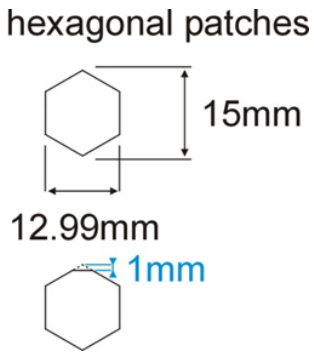

Figura 3.4: Shape and dimensions of an hexagonal PZT patch.

must be performed to get the hexagonal mirror. The goal of this network of patches is to create local deformations of the mirror's surface. On each patch is welded a cable which connects the patch to the electrical network. In Figure 3.5 the three little grey circles represent the position of the ground electrodes[1]: their function is to provide a potential difference. It's theoretically possible to use only one ground electrode, but a configuration with 3 of them is preferred to be sure that the whole mirror has a ground connection and to protect the system from possible connection's faults.

3.1.3 Feet

Each segment is equipped with 3 feet which connect it to the base structure. The function of the feet is not only support, but also to transmit rigid motion to the mirror, i.e. the first three Zernike polynomials: piston, tip and tilt (see Appendix A). Three are the main parts of each foot (Figure 3.6): a *position actuator* at the bottom (the piezoelectric beam is mounted transversally respect to the principal axis, and an elliptical structure acts as mechanical amplifier), the central part (composed by several magnetic materials) and a sphere at the top, which interact with an interface part linked to the mirror. The interface part of the feet

[1] A corner of the piezoelectric patches near the ground electrodes is trimmed, but it's experimentally verified that it has negligible effects on performances. Moreover soldering to Aluminium is difficult, so 2.5mm wide, 220μm-thick copper disks are glued at the right position with an electrically conductive glue.

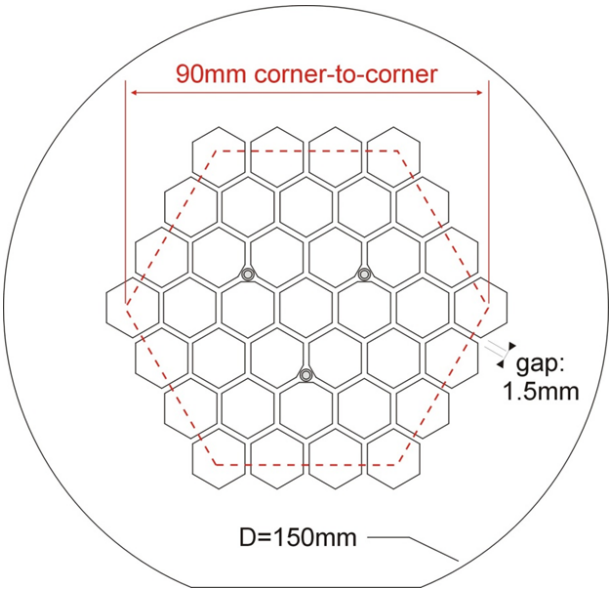

Figura 3.5: The starting circular mirror with the layer of patches. The red dotted line states the dimensions and the geometry for mirror's cutting.

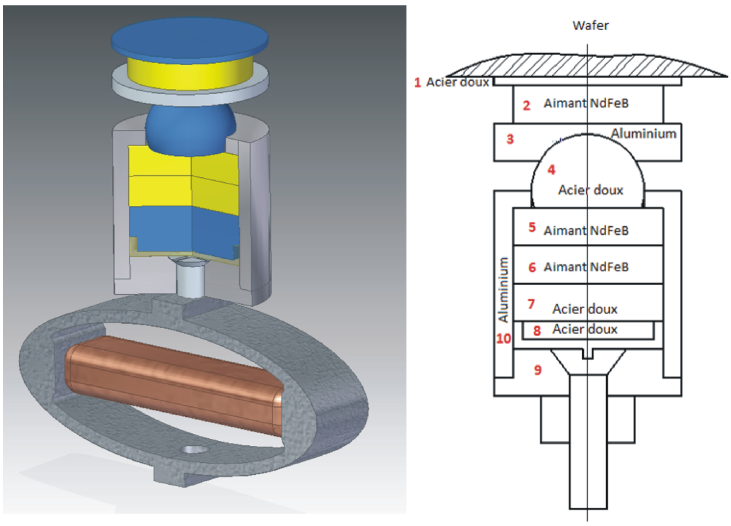

Figura 3.6: CAD model of an active foot and detail of its components.

can be seen as infinitely stiff with respect to the segment, i.e. there must be a mechanical decoupling between the segment and the interface part to avoid a loss of control authority. Adhesives/glues may provide the required compliance, but need a good contact area: a contact area overlapping the gap between 2/3 patches is a more difficult option that a contact area over a single patch. Some adhesive tapes provide the desirable features: very high bonding strength, high compliance, low outgassing, negligible mass, ease of implementation, compatibility with the steps of the manufacturing. Moreover its high compliance allows gluing the foot over a patch without deteriorating its morphing authority. So as interface part is chosen a 8mm diameter, 0.5mm thick steel circle, with a 0.006mm adhesive tape on one side, and it's glued at the center of a piezoelectric patch thanks to the adhesive layer as shown in Figure 3.7. Moreover it is experimentally verified that the influence of the steel layer is negligible for

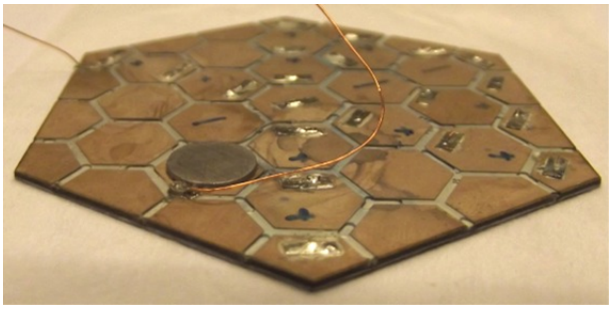

Figura 3.7: The hexagonal mirror with the network of actuators and an interface layer glued at the center of a patch.

the optical quality and the adhesive layer does not suffer for creep effect.

To choose the position of the three feet, 2 criteria are been followed: to minimize the detrimental effect to the resonance frequency and preferably a contact area which not overlaps a gap between the patches. Parametric studies are been made on a numerical model and the optimum in terms of frequency is in the vicinity of $r/R = 0.4$. Patches can be found in the interval $r/R = [0.5, 0.6]$ without a significant decrease of the first natural frequency, which in this case is $f_1 > 500Hz$.

From a design point of view, an isostatic configuration for the feet is implemented (flat-cone-groove interfaces block the 6 rigid-body d.o.f.). This allows a decoupling between the deformation and position actuation of the wafer. Moreover there is an improved authority of the patches and the thermal distortions of the segment are again decoupled from those of support and feet. Feet are then assembled on a support plate with a glue joint; the deformation and position actuation of the wafer. The latter allows a proper assembly strategy, based on stops to fix the relative position of the segments, that shall allow assembling their respective feet and the global support plate to conform to the position of the segments. At the end the electrical wires will pass through the central hole in the support plate and a rigid PCB board will be attached to the back of the support plate to welcome the electrical wires; a flex circuit will connect this PCB board to the control electronics. This approach minimizes the mechanical interferences of the wiring with the segment and simplifies the design.

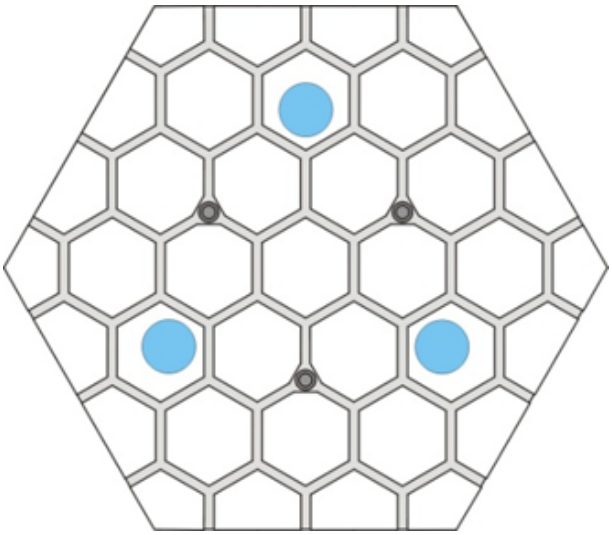

Figura 3.8: The blue circles indicate the positions of the feet. The foot should be slightly decentered on the patch to leave enough space for the electrical connector of the patch.

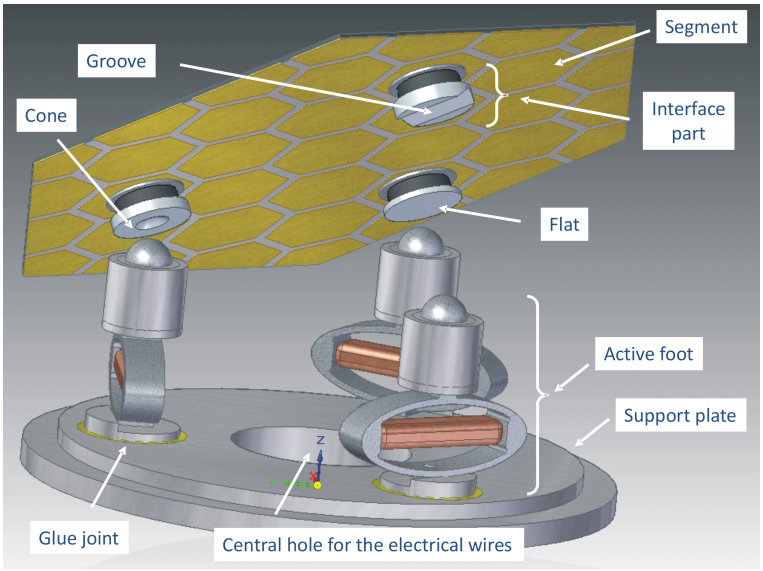

Figura 3.9: The FEM representation of the .

3.1.4 Technological aspects

The creation of this system needs a lot of technological background and experimental tests. Two aspects are in particular critical: the gluing of the piezoelectric patches and the mirror cutting.

- **Gluing:** a first strategy was to spread all along the surface. A spatula was used to spread it and thin wires were used as guides for the thickness. However, this process was uneasy and limited by the availability of thin yet strong wires. This approach has been replaced by the use of a calibrated pipette of common use in bio-chemistry laboratories, made possible by the very low viscosity of the glue. This provides a fast, easy and accurate way to control the quantity of glue that is applied. A further improvement of the process is to glue the patches on a spherical and stiff support: it's experimentally verified that the final quality of the mirror is improved. See Figure 3.10.

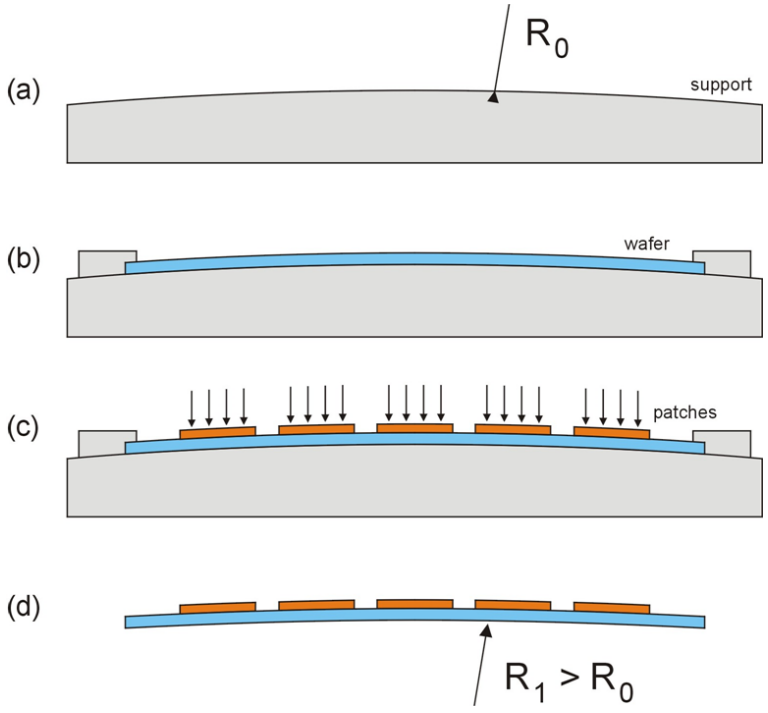

Figura 3.10: (a) The gluing support is machined as a portion of a convex sphere with a radius of curvature R_0. (b) The wafer is forced to conform on the support. (c) The patches are glued on the wafer. A weight is applied to bend the patches over the wafer. (d) When released, after the curing, the wafer is bent as a concave spherical shape with a radius of curvature $R_1 > R_0$ (the wafer is less curved than the support).

- **Cutting:** also in this case several attempts were made before to find acceptable results. The cutting is made by laser, which slices only the PZT and part of the mirror, and the final breaking is made by hand.

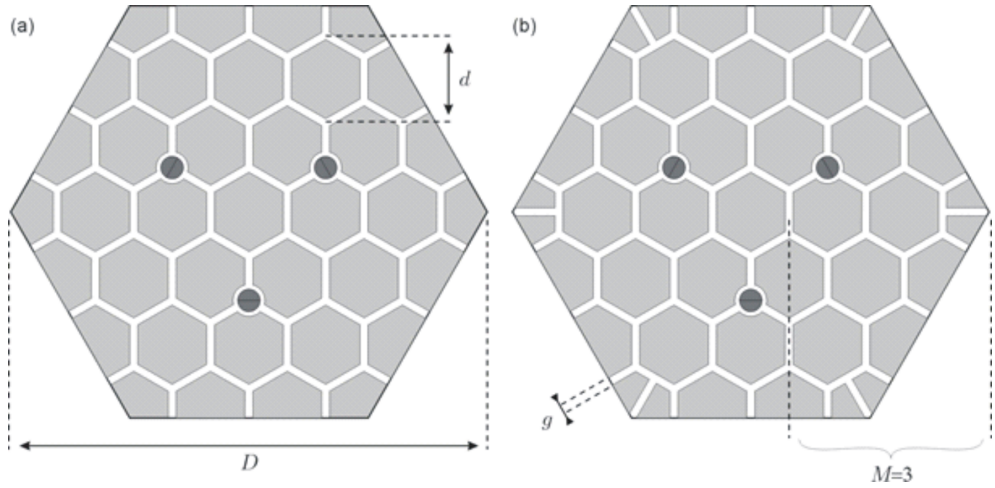

Figura 3.11: Main parameters of the baseline geometry of the segments. The actuators are distributed over a dense honeycomb pattern. The intersections with the edges of the segment and with the areas where the isostatic support is located are taken into account. Configuration (b), with split-corners, will not be used.

3.2 Finite Element model

The baseline of the geometry of the parametric model and some of its features are illustrated in Figure 3.11.
The mirror and the patches of piezoelectric material are of hexagonal shape. The network of patches extends up to the edges of the segment to allow covering the largest area possible; the intersections of the patches with the edges are detected automatically and the corresponding shapes are adapted in consequence. The patches in the corners may be kept full or can be divided in two parts to refine the control over the edges, which may be important regarding the ability of the segmented mirror to generate a continuous surface. This second configuration (the so called *split-corners configuration*) will not be used here. Indeed with respect to the advantage mentioned above, several disadvantages are present, three in particular: more difficulties for the gluing of the patches, an increasing complexity of the electrical wirings and for the design of the electronics, and finally it induces a less precision sensing with the Shack-Hartmann sensor.

The main parameters are:

- D: the (outer) diameter of the segment;
- M: the number of rings of actuators surrounding the central one;
- d: the (outer) diameter of an actuator;
- g: the gap between two adjacent actuators.

The position of the feet is a second control parameter; this is an important parameter regarding its impact on the figure error, the resonance frequencies, the static and dynamic responses, etc. In fact it sets the boundary conditions. Another set of parameters allows controlling the

density of the finite element (FE) mesh.

Standard triangular and quadrangular planar elements are used to mesh the structure in the FE software SAMCEF. An example is illustrated in Figure 3.12; one may recognize regular patterns corresponding to the actuators. The mechanical behavior of the segment is modelled

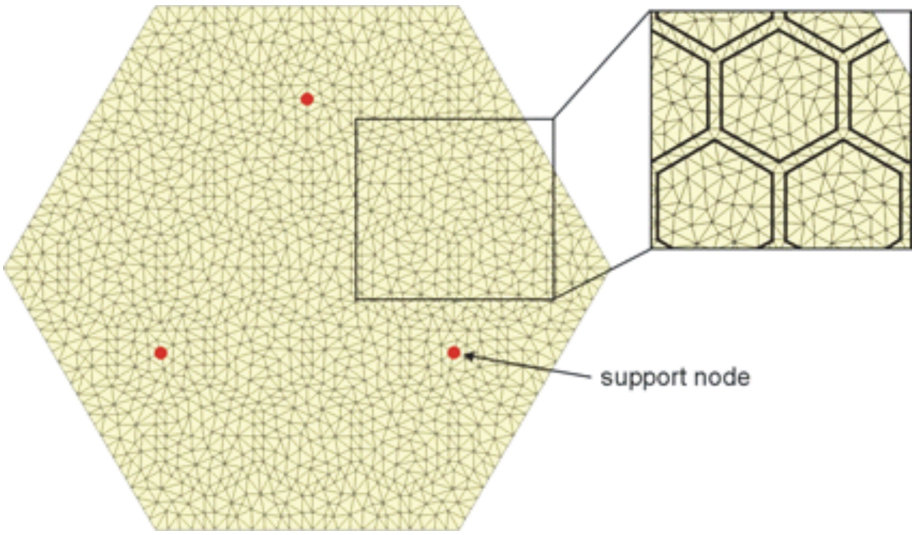

Figura 3.12: Mesh of the finite element model built in SAMCEF. The red dots show the location of the support nodes. One may recognize regular patterns corresponding to the patches. Various parameters allow choosing the density of the mesh.

using multilayered plate elements, based on a Mindlin formulation. The thickness and material properties of each layer can be defined independently; arbitrary sequences of layers can be combined to model any part of the structure. The actuators are modelled by a layer with the properties of a piezoelectric material. This module has been developed at the Active Structures Laboratory [27] and subsequently implemented as a standard tool in SAMCEF. The model allows implementing easily combinations of an arbitrary set of layers to represent any design option that may be worth to study.

The model used throughout this thesis includes the Aluminum ground electrode and the electrodes of the patches; it neglects the influence of the electrical wires and of their soldering spots. The layer of glue is also neglected: this corresponds to the ideal case where the glue is infinitely stiff and the layer infinitely thin. The boundary conditions are also simplified with respect to the reality, therefore the numerical results may be seen as the best results achievable. The material characteristics are summarized in Table 3.1; we use homogenized values for the silicon based on the literature, those for the PZT patches come from the datasheet of the patches purchased to build the demonstrators, and have been later refined after a discussion with the provider. The properties of Aluminum are based on standard average values. The whole model is based solely on linear hypotheses and the regime for the computations is also assumed linear (small displacements). Active Structures Laboratory has gained a broad experience in the modelling of smart structures implementing piezoelectric materials, which also helped in validating the dedicated SAMCEF module by confronting it to various experimental results. In particular, the correspondence between the experimental and numerical results of

Silicon	
$\rho[kg/m^3]$	2329
$E[GPa]$	130
$\nu[/]$	0.275
$\alpha[1/K]$	$2.59e^{-6}$

PZT PIC 255	
$\rho[kg/m^3]$	7800
$c_{33}^E[GPa]$	52.9
$c_{11}^E[GPa]$	52.9
$\nu[/]$	0.34
$\alpha[1/K]$	$6e^{-6}$
$\epsilon[nF/m]$	15.5
$d_{31}[pm/V]$	-180

Aluminium	
$\rho[kg/m^3]$	2700
$E[GPa]$	69
$\nu[/]$	0.33
$\alpha[1/K]$	$23.0e^{-6}$

Tabella 3.1: Main characteristics of materials.

this type of deformable mirrors has proved very good [30].

3.3 Stoney formula

In this section the FEM model will be validated using a famous result about film stress and substrate curvature, known as *Stoney formula*.

3.3.1 Mathematical formulation

The existence of residual stress in films deposited on substrates and the effect of such stress on delamination and cracking were recognized as early as the nineteenth century. In 1909 Stoney made the observation that a metal film deposited on a thick substrate was in a state of tension or compression when no external loads were applied to the system and that it would consequently strain the substrate so as to bend it [8].
Let us suppose that a thin film is bonded to one surface of a substrate of uniform thickness h_s. It will be assumed that the substrate has the shape of a circular disk of radius R, although the principal results of this section are independent of the actual shape of the outer boundary of the substrate [8]. The film is supposed very thin in comparison with the substrate and the substrate is thin so that $h_s \ll R$. The film has an incompatible elastic mismatch strain with respect to the substrate, and the mismatch strain is assumed to be an isotropic extension or compression in the plane of the interface. Using the subscript 's' to denote the properties of the substrate, it is assumed to be an isotropic elastic solid with elastic modulus E_s and Poisson ratio ν_s.
Because the state of deformation is equi-biaxial strain at each point of the substrate, the resistance to the deformation can be represented in terms of the biaxial elastic modulus of the substrate material, which is denoted by M_s. In an isotropic material, the biaxial elastic modulus is the ratio of equi-biaxial stress to equi-biaxial strain, and for the substrate material could be expressed as $M_s = E_s/(1-\nu_s)$.
Stoney formula can be derived using a number of different methods (and following suitable hypotheses), see [8] or [35] for details.

Considering now the membrane force f (Figure 3.13) of the thin film, the *Stoney formula* is:

$$\kappa_{St} = \frac{1}{R_c} = \frac{6f}{M_s h_s^2} \tag{3.1}$$

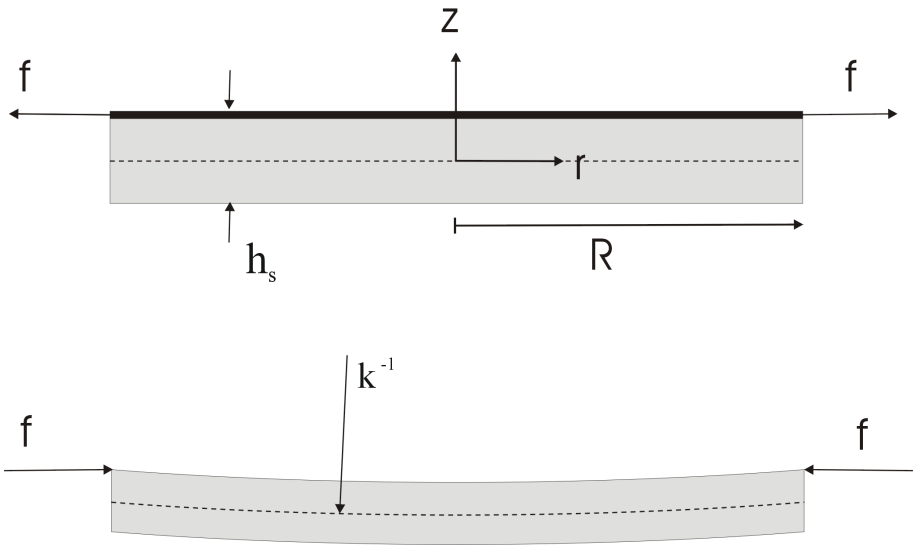

Figura 3.13: Development of curvature in a film-substrate system with mismatch is represented as the sum of the two deformation states depicted here.

where R_c is the radius of curvature and κ its inverse. The sign of the curvature is as that of f. For the case of a tensile mismatch stress, the face of the substrate bonded to the film becomes concave whereas, for a compressive mismatch stress, the face of the substrate bonded to the film becomes convex. An important property of this formula is that the relationship between curvature κ and membrane force f does not involve explicitly the properties of the film material.

3.3.2 Improvements of the formula

It's possible to improve the precision of this formula, extending it to different situations.
A first improvement is to extend it to an arbitrary film thickness. If h_f is the thickness of the film, one can find [8]:

$$\frac{\kappa_{impr}}{\kappa_{St}} = (1 + \frac{h_f}{h_s}) \left[1 + 4\frac{h_f}{h_s}\frac{M_f}{M_s} + 6\frac{h_f^2}{h_s^2}\frac{M_f}{M_s} + 4\frac{h_f^3}{h_s^3}\frac{M_f}{M_s} + \frac{h_f^4}{h_s^4}\frac{M_f^2}{M_s^2} \right]^{-1} \tag{3.2}$$

A further step is to apply this formula to a discontinuous film (like our system, constituted by a layer of patches with a certain gap between them). If the area of substrate's surface is A_s and the total area of the film is A_f, this approximate relation stands:

$$\tilde{\kappa} = \kappa_{impr}\frac{A_f}{A_s} \tag{3.3}$$

3.3.3 FE model validation

The validation is made on two different finite elements models. The first one is a circular plate with patches inside, the second one refers to the hexagonal system above defined (for

this second one see Figure 3.12).

The goal is to compare the curvature κ calculated with SAMCEF and the analytic value coming from the Stoney formula. Referring to Appendix C and to [8], one can say that:

$$f = N_p = -e_{31}V = -M_f d_{31}V \tag{3.4}$$

Owing to this equation, an electric tension of $1V$ is applied to all the patches. From SAMCEF we get the peak to valley (PV) excursion of the surface (i.e. the displacement of the central point of the model), and it's possible to obtain the value of κ easily (assuming a parabolic surface):

$$\kappa = 2\frac{PV}{R^2} \tag{3.5}$$

Table 3.2 compares the analytical and numerical results obtained with SAMCEF and with the several refinements of the Stoney formula.

/	κ_{samcef}	κ_{St}	κ_{impr}	$\tilde{\kappa}$	$Difference$
Conf. 1	$4.466e-04$	$9.852e-04$	$7.145e-04$	$4.818e-04$	7.872%
Conf. 2	$5.862e-04$	$9.852e-04$	$7.145e-04$	$5.780e-04$	1.387%

Tabella 3.2: Comparison of the curvature, computed with FEM and with refinements of the Stoney formula.

3.4 Experimental results

The goal of the measurements described below is to compare the actuation performances of a prototype of deformable segment with the results provided by a finite element model. The prototype is a 90mm segment.

In this section, all measurements are **relative**; the reference is the case when the electrodes of the patches are shortcut (V = 0V). This allows removing the permanent surface figure error of the segment emanating mainly from the Silicon wafer itself and from the gluing process.

3.4.1 Description of the test setup

The test setup uses a NIMO wavefront sensor, based on a technique called *phase-shift Schlieren*. This interferometric technique measures the slopes in the X and Y directions; the shape of the mirror is then determined by an integration performed by the software of the sensor. The support of the mirror is shown in Figure 3.14; the measurements of the actuation performance are done over a pupil of 76mm diameter to ease the post-treatment of the results.

3.4.2 Comparison of the results

The comparison is based on the influence functions of the mirror: a voltage of +60V is applied to a patch, and 0V to the other patches. This procedure is repeated for each patch. The segment is the same as that described in Section 3.1.1. The numerical model is the same as that described in Section 3.2. The only difference is related to the boundary conditions: to

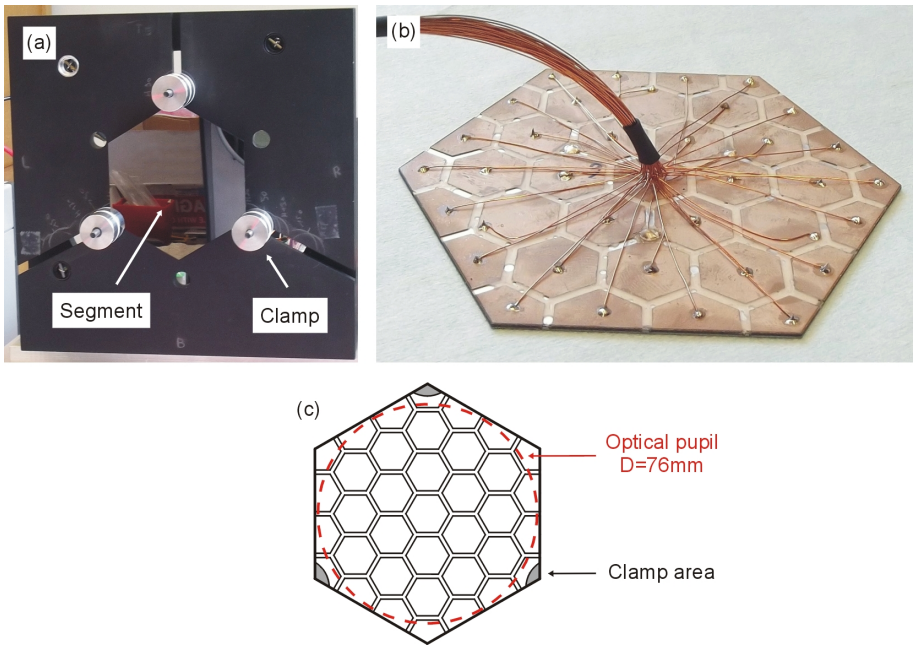

Figura 3.14: Support of the sample mirror: (a) Front view with the prototype clamped. (b) Back view of the mirror with its individual wires. (c) Characteristic dimensions of the optical pupil and of the effective clamp area.

approximate the effects of the clamp of the test bench (Figure 3.14), the six DOFs of three of the corner nodes are blocked. Several representative experimental and numerical results are compared in Table3.3 and Figure 3.15 to Figure 3.19.

In general, we notice a relatively good correspondence between the experimental and numerical results: both the shapes and the amplitudes correspond quite well in most cases. Some show larger discrepancies that may come from various sources:

- differences in terms of mechanical properties of the materials with respect to the data-sheets, and in terms of the actual geometry (thickness of the layers, in-plane dimensions and positions,..). These systematic errors mostly affect the amplitude without changing the shape; it can be removed by a proper calibration of the model from experimental measurements.
- imperfections in the control electronics used for the test, that cause slight differences between the actual voltages and those used for the simulations. Again, this only affects the amplitude and can be improved.
- imperfection in the modeling of the boundary conditions (the actual kinematics differs from that which is modeled), and potential insufficient tightening of the clamps on the test bench. This problem is expected to be of smaller importance when the segments will be mounted on the active feet described in Section 3.1.3, as shown by experimental tests.

Therefore, these raw results, obtained without any attempt of optimization, can be considered a good first-order validation of the mechanical behavior of the patches. Furthermore,

one should keep in mind that the nature of the control based on the influence functions will automatically compensate for any dispersion in the material, geometrical and kinematic characteristics of the system[2].

IF	Measurements [μm]		Numerical model [μm]	
	PV	**RMS**	**PV**	**RMS**
1	3.52	0.62	3.69	0.79
2	3.45	0.69	3.61	0.75
8	3.28	0.62	3.53	0.72
9	3.03	0.52	3.75	0.67
10	3.06	0.49	3.05	0.54
23	1.51	0.34	1.66	0.38
25	2.04	0.31	2.69	0.42

Tabella 3.3: Comparison of the PV and RMS values of the experimental and numerical influence functions.

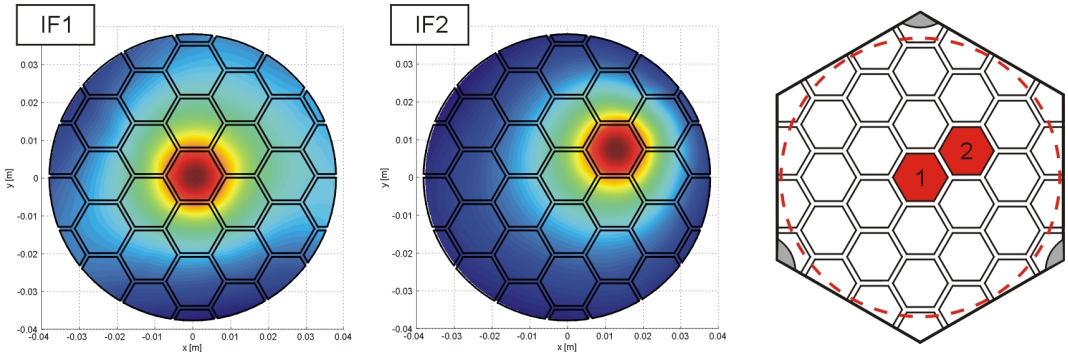

Figura 3.15: Influence functions 1 and 2: experimental results.

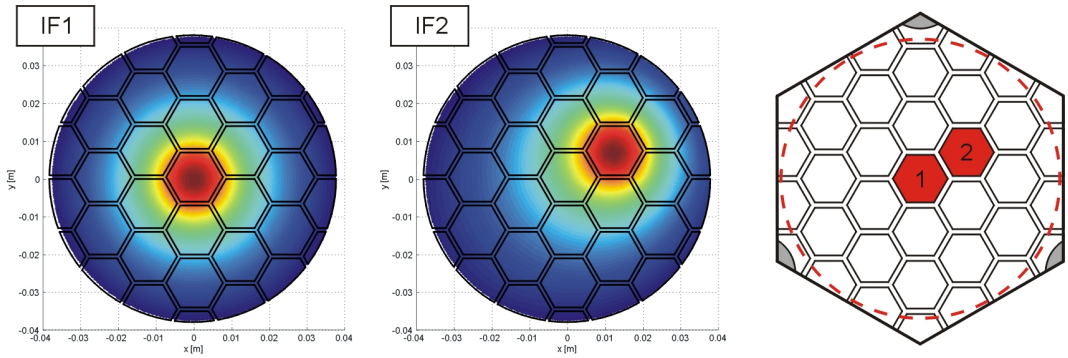

Figura 3.16: Influence functions 1 and 2: numerical results.

[2]Other similar comparisons, based on different configurations, geometries, wafers and patches have been and are still being made on a regular basis throughout the development of the prototypes described above; they show that a better monitoring of the experimental conditions can improve the correspondence. It is beyond the scope of this thesis to discuss these results.

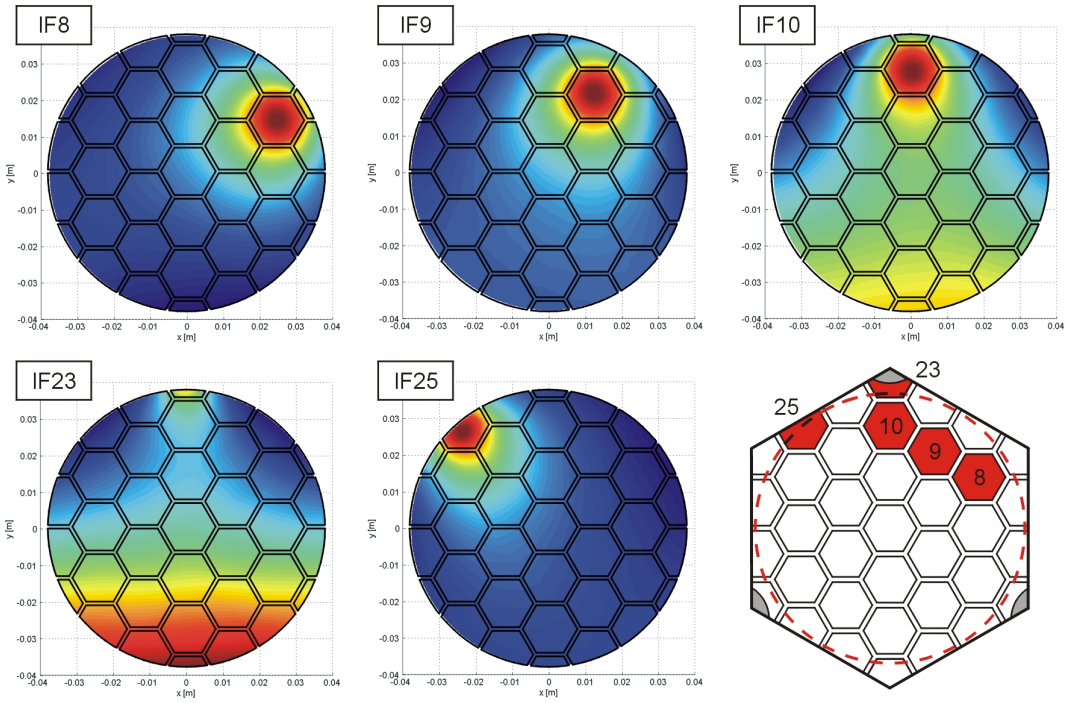

Figura 3.17: Influence functions 8, 9, 10, 23 and 25: experimental results.

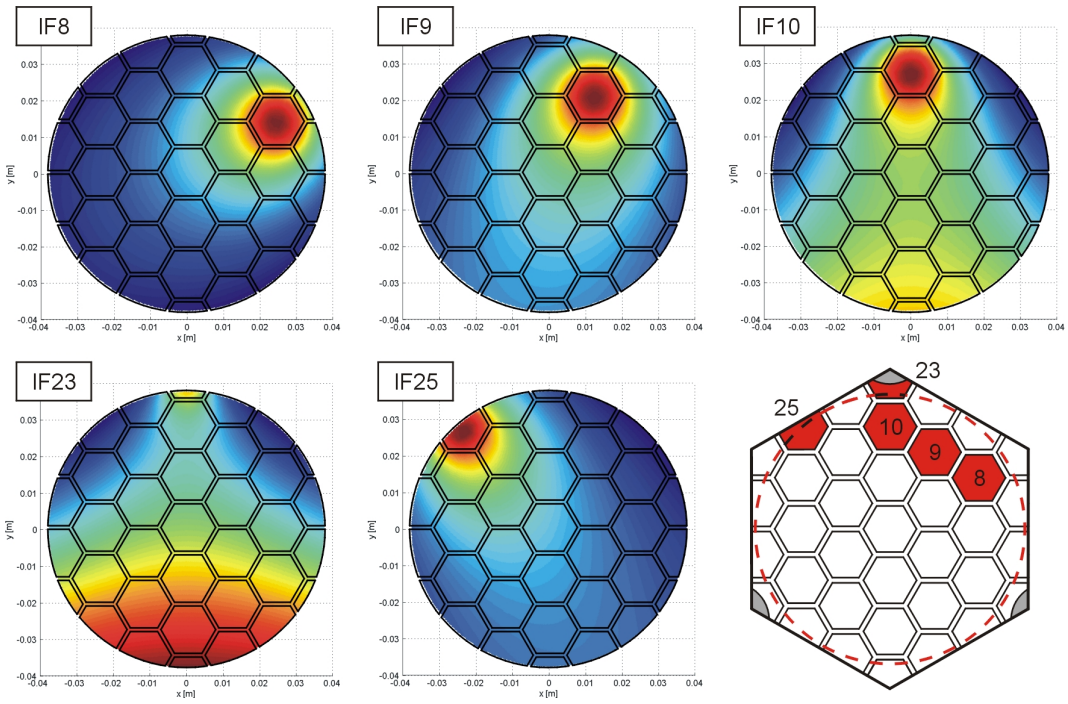

Figura 3.18: Influence functions 8, 9, 10, 23 and 25: numerical results.

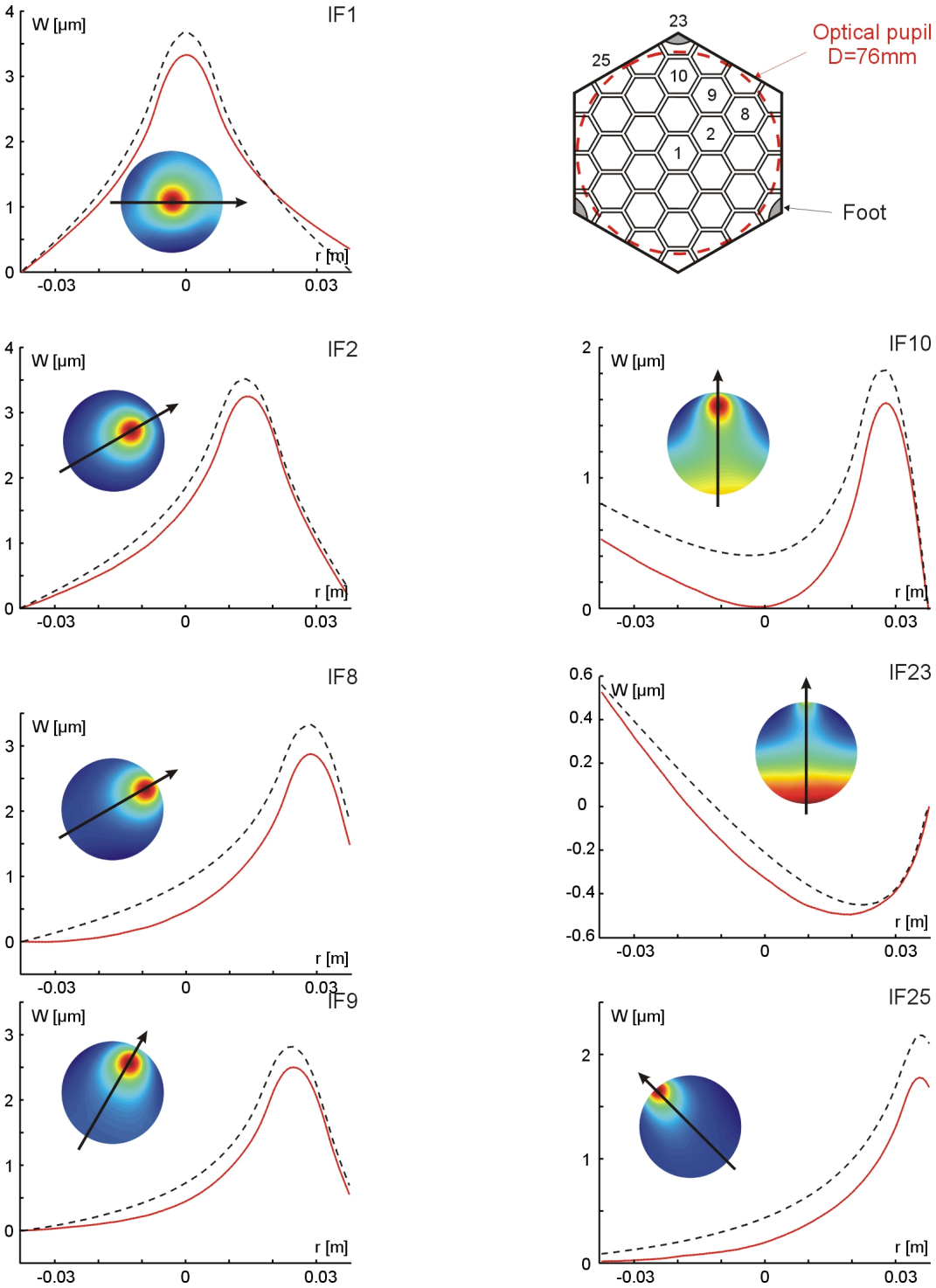

Figura 3.19: Comparison of the cross-sections of the influence functions measured experimentally (continuous line) and computed in SAMCEF (dashed line).

Capitolo 4

The control techniques

As mentioned in the previous chapters there are two distinct aspects to control: the morphing and the co-phasing of the segments. The approach followed here is based on the state-of-the-art sensors, which cannot measure at the same time both the shape and the phasing of the segments. This fact implies that we need to use the at least 2 sensors to achieve both the morphing and the co-phasing of the segments, and these two aspects of control operates independently.

By **morphing** we tackle the *shape control* of the surface, that is the possibility to deform *locally* the surface applying suitable voltages to the piezoelectric patches glued on the back of each segment. Commonly optical sensors allow to measure the slopes of the surface, and at this level of control we can get information on the local shape of the segment and on the average orientation of it.

The **co-phasing** between segments is achieved by modifying the voltages associated to the rigid-body actuators in order to guarantee the continuity of the whole surface: it is a *global* approach. The most part of the correction (we can roughly says more than the 90%) acts on the piston term, which is completely not sensed by the optical measurement system. It is then possible to act also on the tip-tilt components, to adjust local little differences between segments not well appreciated before, improving in general the continuity of the surface. Numerical simulations show that this second step of co-phasing has not a big impact on the final results, and its effective advantage could be evaluated from time to time.

In Figure 4.1 a schematic summary of the control steps is provided. In this chapter the two aspects of control will be analyzed in a more rigorous way, and in Chapter 5 the concepts described here will be applied to two different control strategies based on different sensing techniques.

4.1 Morphing

The goal of morphing is to compute the voltages to be applied to the PZT and the linear actuators (i.e. the active feet) in order to change the shape and orientation (the slope in general) of each segment *independently* to fit a specific target surface or shape.

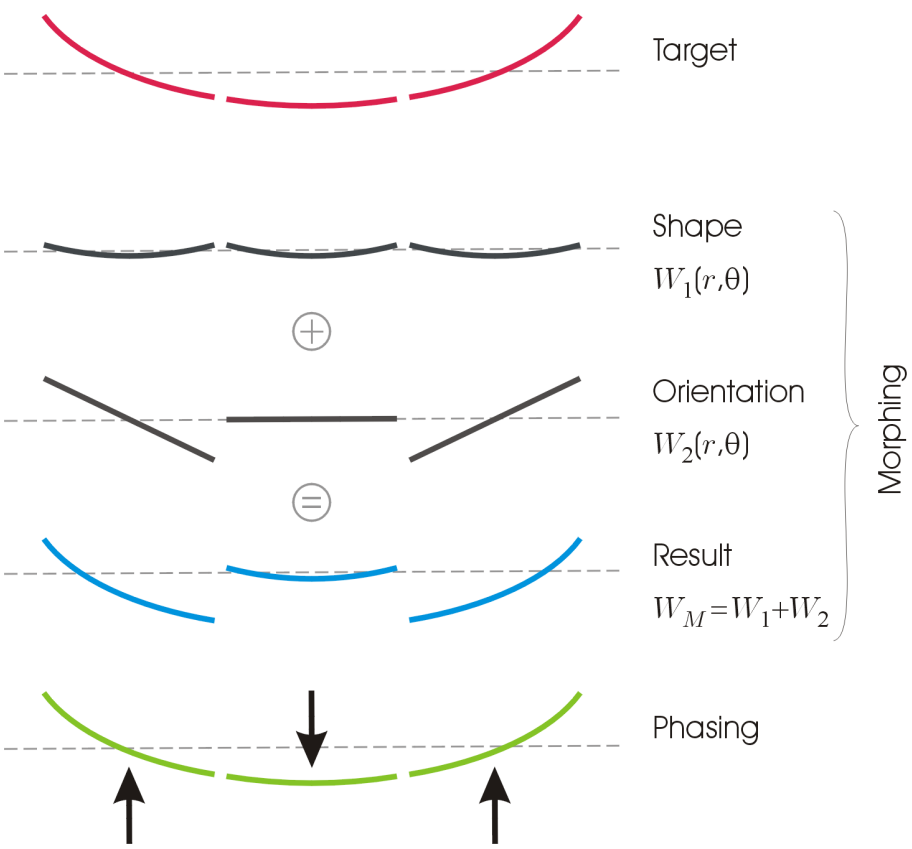

Figura 4.1: The target surface pictured in red at the top of the figure and the steps of control. During the morphing, the PZT actuators provide the curvature to segments and the feet the rigid orientation. Then with the co-phasing, the segments are adjusted to achieve the continuity of the surface. The dotted line represents the mean value of the surface.

Let us suppose N actuators per segment: in this number both piezoelectric actuators and linear rigid-body ones are included. For example in the system analyzed in Chapter 3, the number of piezoelectric actuators is 37 plus 3 rigid-body ones, for a total of $N = 40$. We suppose that we know M measurement points, provided by the chosen sensing method (in Chapter 5 two different measurement systems will be treated). For the moment no hypothesis on the relative amplitude between M and N is made. One can write this matrix equation:

$$w = \mathbf{J}v \tag{4.1}$$

where w is the vector (with dimensions $[M \times 1]$) containing the outputs of the measurement system (typically displacements or slopes, see Chapter 5), v contains the voltages applied to the actuators (both piezoelectric and rigid-body, and with dimensions $[N \times 1]$) and $\mathbf{J}$ is the so-called *Jacobian matrix* which is, in general, rectangular (so $[M \times N]$).

Considering Equation 4.1, $\mathbf{J}$ is built in this way:

$$\mathbf{J} = \{\, w_1 \ \ldots \ w_i \ \ldots \ w_N \,\} \tag{4.2}$$

where the w_i are vectors called the *influence functions* of the system, corresponding to the sensor signals obtained by applying a unit voltage in the i^{th}-position of v, the vector of voltages. This formulation for the Jacobian is easy to implement, robust with respect to deviations in the distribution of the characteristic incomplete systems, and so on.
The elements of v are ordered so that the voltages applied to the piezoelectric patches come first, and the last values correspond to the rigid-body actuators. For example, always referring to the system in Chapter 3, one can get:

$$v = \begin{Bmatrix} v_1 \\ \vdots \\ v_{37} \\ v_{rb1} \\ v_{rb2} \\ v_{rb3} \end{Bmatrix} \tag{4.3}$$

where $v_{rb,i}$ refers to the i^{th} rigid-body actuator.
It is important to underline that all the calculations are made segment by segment. It is possible, in general, to define the same quantities not in a local, but in a global way, that is with a block-diagonal matrix which includes all the segments together. For numerical stability of the problem, a better conditioning and a faster implementation, the local approach (segment-by-segment) is here used.

The control problem amounts to solving the inverse problem, which is to determine the best distribution of actuator signals (voltages), v_T, to approximate a surface shape projected in the sensor space, given by w_T. It requires the inversion of the Jacobian matrix $\mathbf{J}$. As pointed out above, in general $\mathbf{J}$ is rectangular, so the pseudo-inverse $\mathbf{J}^+$ of the Jacobian must be computed (see Appendix B):

$$v_T = \mathbf{J}^+ w_T \tag{4.4}$$

The computation of the pseudo-inverse can be performed using different methods. One can use the well known *Moore - Penrose* formulation:

$$\begin{aligned} w_T &= \mathbf{J} v_T \\ \mathbf{J}^T w_T &= \mathbf{J}^T \mathbf{J} v_T \\ v_T &= (\mathbf{J}^T \mathbf{J})^{-1} \mathbf{J}^T w_T \\ v_T &= \mathbf{J}^+ W_T \end{aligned} \tag{4.5}$$

In practice $(\mathbf{J}^T\mathbf{J})^{-1}$ is rarely well conditioned, and can even be singular, because the influence functions of the actuators might not be sufficiently different, especially in the presence of several deformable mirrors or in the case of actuators located far away from the optical aperture and with very low authority inside of it [30].

As described in Appendix B, the Singular Value Decomposition algorithm is an other approach to perform the pseudo-inverse. One can always write:

$$\mathbf{J} = \mathbf{U}\Sigma\mathbf{V}^T \tag{4.6}$$

where the column of $\mathbf{U}$ are the orthonormalized sensor modes, the columns of $\mathbf{V}$ are the orthonormalized actuators modes and Σ is a rectangular matrix which contains the singular values σ_i on its diagonal [1]. The pseudo-inverse is therefore:

$$\mathbf{J}^+ = \mathbf{V}\Sigma^{-1}\mathbf{U}^T \tag{4.7}$$

The diagonal matrix Σ^{-1} contains the inverse of the singular values, σ_i^{-1}, on its diagonal; it provides an equal authority on all singular value modes.
An important advantage of this technique is the possibility of doing a filtering of the eigenvalues in an easy way. In fact, using the Σ matrix, we have a direct knowledge of the magnitude of the singular values, and we can remove an arbitrary number of these values by removing the corresponding lines and columns from $\mathbf{U}$, $\mathbf{V}$ and Σ. Obviously, this procedure strongly affects the results (see Appendix B.2.1), and some practical examples will be provided in Chapter 5.

As already highlighted, the $\mathbf{J}$ matrix is in general rectangular. Reminding that N is the number of actuators (both piezoelectric and rigid-body ones) and M are the measurement points, three different situations can occur:

- $M < N$: there are more actuators than measurements points. This means that in general the components of the target surface at lower frequencies will be sensed, whereas the ones at higher frequencies may be lost or pollute the low frequencies. The effect is that the sensed surface is smoother than the real one, because the tendency (from the properties of the pseudo-inverse) is to minimize the RMS of the actuator signal, i.e. the voltage range.

- $M > N$: there are more measurement points than actuators. In this case the surface is sensed in a better, more precise way, and the pseudo-inverse will minimize the RMS error of the surface without regards for the voltage range that can become larger. The risk is that the PZT's will do their best to match even the high frequency components,

potentially by adopting large, unbalanced distributions of the voltages which is not bound in this configuration.

- $M = N$: this is the only configuration with an exact solution, and not a least squares one. This fact does not mean that the solution is perfect, in fact one can get both the two problems explained in the previous cases, and we know that no one of these two parameters is optimized.

There is not a more advantageous configuration, it depends on the situation in which the pseudo-inverse is used, and which quantity we want to minimize. In our case, in general, we have $M > N$, that is the goal is to minimize the RMS of the surface. The problem is that the rank of $\mathbf{J}$, denoted by r, could be inferior than M (so $r < M$). Mathematically speaking this means that some columns of $\mathbf{J}$ are not orthogonal to the others. From the point of view of physics, the sensing method cannot make an obvious difference between some of the Influence Functions (IF). A filtering is necessary to cut off the singular values that generate these not orthogonal columns.

One example is given in [1]. Figure 4.2 shows a typical distribution of the singular values of

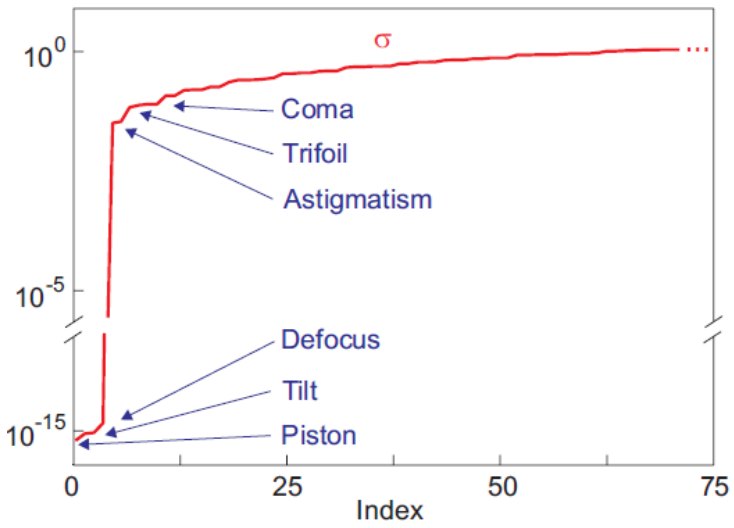

Figura 4.2: Singular values of the Jacobian, ranked by increasing values.

the Jacobian matrix for the phasing control of rigid segments, with the relative displacements between segments monitored by the edge sensors (in this particular case the mirror was composed of 91 segments and supported by a truss). The singular values are ranked by increasing values; one sees that the lowest singular values correspond to the lowest optical modes, piston, tilts and defocus, which are unobservable from the sensors used in this study ($\sigma_{1-3} \simeq 0$), and the modes with the lowest singular values next to them are astigmatism, trefoil and coma (that is the following three Zernike polynomials, see Appendix A). A filtering of these first three singular values close to zero is necessary to get a well conditioned matrix and avoid aberrant results from the pseudo-inverse.

4.1.1 Principles of filtering

It is possible to improve the results given by the pseudo-inverse by applying a filtering bond on the singular values. We can write Equation 4.7 in a different fashion [19]:

$$\mathbf{J}^{+} = \sum_{i=1}^{r} \sigma_i^{-1} u_i^T v_i \tag{4.8}$$

where r is the rank of the Jacobian matrix. In this reconstruction, it is always possible to decide not to use one or more singular values of $\mathbf{J}$ (and the correspondent actuator and sensor modes), and to restrict the sum of Equation 4.8 to the other terms of interest. In practise, in most cases, the filtering is based on the examination of the distribution of the singular values: those with largest value correspond to actuator modes with big authority and that are well sensed by the sensors; conversely, a low value indicates either a low authority and a poor sensing, which may result in a lower rank of $\mathbf{J}$ and cause the voltage range to be large because of the inversion of the corresponding low values of σ_i in Equation 4.8.
In our approach, we compute the normalized distribution σ_i/σ_{max}, ordered in descending order, and eliminate the modes with normalized singular values smaller than a certain threshold, that is a function of the characteristics of the mirror and of the sensor. In practise, this is done by restricting Equation 4.7 to the sub-matrices $\mathbf{U}$, Σ and $\mathbf{V}$ involving only the retained singular values and the corresponding modes. This leads to a loss of accuracy of the results in term of morphing as it amounts to remove some actuation modes from the space of effective degrees of freedom available for control. However, this leads also to a reduction in the voltage range as Equation 4.8 does not involve anymore inverting very small values of σ^{-1}.

4.2 Phasing

Referring to Figure 4.1, the phasing is the last step of the control. The goal of this control technique is to adjust the value of voltages in the rigid-body actuators, in order to achieve a continuous surface. In particular it compensates for mostly the piston error, i.e. the purely rigid motion in the direction normal to the reference plane, and then it also adjusts the tip-tilt components, that is the (rigid) slopes of the segments. As already pointed out at the beginning of this chapter, this is not a local approach, as it must consider the system as a whole. The corrections for all the segments are computed together to get the desired continuity of the surface they form.

4.2.1 Measuring the phasing

There are different methods to perform the measurements of phase steps between segments. There is not a general criterion for the choice of the sensing method, it strongly depends on the system and on its feasibility. In Chapter 2, two different approaches are described, each one related to a particular sensor. Let us now see how they can be applied to the system studied in this thesis.

Edge Sensors

The basic principles of the edge sensors are described in Chapter 2.3.2. In the numerical model, we started by modeling a sensor giving pointwise measurements of phase steps bet-

ween neighboring segments. This is equivalent to virtual, ideal, edge sensors that would be compatible with the segmented DM described here (in reality, as explained in Chapter 2.3.2, the use of edge sensors in this system is not possible).

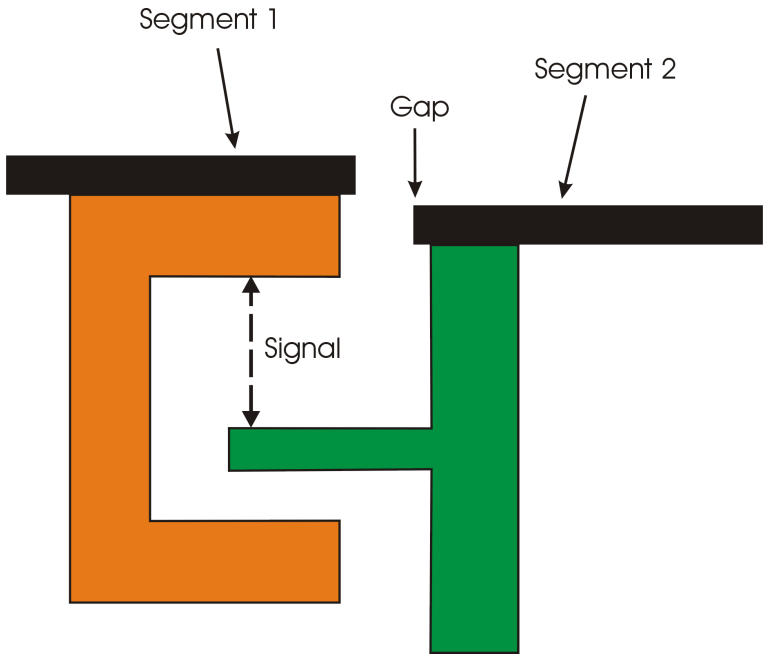

Figura 4.3: A simple scheme of a (capacitive) edge sensor. The signal is the relative distance between the two parts of the device. Let us notice the small gaps due to mounting between the device and the edge of the segments: this may induce some error if the effective measurement is not exactly centered on the edge (see Chapter 2.3.2).

Referring to Figure 4.3, we see that the output signal from the measurements devices is computed as difference between two parts: one, denoted as *edge sensor*, connected to a segment and the second one, called *coupled part*, connected to an adjacent segment.
Here we suppose there is 1 edge sensor per edge, and that the gap between segments is 4% of the flat-to-flat diameter of the segment. This is illustrated in Figure 4.4. It is important to underline that if some edge sensors are outside the optical pupil, they are considered as deactivated, so we get no signals from them.
Using this method, we get 2 measurements per edge, in order to get not only a piston difference between two adjacent segments, but also the relative slopes between them, that is how much a segment is tilted with respect to its neighbor. We must remind that this are global measurements, and they refers to the rigid global inclination of a segment respect to its related one. This means also that, having only two measurements points per edge, the results could potentially be affected by local curvatures due to the surface morphing.

Zernike Phase Contrast Sensor (ZPCS)

The theoretical basis of this sensor is described in Chapter 2.3.3, and for further information the reader should refer to [37].

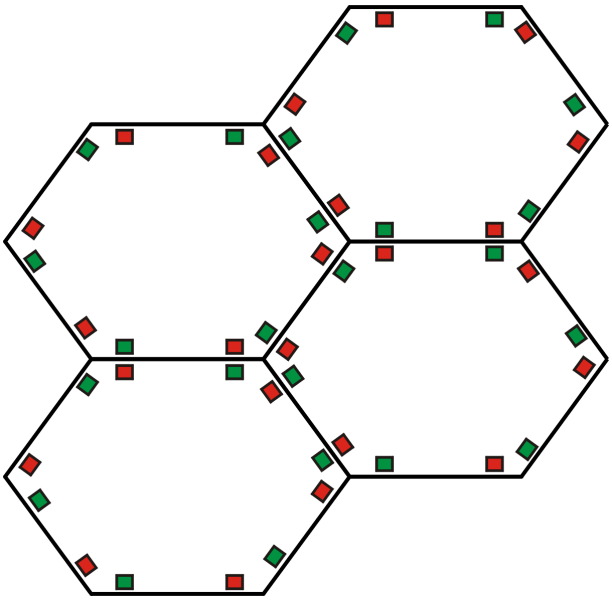

Figura 4.4: Example of edge sensors distribution on 4 adjacent segments. Each edge sensor is made by two parts, indicated by coupled green and red rectangles.

As already mentioned in Chapter 2.3.3, in our numerical model this sensor is simulated using 8 measurements points per edge. But also other configurations are been studied.

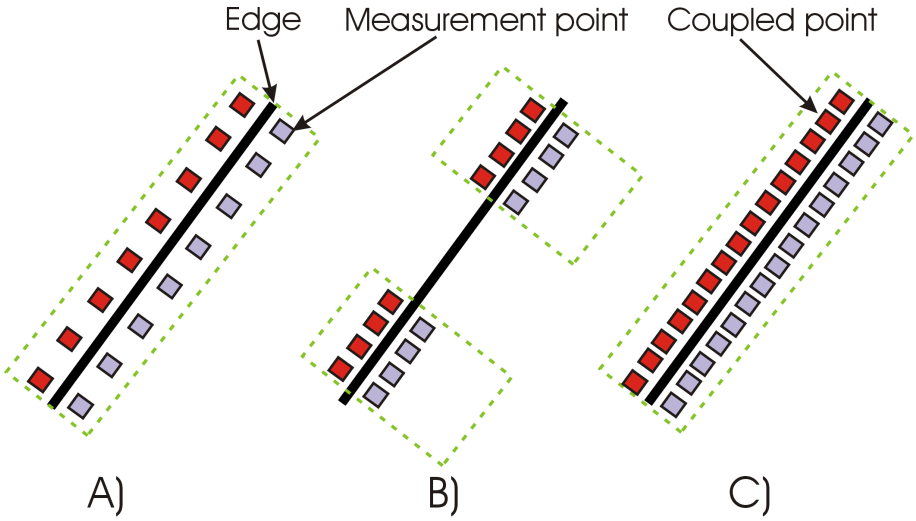

Figura 4.5: The three configuration analyzed for the Zernike Phase Contrast Sensor. A) 8 points equally distributed along the edge. B) 8 points spread in two groups. C) 16 points equally distributed. The green rectangles indicate the points used to calculate the average values. Coupled points in red.

As already explained in Chapter 2.3.3, this optical sensor measures the phase steps along the edges of 2 neighboring segments in a continuous fashion (this can be seen as a set of virtual ESs distributed continuously along the edge). The information is then averaged over one or more areas. Therefore, in the numerical model, we choose to model it in a fashion similar to

the ESs, with the exception that we consider more measurements points, and that we group some of them to compute average signals. In Figure 4.5 are depicted three different situations used to simulate the ZPCS. In configurations A) and C) we take 8 and 16 points per edge respectively, and we perform an average value on the relative displacements calculated per each sensing point on the edges. In this way a unique average value is calculated per edge. In configuration B) the measurements points are spread in two groups per edge, and two average value (one per group of points) are calculated along each edge (a result closer to the one obtained with the edge sensors above described). The goal of the average calculation is to (partially) consider the deformations of the surface and so to get more precise values, less influenced by the local shape of the surface due to morphing.

Both the three configurations are been applied to all the cases of study, and no appreciable differences exist between them for the results. Therefore, in general, for the calculations in this thesis we suppose to always use configuration A) depicted in Figure 4.5 (so 8 measurement points and 1 average value per edge).

Doing a comparison between the edge sensors and the ZPCS, one can see that the results for the phasing are improved using the second device. This is mainly due to the average procedure in the ZPCS, which allows to consider the effects of the local shape of segments. So, if unless stated otherwise, the simulation always use the ZPCS model to perform the phasing between segments.

4.2.2 General procedure

The procedure explained here is general and can be applied to any configuration. We illustrate the theoretical explanation with a practical example, using a configuration with 19 hexagonal segments and 40 actuators per segment (37 piezoelectric actuators plus 3 rigid-body ones). As stated above, we suppose that we use a ZPCS, with 8 measurement points per edge and 1 averaged over one area per edge.

The phasing control starts with a fundamental equation:

$$S_s = \mathbf{J}_s^{gl}\, v^{gl} \tag{4.9}$$

where S_s is the vector with the relative signals associated to each edge inside the optical pupil (in the example its dimensions are $[42 \times 1]$), v^{gl} is the vector which contains the voltages associated to all the actuators, that is the structure of Equation 4.3 is repeated segment by segment (with dimensions $[760 \times 1]$), and $\mathbf{J}_s^{gl}$ is the global Jacobian matrix that relates them. It gives the influence of *any* actuator of the system (both piezoelectric and rigid-body ones) on the averaged phase signal as seen by the ZPCS. It dimensions are $[42 \times 760]$. It is built according to the following procedure:

- In a way similar to Equation 4.1, the numerical model gives us access to the displacements of any point of the segment under the influence of its N actuators (40 here). This Jacobian matrix can be restricted to Z, the absolute displacement of the 6×8 points of interest for the ZPCS, and will be identical for all the segments as they are identical themselves. We denote this Jacobian by $\mathbf{J}_z$, with dimensions $[48 \times 40]$. At this

stage we should emphasize that $\mathbf{J}_z$ contains absolute displacements only, not relative displacements suitable for the ZPCS. So we can write:

$$Z_i = \mathbf{J}_z \, v^i \tag{4.10}$$

where the index i refers to the segment index.

- We build a global Jacobian matrix, $\mathbf{J}_z^{gl}$, that contains the absolute displacements of all the segments under the effects of all the actuators:

$$Z^{gl} = \mathbf{J}_z^{gl} \, v^{gl} \tag{4.11}$$

where Z^{gl} is a vector that contains the absolute displacements of all the segments, $z^{gl} = \{z_1 \dots z_i \dots z_{19}\}^T$, v^{gl} is the vector defined above and $\mathbf{J}_z^{gl}$ is a block diagonal matrix given by:

$$\mathbf{J}_z^{gl} = \begin{bmatrix} (\mathbf{J}_z)_1 & & & & \\ & \ddots & & & \\ & & (\mathbf{J}_z)_i & & \\ & & & \ddots & \\ & & & & (\mathbf{J}_z)_{19} \end{bmatrix} \tag{4.12}$$

The index of the segment, i, is given for clarity but the reader should remember that these sub-matrices are all identical.

- The next step applies a linear transformation to compute the averaged ZPCS signals, denoted by S, from the absolute displacements z^{gl}. This operation is performed by a mapping (or shape) matrix, $\mathbf{M}$, populated of 0, +1/8 and -1/8 to select the pairing points and compute the average at the same time (1/8 because in this example we have 8 signals per area):

$$S = \mathbf{M} \, z^{gl} = \mathbf{M} \, \mathbf{J}_z^{gl} \, v^{gl} = \mathbf{J}_s^{gl} \, v^{gl} \tag{4.13}$$

which correspond to Equation 4.9.

This procedure is general and can also be adapted for edge sensors or other configurations of the ZPCS.

Piston correction

From $\mathbf{J}_s^{gl}$ it is possible to extract the sub-matrix which refers only to the piston value of the rigid-body actuators. To do this, it is sufficient to take the 3 columns of each segment associated to the rigid-body actuators, and then sum them. Following this procedure we get a new matrix $\mathbf{J}_{s,P}^{gl}$, where P means piston, with dimensions $[42 \times 19]$. We can perform the

pseudo-inverse of this matrix[1], denoted by $(\mathbf{J}^{gl}_{s,P})^{+}$, and then compute the voltages associated to the pure piston components using:

$$v_P = (\mathbf{J}^{gl}_{s,P})^{+} S_s \tag{4.14}$$

where the dimensions of v_P are $[19 \times 1]$, that is one value per segment. Given that it is a rigid-body motion, the piston component acts only on the last three components of the voltages vector. By definition it has the same value for all the three rigid-body actuators in each segment. v_p is then used to correct the piston, segment by segment, by subtracting it from the voltages associated to the corresponding rigid-body actuators. With these modified values of voltages, it is possible to calculate the new signals in the edges, like in Equation 4.9 and check the improvement of the results (in Chapter 5 there are many numerical examples).

Tip-Tilt correction

The procedure to correct the voltages also from the point of view of the tip and tilt rigid motions is similar to that described for the piston correction, except for two differences: the first one is that the voltages at the starting point are the ones already corrected by the piston control, the second one is the building of $\mathbf{J}^{gl}_{s,TT}$, the matrix used for the correction. In a fashion similar to the piston case, we build tip and tilt influence functions by a proper linear combination of the columns corresponding to the rigid-body actuators of the corresponding segment. The combination differs for tip and tilt; the coefficients are a function of the geometry of the system only.
From these computations one can build a matrix, that now we denote with $\mathbf{J}^{gl}_{s,TT}$, with dimensions $[42 \times 38]$, where 38 is the number of segments times 2 (because we get two columns per segment, one for tip and one for tilt). Except for these 2 differences, the procedure is exactly the same.

In general the effect of this correction appears smaller than that of the piston correction, but in most cases, it has at least a positive effect, so for the calculations carried out in Chapter 5 this second step of control is also used.

[1] An easy procedure to improve the conditioning of this kind of matrix is to add a line of ones at the bottom (see [37]). As a consequence, the matrix will have an extra line, so the new dimensions of $\mathbf{J}^{gl}_{s,P}$ are $[43 \times 19]$. If this modification is used, it is then necessary to add a zero at the end of the S_s vector. This amounts to forcing the average piston to remain 0. Alternatively, to improve the conditioning, it is possible to remove the piston singular value by a proper filtering.

Capitolo 5

Two approaches for control

The purpose of this chapter is to show two practical applications of the theoretical concepts of control explained in Chapter 4. One approach is based on the knowledge of the absolute displacements of certain points inside the segment, the second one is based on the measurements of the slopes provided by a Shack-Hartmann sensor.

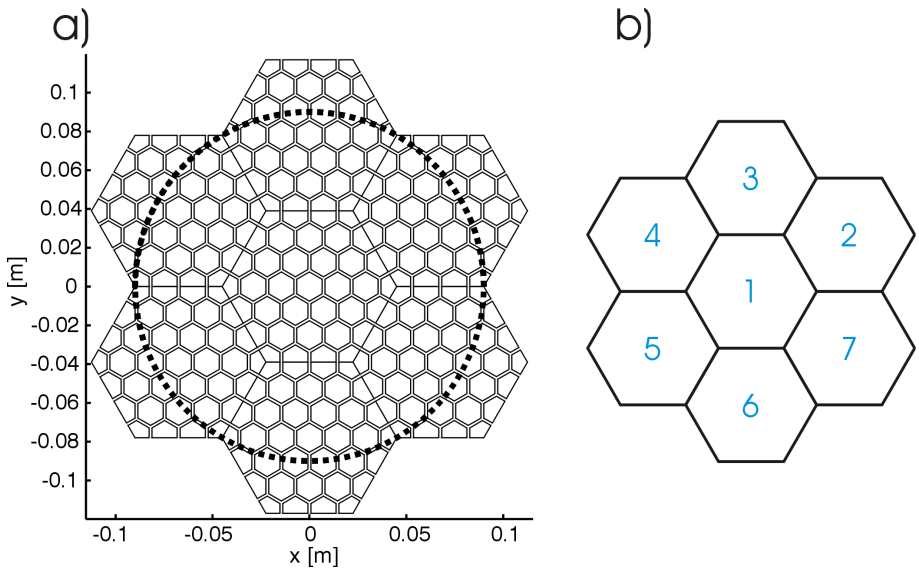

Figura 5.1: a) The geometry of the reference configuration: 7 segments and 37 piezoelectric patches per segment. b) Numbering of the segments.

In Figure 5.1, the configuration taken as reference is depicted. It is composed of 7 segments, and each segment has 37 piezoelectric actuators, plus 3 rigid-body actuators (not represented in the figure). The dotted line represents the optical pupil, that is the effective part of the segmented mirror used (hit by the light) in the telescope. This also means that the target shapes for the surface will be defined over this area.
Except for the central segment, none of the segments of the external crown are completely inside the optical pupil. The patches outside the optical pupil, however, contribute to the morphing of the whole segment. Later in this chapter, the effect of these external patches will be discussed with more details.

5.1 Control with displacement sensor

The first strategy analyzed here is based on the knowledge of the displacements of certain points inside each segment. We create a grid, a mesh of points (with 1141 points per segment, it is quite dense) and we suppose that we use an ideal sensor which can provide the value of the displacement of each point of the grid. Following the mathematical procedure explained in Chapter 4, we take the IFs (we recall that they are calculated applying 1V to a patch and 0V to the others) from the FE simulation (in SAMCEF) and we interpolate these IFs over the points of the sensor mesh (see Figure 5.2). As written above, the mesh is composed of 1141 points per segment, but it is important to underline that the points outside the optical pupil are not considered for the interpolation (so, in the reference configuration, only the central segment is completely inside the optical pupil and uses all the points of the mesh).

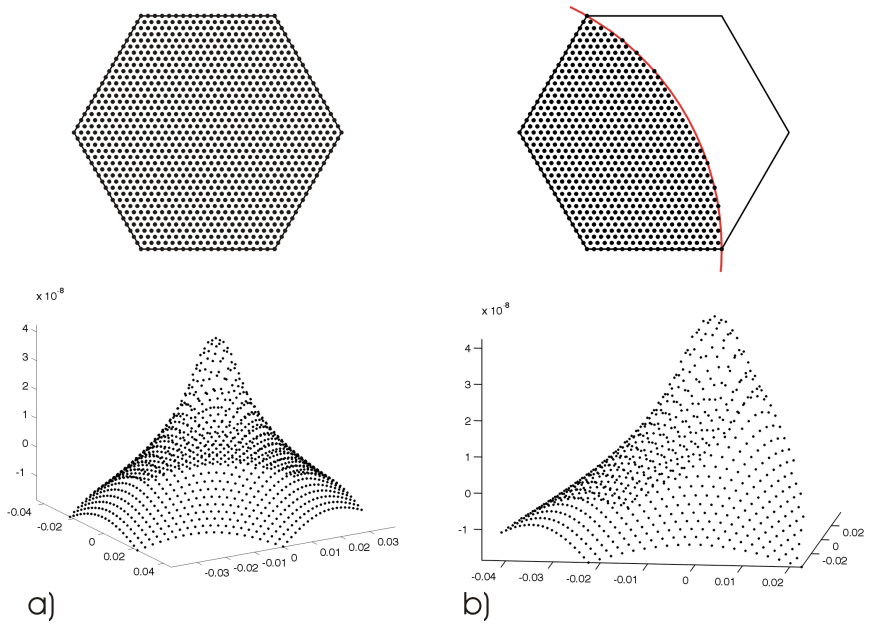

Figura 5.2: a) Influence function for the central segment applying 1V to the central patch. b) Influence function for segment number 2 applying 1V to the central patch. The corresponding meshes are displayed above.

From this procedure we get the vector w_i for each actuator i, which contains the displacements, and we can build the Jacobian matrix **J** as described in Equation 4.2. This Jacobian matrix is valid for all the segments (true in general, but for the segments partially outside the optical pupil only the lines of the Jacobian correspondent to the active measurement points are considered, see Figure 5.2) and links the voltages in the actuators to the displacements of the surface.

5.1.1 Singular values

As already described in Chapter 4.2.2, an important step of the control concerns the pseudo-inverse matrix of the Jacobian. Using the method based on the SVD (see Appendix B and Chapter 4.1), we directly have access to the singular values (also called eigenvalues), that are

the diagonal components of the Σ matrix.

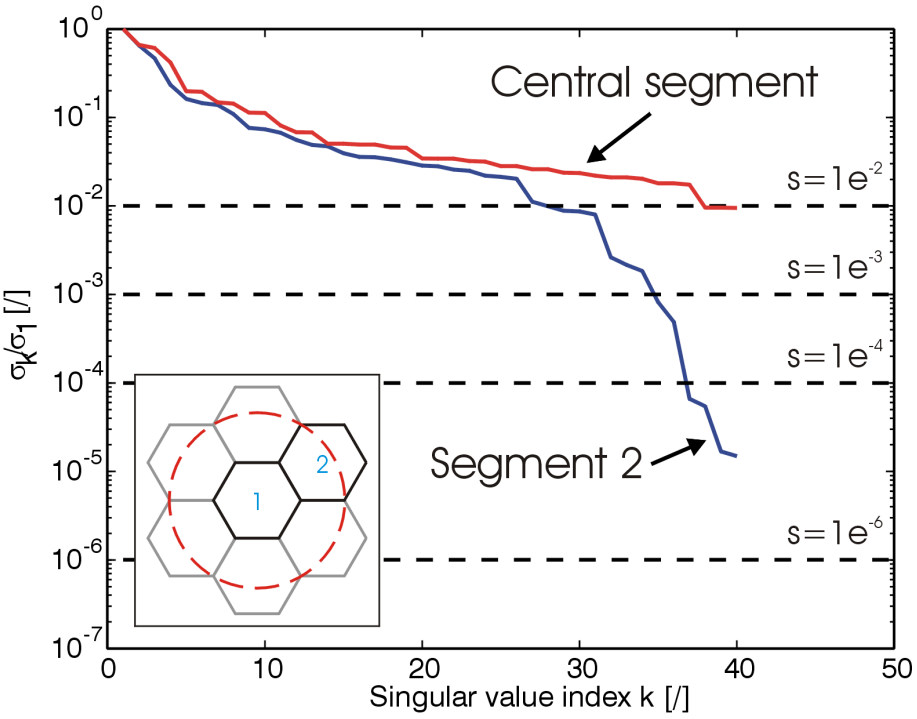

Figura 5.3: Singular values distributions for the central segment and for segment number 2 (see Figure 5.1 for the numbering of the segments). The dotted black lines are the thresholds for the filtering.

In Figure 5.3 the singular value distributions for segments 1 and 2 are provided. Numerically, the distributions of singular values of the external segments are all very close (except for negligible variations)[1] to that of segment 2.
From Figure 5.3, one can directly see how the central segment has a better distribution of singular values, that is the overall distribution has a much smaller variation, and in particular the minimum singular value of the central segment is approximately 3 orders of magnitude larger than that of segment 2. Looking at the thresholds in Figure 5.3, it is easy to notice how the effect of filtering mostly affects the external segments, unless we use a cutting level for the eigenvalues around 10^{-2}. We remind that the basic principles of filtering are explained in Chapter 4.1.1. In the following section we will see with an example how the filtering level affects the shape and in particular the parts of the segments outside the optical pupil.

5.1.2 Example: Astigmatism

As an example of the effect of the filtering of the singular values, we take Astigmatism as the target surface for the system (see Appendix A, about Zernike modes). The peak-to-valley

[1]The results are really close to each other mainly because the number of measurement points and their position inside each segment is roughly the same because of the 60° symmetry of the geometry. This is not necessarily true for configurations with more segments, because there will be different symmetries for the external segments, resulting in groups of segments with similar distributions of singular values that can exhibit non-negligible differences from one group to one other.

amplitude of the target surface is chosen to be $10^{-6}\mu m$.

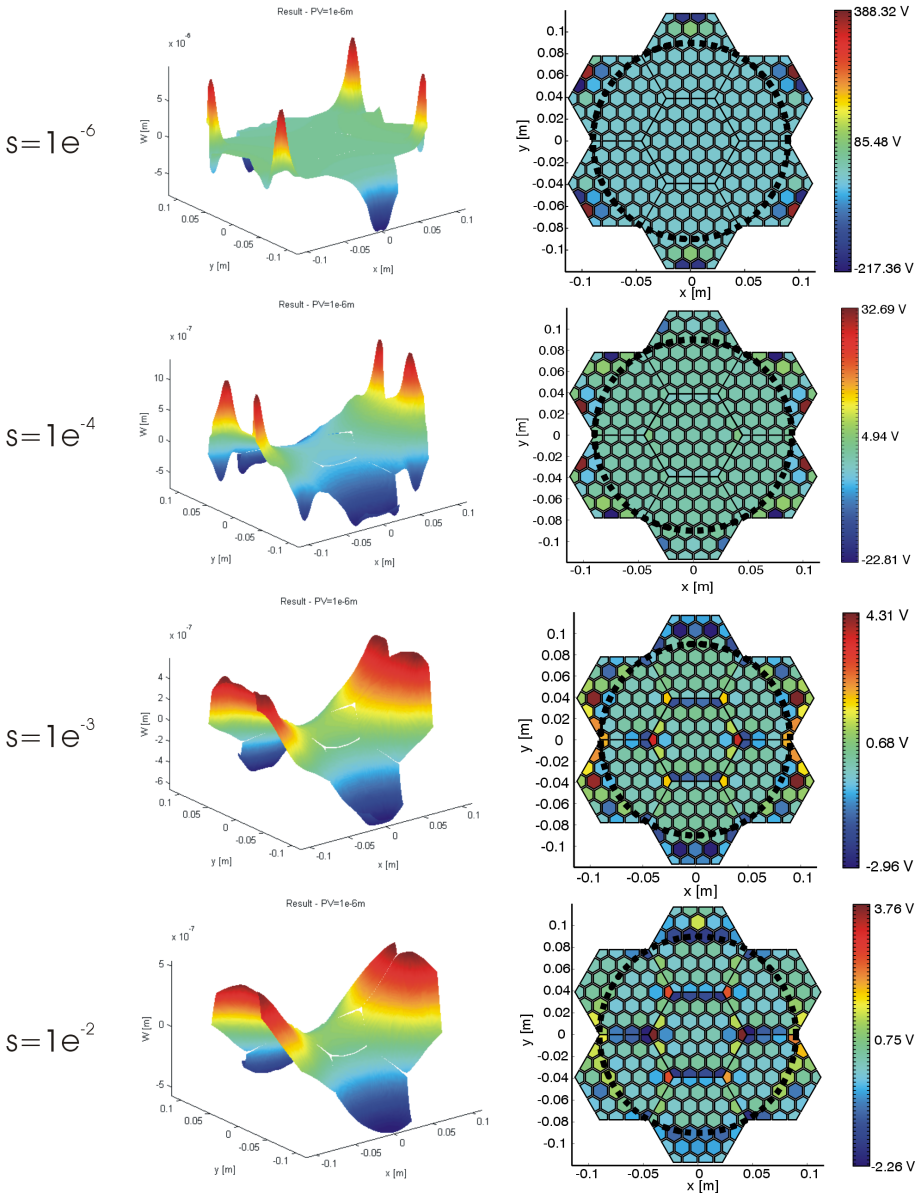

Figura 5.4: The effect of filtering on the system. The threshold levels for the filtering are the same shown in Figure 5.3. In the left column we see the evolution of the resulting shape, in the right one the correspondent voltage maps are provided.

In Figure 5.4 we see the effects of the filtering on the results (of the system). We can see that the higher the threshold for the singular values rejection, the smaller the bending of the external segments. In particular the parts of the external segments that are outside the optical pupil are the most affected by the filtering. Starting from a configuration with a threshold (equal to 10^{-6}) which does not filter any singular value, and in which the bending of the external segments is too exaggerated to be performed by a real system, we gradually

switch to a flatter, smoother surface. It is important to look in parallel at the evolution of the voltage map: the first configuration presents the largest absolute values for the voltages (above the technical limit voltage of 400V), but as the filtering level increases the voltage range tends to decrease significantly. For low values of filtering, the highest voltages are distributed (in a symmetrical fashion) outside the optical pupil, and they are the cause of the excessive bending described above. In particular, one can see that there are *voltage dipoles*, in the sense that the patches with the highest positive voltages are located next to them with the largest negative voltages, creating large local deformations outside the optical pupil, but that balance each other when seen from inside the optical pupil. Therefore this is considered as an aberrant result. Both effects are due to the pseudo-inverse. This behavior is typical of a badly conditioned Jacobian matrix, i.e. it is associated to the actuation and sensing modes with the lowest singular values. Physically, in our system, it emanates from the presence of actuators that, at the same time, are outside the optical pupil and have a moderate authority: the problem in mostly due to the smallest patches along the edges; the full patches near the optical pupil tend, on the contrary, to slightly improve the morphing capability by introducing more degrees of freedom in the system without introducing more constraints in the equations. As a result, it is difficult for the sensor to discriminate between the IF of mesh patches as, when see from the inside of the pupil, they are quite weak and the differences in the spatial distribution are small. This leads to several columns being almost linear combinations of each other (and in the worst cases also close to 0), inducing a decrease in the rank of the Jacobian matrix.
By filtering out the singular values associated to these problematic actuator modes (i.e. linear combination of actuators involving the problematic ones), we somehow remove them from the space of available degrees of freedom, leading to an improvement of the voltage range (ΔV) at the cost of a loss of precision in the morphing (less degrees of freedom); however, in most cases, for reasonable filtering levels, the benefit on ΔV are much bigger than the decrease of the surface quality, as shown below.

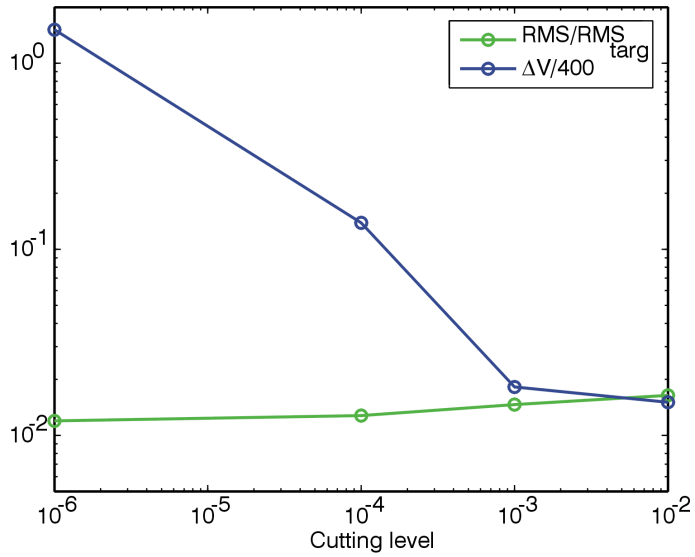

Figura 5.5: The trend of the RMS and the voltage range for different threshold levels. The RMS is normalized over the RMS of the target surface and the voltage range is divided by the maximum allowed voltage, equal to 400 V for the patches considered here.

One can see in Figure 5.5 that the voltage range decreases (which is desirable as it minimizes the portion of the voltage range used to generate a surface with a given amplitude and shape), but the RMS increases (which is not desirable, as it correspond to larger overall surface error). Thus, in general for the this configuration using a displacement sensor, a threshold of 10^{-3} is a good value as it is a good compromise for both criteria. We see that this does not affect the singular values of the central segment, and it is possible to demonstrate numerically that it is not a strict value, as it is quite robust to variations in its vicinity. This fact will not be verified with the Shack-Hartmann sensor: in that case the tuning of the filter is much more sensitive, and it basically depends on the density of sensing point over the segments (we will see that with the Shack-Hartmann sensor the cutting level must be set at the lower singular value of the central segment, that is the filter preserves all the singular values of the central segment).

5.1.3 General Results

In Section 5.1.2 we have chosen a threshold equal to 10^{-3} for the filtering of the singular values.

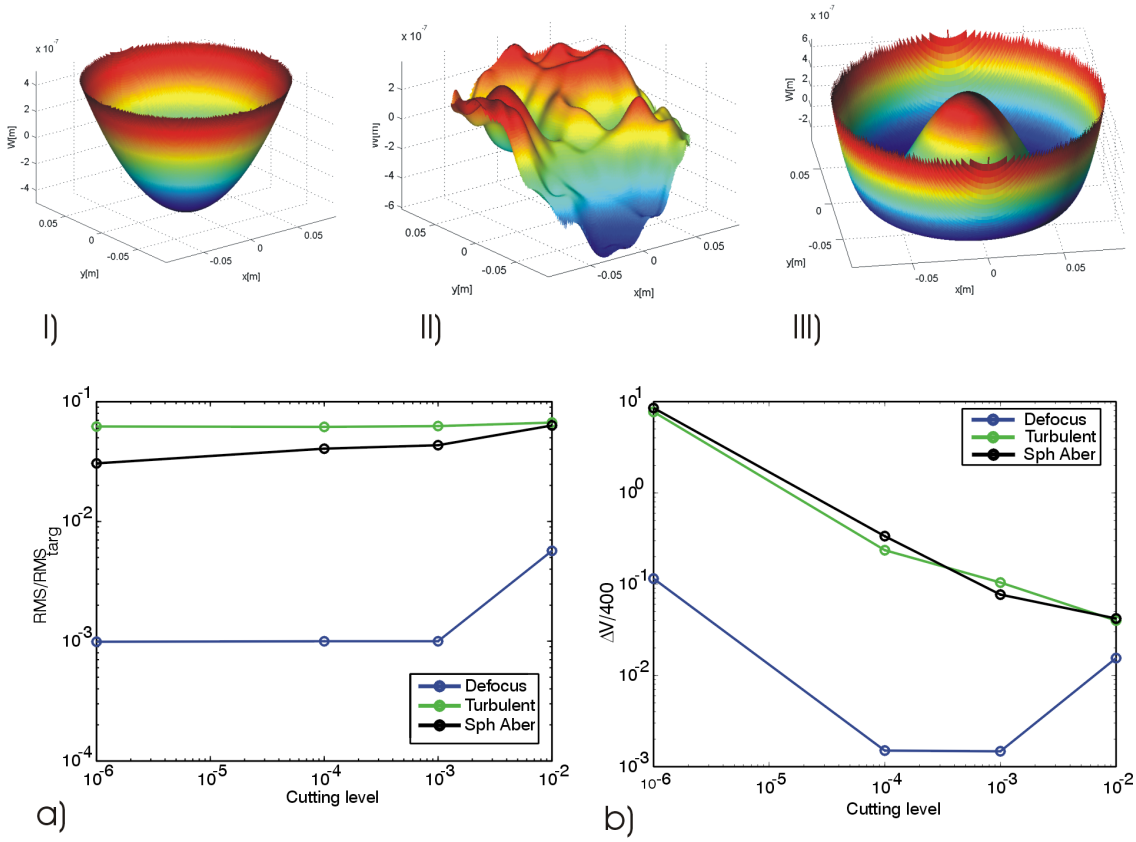

Figura 5.6: Target surfaces: Defocus (I), Spherical Aberration (II) and turbulent screen (III). They are defined over the area of the optical pupil and their peak-to-valley amplitude is $10^{-6}\mu m$. a) The trend of the RMS, normalized over the RMS of the target. b) The trend of the voltage ranges, normalized over the maximum allowed voltage of 400V.

Figure 5.6 shows the results for three different target surfaces: Defocus, Spherical Aberration and a turbulent screen. The first 2 could be represented by suitable Zernike Polynomials, and are quite common aberrations in the mirrors. The third one is a surface generated with the theory of Kolmogorov turbulence (see Chapter 2.2), and it is a realistic method for evaluating the performances of the mirror for AO. The results confirm that the level of 10^{-3} is a reasonable level for the filtering, in order to get good results both for the RMS and the voltage range. As already described, this value admits certain tolerances, it is not too strict, and allow to preserve all the singular values of the central segment.

In Figure 5.7 the results of the three cases are illustrated, showing the resulting shape and the corresponding voltage ranges. These results are calculated using a threshold level of 10^{-3}.

As a final remark, we can also say that this approach is also valid for configurations with more segments. The principle of filtering is basically the same and the threshold level used for the 7 segments configuration is applicable to a generic number of segments. As a general tendency, one can notice that the most problematic segments from a conditioning point of view are usually those with the largest part of the area outside the optical pupil. The results for a configuration with 19 segments are depicted in Figure 5.8. The difference between the two Astigmatism in the Figure is due to the different orientations in space of the main diagonals of the target surface.

5.1.4 Configuration with split-corners

This configuration is briefly described in Chapter 3.2. Instead of a single patch in the corner, this configuration presents two symmetrical patches. As already explained, we will not use this configuration because of its practical disadvantages. From a control point of view, it can be demonstrated that split corners lead to a larger voltage range than that of the full corners for the same target and no filtering. Furthermore, it is interesting to notice that the electrical dipoles and aberrant voltages are mostly concentrated at the split corners. Finally, the split corners also lead to larger voltages even when they are located inside the optical pupil. So, in general they degrade the balance in terms of the authority of the patches. As a result, a practical control configuration requires a strict filtering of the actuation modes involving the split-corners; therefore we loose most of the theoretical advantages of having a better actuation resolution near the corners.

5.2 Control with a Shack-Hartmann sensor

For the physical and theoretical aspects of the Shack-Hartmann (SH) sensor, the reader can refer to Chapter 2.3.1. It should be noted that we suppose a sensor without measurement noise.

The outputs of the SH optical sensor are local average slopes, gradients. The sensor is based on a grid of sensing points (corresponding to the centers of the lenses), and for each measurement point the slopes in x and y directions are provided. So, referring to Chapter 4.1, the Jacobian is divided in two parts: the first rows refer to the slopes in the x-direction, the following ones to the slopes in the y-direction. For the simulation, a grid of 25×25 measurement points is chosen (see Figure 5.9). This grid allows maintaining a number of measures bigger than the number of actuators (i.e. degrees of freedom) of each segment. We remind that for each

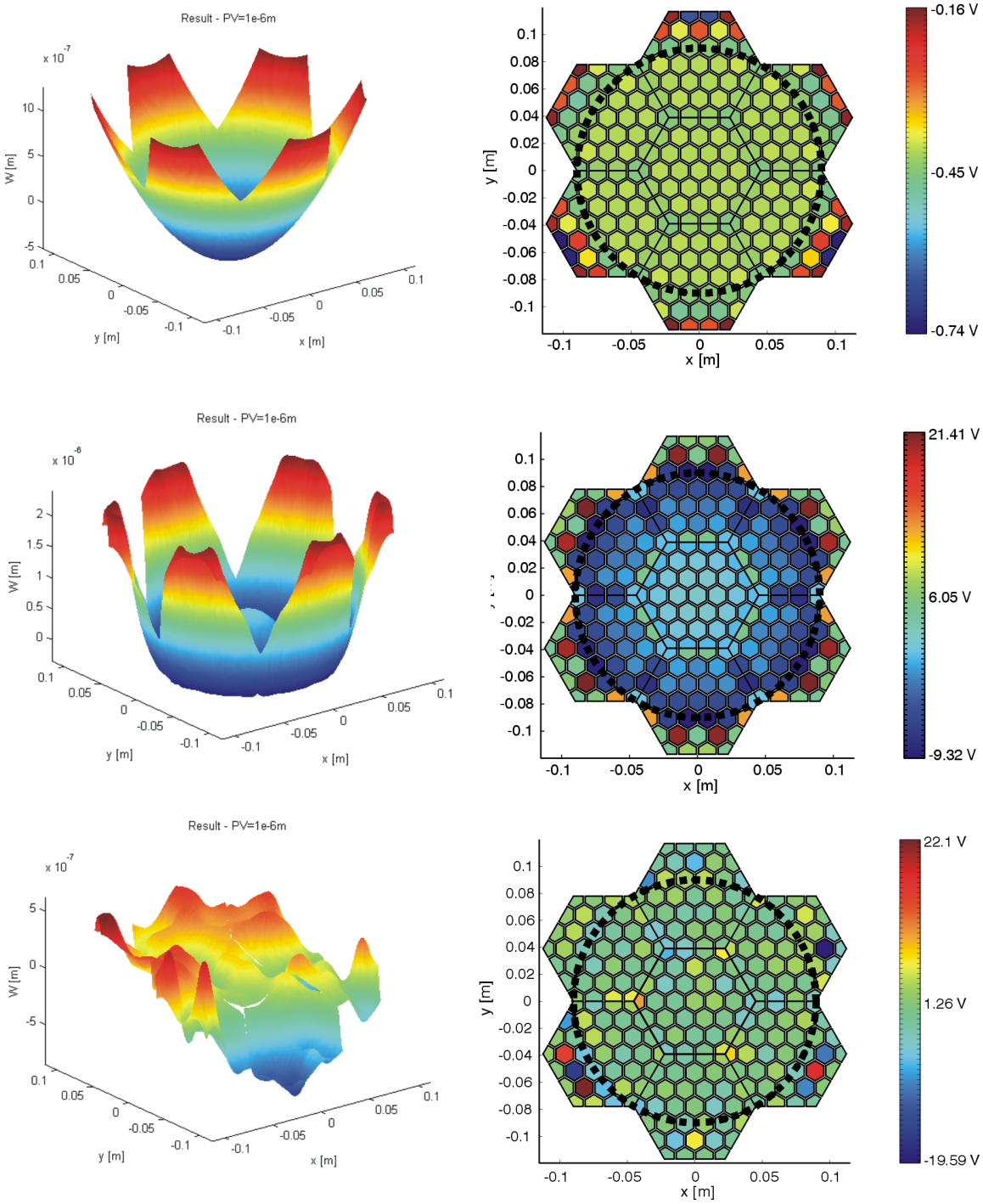

Figura 5.7: Results for Defocus, Spherical Aberration and turbulent screen. The threshold for the filtering is $s = 10^{-3}$.

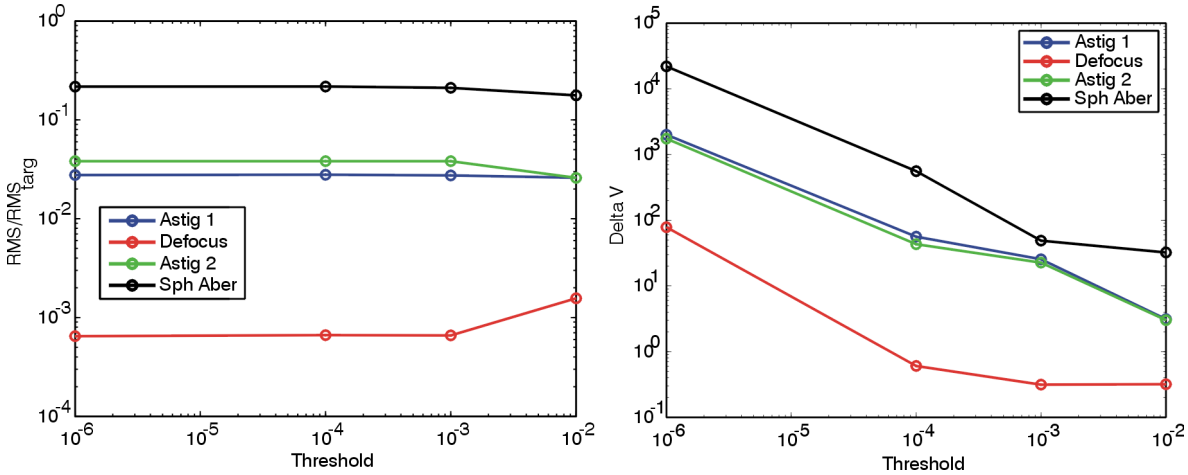

Figura 5.8: Results for a system with 19 segments for different Zernike modes as target surfaces.

sensing point of the SH, we have 2 measurements. Only the points of the grid that are inside the optical pupil are considered as active points. Sometimes also, the points inside the optical pupil that overlap between two segments, are not activated to be more coherent with the reality of the sensor[2].

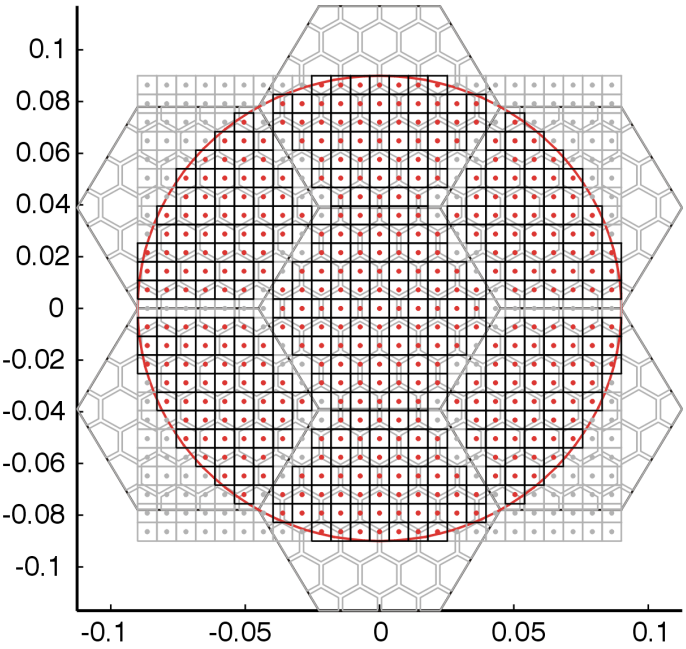

Figura 5.9: 7 segments configuration with a Shack-Hartmann grid of 25×25 points, with their corresponding (virtual) lenses. Only the red points are active measurement points for the sensor; the others (in grey) are not used in the algorithm.

[2]In general, such lenses would produce 2 spots on the detector (one per segment), making it difficult, if not impossible, to retrieve an accurate reconstruction if the slope and the orientation of the segments are not correlated.

5.2.1 Singular values

The filtering of the singular values is also necessary to achieve good results in the case of the SH. The eigenvalue distributions for segments 1 and 2 are depicted in Figure 5.10. Similarly to the case with the displacement sensor, the central segment has a better distribution of the eigenvalues. The first, evident difference with respect to the previous case is that the SH sensor, by nature, does not sense the piston term, and this fact implies the presence of a singular value equal to 0 for this piston term. It happens for all the segments. In order to avoid problems in the pseudo-inverse of the matrix due to this bad-conditioning, this singular value must be always cut off by the filter.

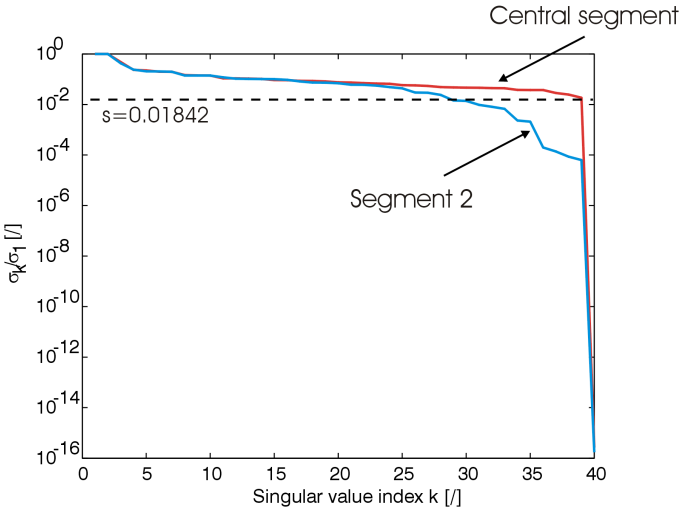

Figura 5.10: The normalized singular value distributions for segments 1 and 2, using a SH sensor with a grid of 25×25 points shown in Figure 5.9.

The second difference respect to the displacement sensor is based on the grid chosen for the analysis. In fact, except for the inevitable presence of the null singular value, it is possible to demonstrate numerically that the denser the grid of the SH, the better the conditioning of the other singular values.

It appears from several test that the tuning of the filter for the Shack-Hartmann sensor is really strict. It is not robust with respect to little changes in the threshold (i.e. a smaller decrease of s induces a noticeable increase of the voltage range). The best results for RMS and voltage range are reached using a cutting level just below the first non-zero singular value of the central segment: this choice allows to preserve all the singular values of the central segment (except the one associated with piston). In Figure 5.10 the dotted line is an example of filtering using this strategy.
In Figure 5.11, the trend for the target shape and the voltage map changing the filter level is presented. The target is an Astigmatism, the same target shape of the example analyzed for the displacement control. The results in the middle of the picture refer to a filtering level of $1.842e^{-2}$, the value just below the first non-zero value of the central segment. It is interesting to notice that in the results at the bottom, with a higher level of filtering (10^{-1}), the segments lose a high number of singular value (i.e. actuation degrees of freedom), and the final result becomes closer to a system with only rigid motion allowed (the morphing capacity of the

segment is reduced). Figure 5.12 synthesizes the performances of the system as a function of the threshold of the filter.

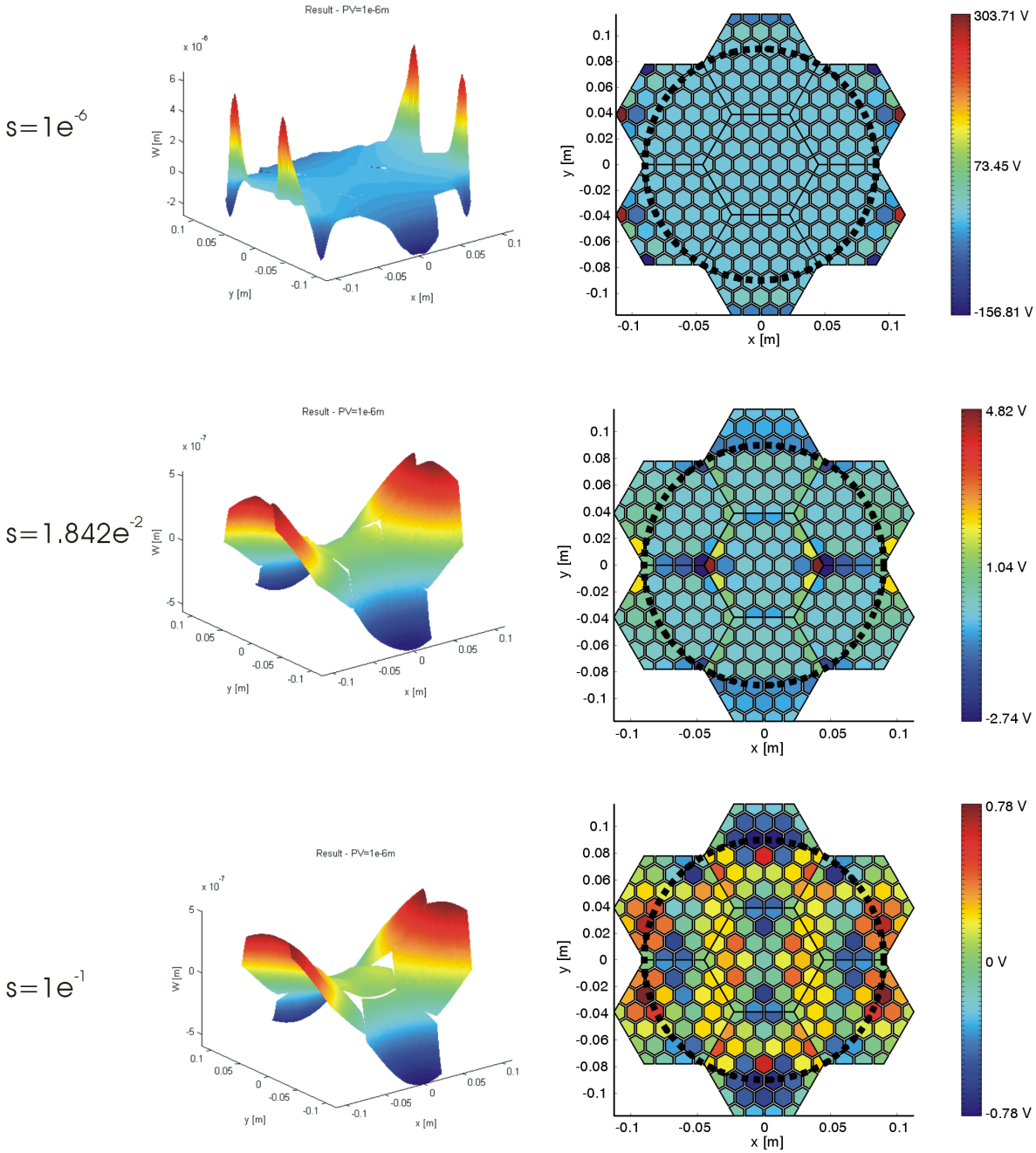

Figura 5.11: Evolution of the shape and of the voltage maps using a Shack-Hartmann sensor, by changing the threshold. The target shape is an Astigmatism.

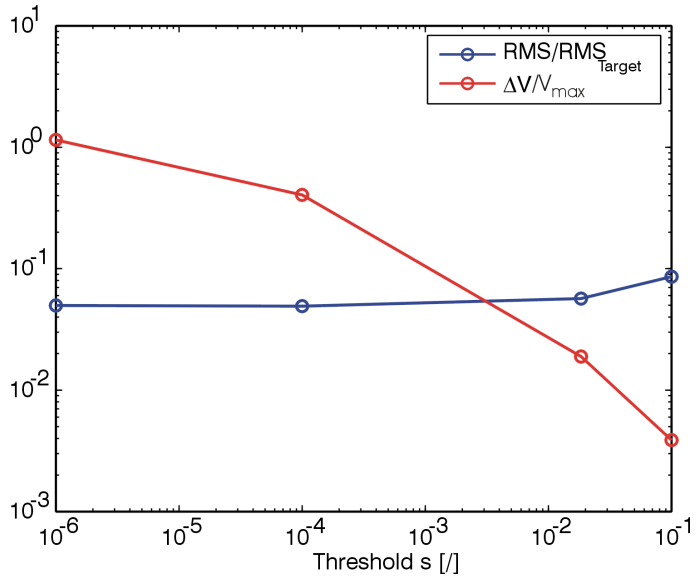

Figura 5.12: Evolution of the normalized RMS and voltage range as a function of the threshold for the filtering, s. Here $V_{max} = 400V$.

5.2.2 Results

Figure 5.13 shows the results for Defocus, Spherical Aberration and a turbulent screen, using the reference control strategy, based on a filtering that preserves strictly the singular values of the central segment. It has been demonstrated numerically that the filtering strategy is valid also for configurations with more segments. The results also proved sensitive to deviations from this strict preservation of the singular values of the central segment. These results have been omitted here.

5.2.3 Note: coupled SH

Up to now, we have used a square grid of measurement points (lenses) for the SH sensor. Other geometries are also possible. In general, the choice of the grid can affect the results if the points are not well disposed in space, resulting for example in a kind of spatial aliasing[3]. We illustrate this with the geometry displayed in Figure 5.14: we consider hexagonal lenses in a pattern matching that of the patches; i.e., there are as many measurement points as patches. This kind of honeycomb geometry is commonly available from micro-lenses manufacturers.
This particular configuration introduces one effect in the reconstructed surface (that happens also with square grid in particular cases with an insufficient number of measurement points, so for spatial aliasing): some bumps appear in surface. This comes from the slopes of the IF itself: by nature, the patches create a local curvature inside their footprint, and a constant slope elsewhere (see Appendix C). As the lenses are centered over the patches and sense average slopes in x and y, each IF is seen as a null signal by its corresponding lens, no matter

[3]With *spatial aliasing* we mean a wrong sampling of the surface due to a disposition and quantity of points not sufficient to appreciate the real shape of the surface. Similarly to what happens with the (temporal) sampling of signals, if we do not use a sufficient number of sampling points, the resulting surface can be totally different from the original one (for signals in time, one can use the Shannon theorem to establish a suitable sampling frequency).

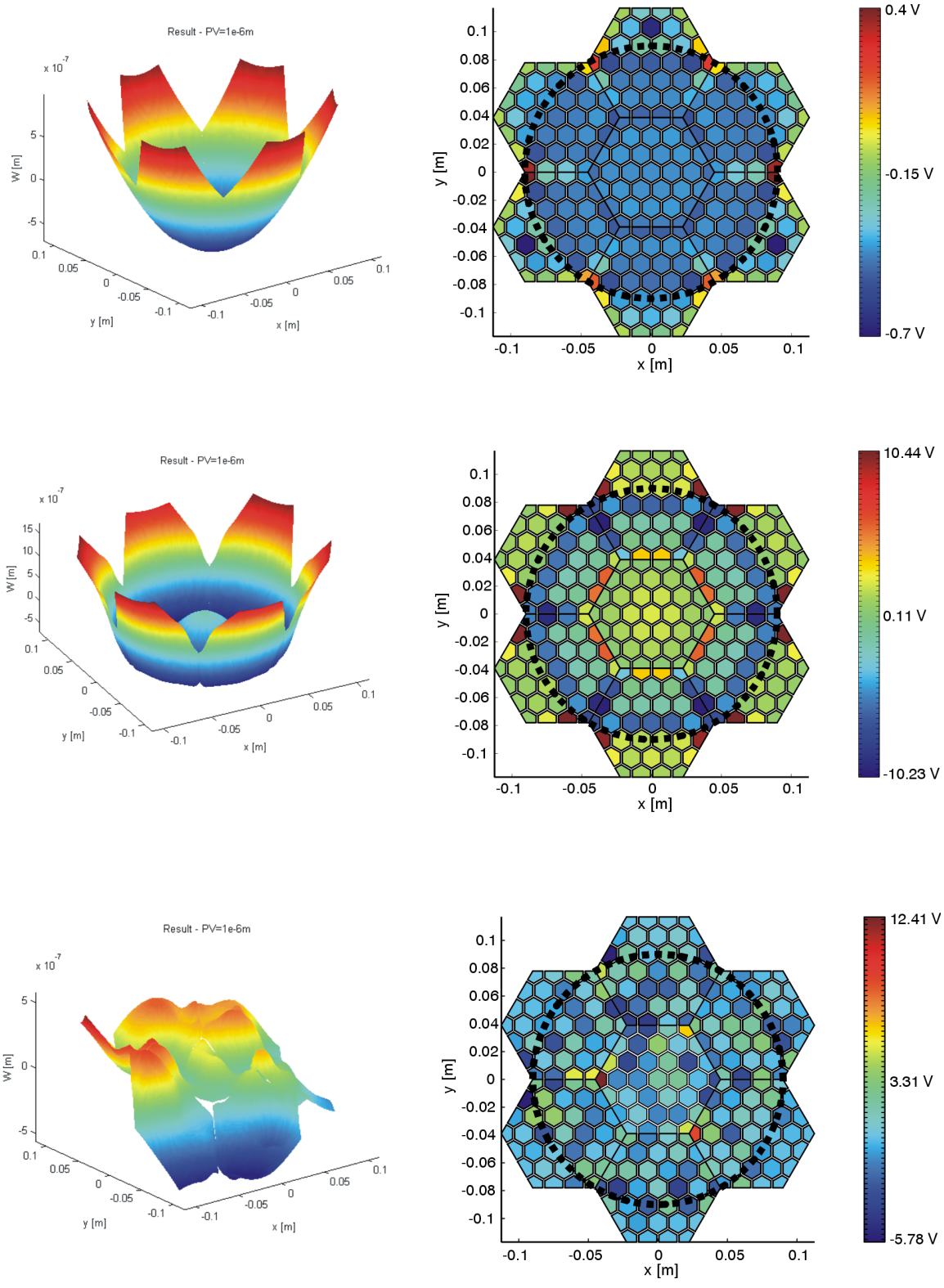

Figura 5.13: From top to bottom: Defocus, Spherical Aberration and turbulent screen. A SH sensor with 25×25 points is used. The threshold for the filter is 0.01842.

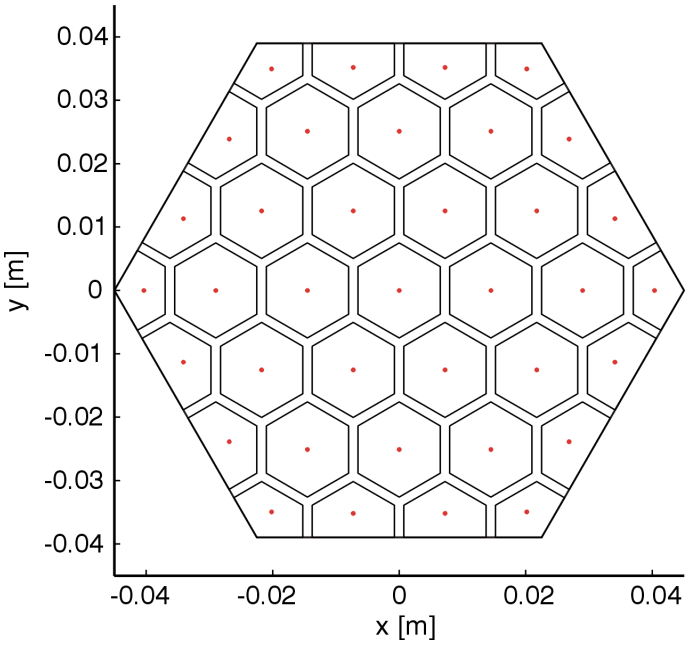

Figura 5.14: Configuration with an hexagonal segment with 37 piezoelectric patches and the SH sensor measurements points positioned on the center of each patch.

its actual amplitude. This induces the control algorithm to often converge to results such as those illustrated in Figure 5.15. The filtering does little to improve this fact. Before the testing of this configuration, it was expected to be well-conditioned owing to this diagonal of zeros (or near-zero values) coupled to non-zero off-diagonal terms; however, deep numerical investigation proved the opposite: this configuration exhibits poor results in general and should be rejected in favor of a square grid of lenses with a sufficient number of lenses.

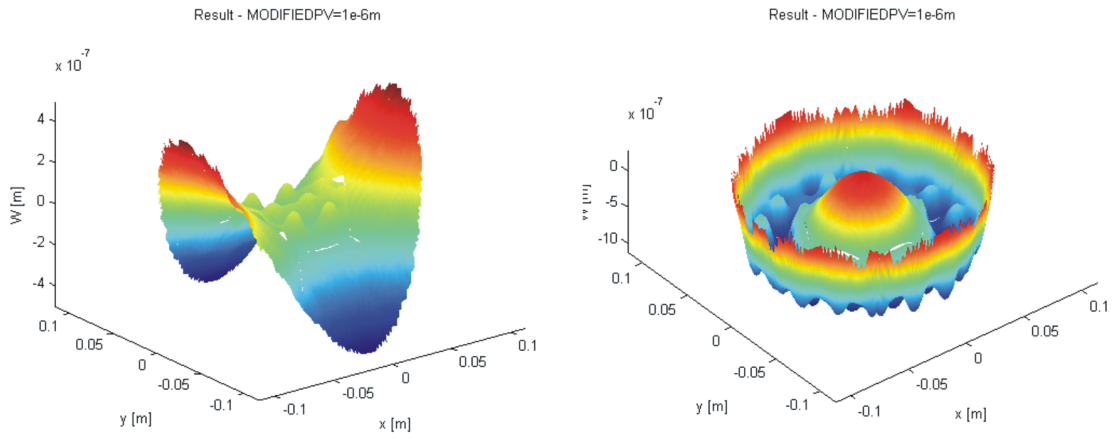

Figura 5.15: Two examples of result surfaces (the corresponding targets are Astigmatism on the left and Spherical Aberration on the right) with s SH grid matching the geometry of the patches. Undesirable bumps can be observed easily, resulting from the particular relation between the sensors and the actuators in this case.

5.3 Conclusions

In this chapter, we have highlighted and isolated the influence of the actuator network from that of the sensor on the control problem. The displacement sensor is only an ideal sensor that is not possible to use in applications such as adaptive optics. Its results are theoretical, and can be used as a point of comparison for other sensors (a best case), as this sensor allows quantifying the morphing capability of the actuation network. The SH sensor is, on the contrary, a widespread optical sensor; here we consider ideal SH sensors because parameters such as measurement noise are omitted in the analysis. However, the results still give an accurate account for the influence of the main characteristics of such sensors (resolution, quantity sensed,...) on the control performances.

Each sensor induces differences in the Jacobian matrix, particularly in terms of its conditioning. For example, with the SH sensor, the singular value associated to piston is always equal to zero because of the physical principle of the sensor, and it must be filtered out to avoid numerical problems when computing the pseudo-inverse of the Jacobian.

Furthermore, ensuring a good compromise between performances (morphing, phasing) and feasibility (limited voltage ranges, reasonable demands on the actuators properties,...) requires addressing the conditioning issues of the Jacobian. Small singular values can either ensue from the very limits of the sensor (e.g. SH cannot sense piston at all, edge sensors cannot sense global piston and tip/tilt,...), from the presence of actuators with a low authority or with quasi-identical influence functions (from the point of view of the sensor at least). These problems appear in our system because of the actuators located outside the optical pupil, and those on the edges/corners of the segments (thus 2 to 3 times smaller than the others), irrespective of the sensor type.

This problem is addressed here by filtering the problematic singular values. We have demonstrated numerically that a simple rule can be used to define the threshold of the filtering, that proved valid for both sensors: the threshold for the filtering is fixed so as to preserve the singular values of the segments located fully inside the optical pupil, and to remove all the singular values below this threshold for the segments partially outside the pupil. This proved a good compromise as the negative influence of the most problematic actuators is mitigated while the full morphing capability of the segments inside the pupil is preserved. We have also shown that, in general, the conditioning of the matrix and the robustness of the filtering rule (with respect to an underestimate of the threshold value) improve as the density of measurement points increases.

Capitolo 6

Parametric Study

In Chapter 5, the system was studied in terms of geometry, morphing capability and control strategy. We are now interested in the evolution of the performances if we change the number of segments and of actuators per segment, keeping constant the optical pupil diameter, the number of degrees of freedom of the system and the target surface (a turbulent screen, see Figure 6.1). The system will evolve from a purely deformable configuration (composed of a single segment) to a segmented mirror with rigid segments only (i.e. with only the 3 active feet as rigid-body actuators).

The diameter of the optical pupil is close to be $D_{ap} = 0.32m$. Regarding the grid of the Shack Hartmann sensor, an initial configuration with 40×40 lenses is chosen (an example for the reference configuration is given in Figure 6.2). In order to keep the number of degrees of freedom constant, increasing the number of segments requires to decrease both their size (to keep D_{ap} a constant) and the number of actuators per segment to keep the total number of degrees of freedom approximately constant. Below a certain segment size this 40×40 SH grid causes some segments to be covered by a number of lenses that becomes too small (this is especially important in cases when it leads to segments with more actuators then sensing points, as it changes the effect of the control, see Chapter 4.1). In these cases, a grid with 60×60 lenses will be used. We shall recall that each Shack-Hartmann point corresponds to two measurements, both in the x- and y-direction.

A turbulent screen is chosen as the target as it is the most physically relevant target to assess the performances for real adaptive optics applications.

We also need to consider other parameters to evaluate each configuration, such as the natural frequency of the mirror and the practical case of implementation. These are important factors; they play an important role in the characterization of the system.

From the point of view of co-phasing, the approach using the Zernike Phase Sensor is here applied for its feasibility. We consider 8 measure points per edge (see Chapter 4.2). The results have been calculated both with only one average area per side and with 2 areas, and they are affected only in a negligible way by this choice. Therefore, the results shown below refer only to one average area per edge.

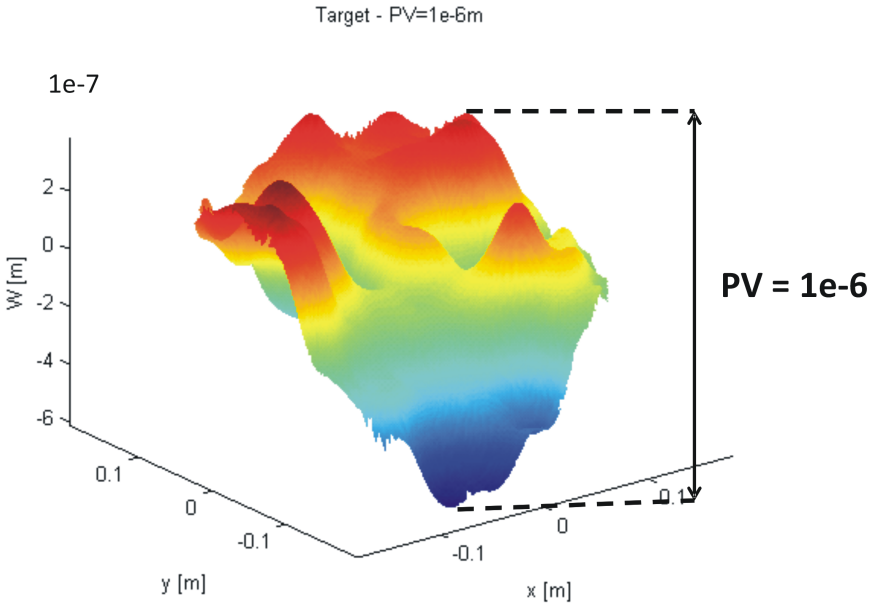

Figura 6.1: The turbulent screen used as target surface common to all the configurations, with a peak to valley amplitude of $1\mu m$. The RMS of the surface is $RMS_T = 1.8630e-7$.

6.1 Reference configuration

The reference configuration for this study is shown in Figure 6.2: it consists of 19 segments with 37 piezoelectric actuators and 3 rigid-body actuators per segment. This implies a total number of degrees of freedom equal to 760. As discussed in Chapter 5, the Shack-Hartmann sensor induces a singular value close to zero in the Jacobian, associated to the piston term. We suppose that this value is always cut off by the filtering process.

Figure 6.3 shows the evolution of the results for different values of the threshold for the filtering, s. Table 6.1 summarizes the numerical values associated to these 3 cutting levels. It is important to notice (and it is valid in general for all the configurations) that the best results in terms of RMS error and voltage range are achieved when the filtering of the eigenvalues is at the level of the last significant singular value of the central segment that is when all the singular values of the central segment are preserved strictly and the singular values of the outer segments with a normalized value below the threshold are cut off.

Threshold	RMS	RMS/RMS_T	$\Delta V[V]$
10^{-6}	$6.041e-9$	0.0313	$1.595e4$
10^{-3}	$5.914e-9$	0.0306	213.90
$6.67 \cdot 10^{-3}$	$5.39e-9$	0.0279	18.63

Tabella 6.1: Performance of the system changing the threshold value for the filtering. The RMS of the target is $RMS_T = 1.8630e-7$.

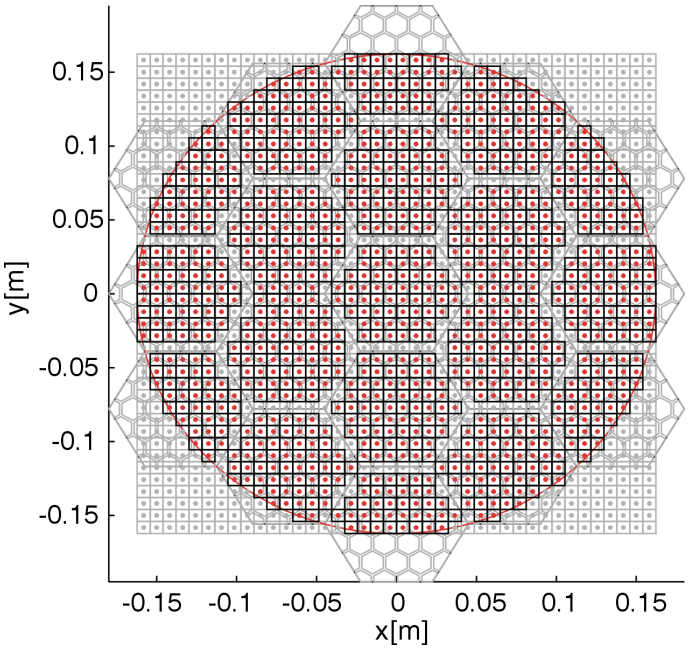

Figura 6.2: Geometry of the reference configuration. The dots are the measurement points (lenses) of the Shack-Hartmann sensor. Only the red ones are active measurement points: they are inside the optical pupil and the lenses overlapping the edges between two segments are deactivated (see Chapter 5.2).

The effect on the performances is considerable. In particular, the voltage range decreases from thousand of Volts to a few tens of Volts. Looking at the voltage maps, we can see in the first two cases how the peak values are always in the external segments, outside the optical pupil. Thanks to the filtering effect this problem disappears gradually, and in the last configuration one can appreciate a much better and more balanced distribution of the voltages inside the optical pupil, that was masked by the large peak values.

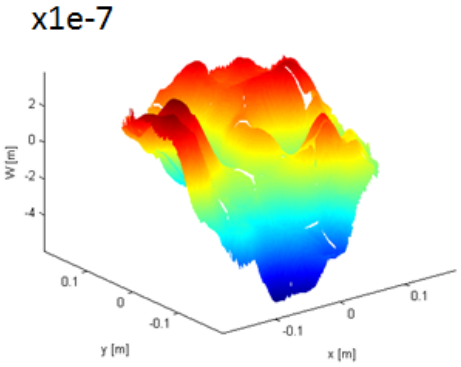

(a) *Result*, $s = 10^{-6}$.

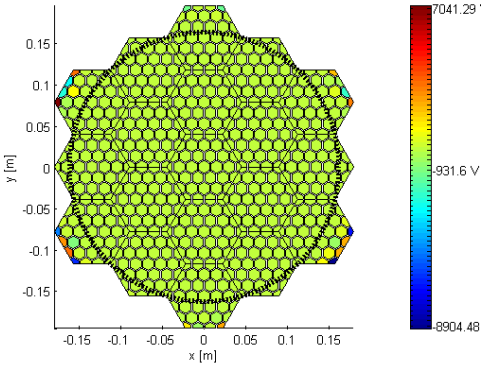

(b) *Voltages map*, $s = 10^{-6}$.

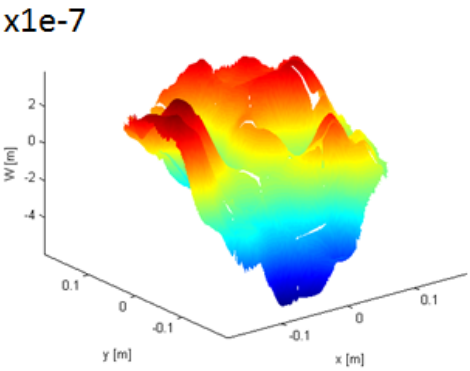

(c) *Result*, $s = 10^{-3}$.

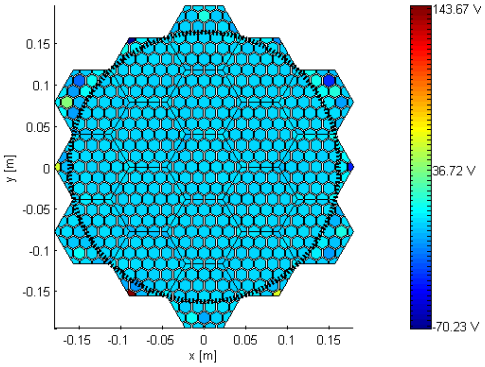

(d) *Voltages map*, $s = 10^{-3}$.

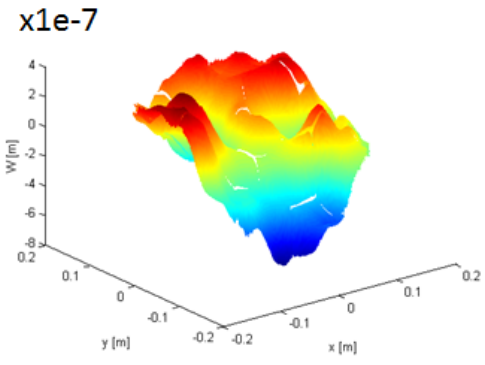

(e) *Result*, $s = 0.00667$.

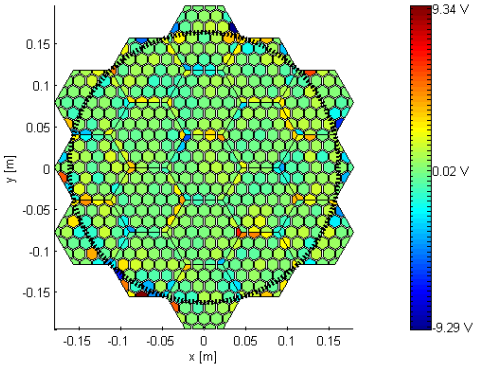

(f) *Voltages map*, $s = 0.00667$.

Figura 6.3: Influence of the filtering on the resulting shape and on the corresponding voltages.

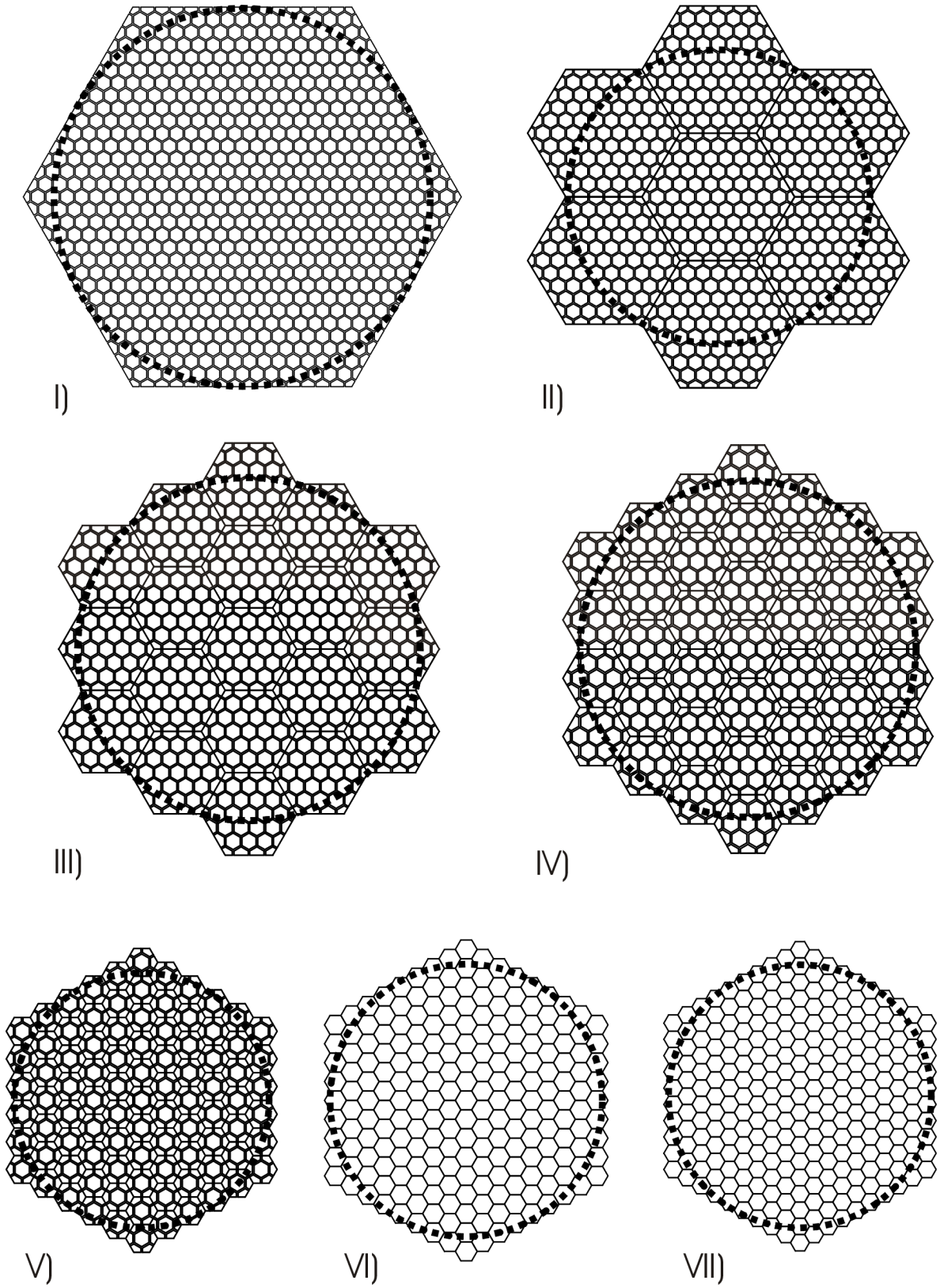

Figura 6.4: The configurations of the system. The numbering follows Table 6.2.

6.2 Other configurations

In Table 6.2, seven different configurations are summarized. They cover several cases from a segment with 721 patches to a highly segmented mirror, where the segments have no piezoelectric patches but only 3 rigid-body actuators each.

Config.	N_s	n_a	N_{tot}	$D_s[m]$
I	1	721	724	$375e-3$
II	7	91	658	$162e-3$
III	19	37	760	$90e-3$
IV	37	19	814	$65e-3$
V	91	7	910	$41e-3$
VI	217	1	868	$26e-3$
VII	271	0	813	$23e-3$

Tabella 6.2: Main characteristics of the configurations studied here. N_s is the number of segments, n_a is the number of patches per segment, N_{tot} is the total number of actuators and D_s is the diameter of the segment. Note that in the column with the number of patches the 3 rigid-body actuators are excluded from the total. Configuration IV is the reference case described in section 6.1.

In Figure 6.4, at the end of this chapter, it is possible to see the pictures correspondent to the configurations in Table 6.2.
For configurations I to IV, a Shack-Hartmann with 40×40 lenses per edge is sufficient to correctly sense all the segments. For the other configurations, the grid is switched to 60×60 lenses, to avoid a substantial decay of the performances of the system as mentioned above. For each configuration in general, we use the filtering strategy described in the preceding sections (the only exceptions are described below). As the geometry of the system changes, the value of s changes too, but the idea remains the same. Three particular configurations need some remarks.

- **Configuration I**: It is purely deformable. Since there is only one segment, the strategy for the filtering of the singular values described above is not applicable. However, there is still a need for filtering, that comes from the presence of actuators outside the pupil (see Figure 6.4), in particular around the corners (i.e. small ones)that induce the same problems as in the configurations with more segments. Although the particular shape of this mirror would not be implemented in practice, it is representative od deformable mirrors with a high density of actuators (see e.g. $M4$ for the E-ELT, $M3$ for TMT or a prototype developed at TU Delft [11]). However it can be shown [30] that a segmented architecture has several potential advantages in terms of cost, ease of implementation, maintenance, risk,....

- **Configuration VI**: In this configuration, there are 217 segments and a single piezoelectric patch per segment. In this case the approach for the filtering illustrated above is not applied. In fact, during the pseudo-inverse process there are only 4 singular values (Figure 6.6): 3 are the rigid-body modes (i.e. piston, tip and tilt)and the residual one is associated to defocus. As already mentioned, the piston term has a singular value close

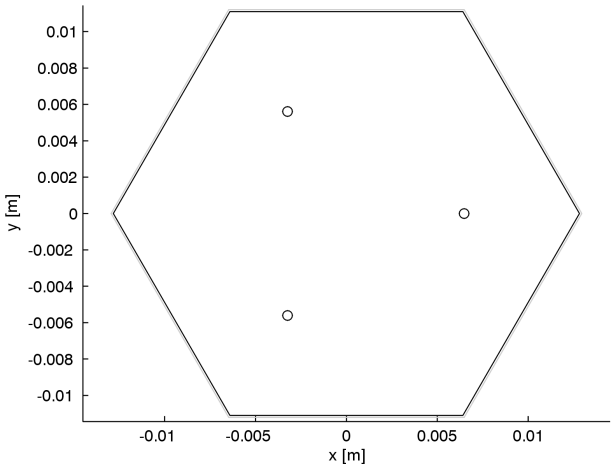

Figura 6.5: A segment with a single patch glued on the back. The dimensions of the patch are equal to those of the segment. The three little circles represent the locations of the active feet.

to zero which is always cut off. In this particular case, we do not cut any other singular value in order not to lose the degree of freedom that differentiate this configuration from number VII, nor the singular values associated to tip-tilt, which would decrease significantly the performances of this configuration. Finally, one should notice that, by nature, the defocus IF is well sensed, provided that there are enough lenses to sense it properly. In Figure 6.6, we see that it is clearly the case all the curves are very close to each other.

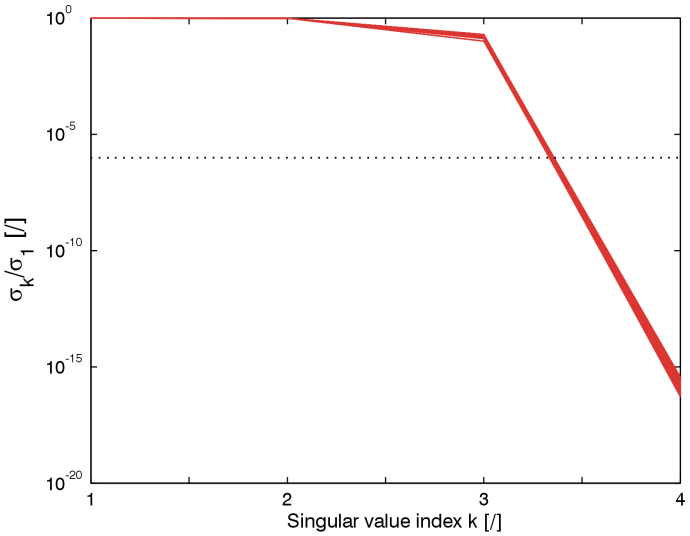

Figura 6.6: Configuration VI has only 4 singular values per segment, the distributions are similar for all the segments, indicating a good conditioning. The threshold of filter is set to 10^{-6}: only the piston term is cut off by singular values filtering. The first two singular values, with the largest values, are related to tip-tilt, the third one is associated to defocus.

- **Configuration VII**: It is a purely rigid configuration, so there are no patches on the back of the segments: the three active feet provide the rigid motions of the segments (basically the first 3 Zernike polynomials: piston, tip and tilt). The piston term is always cut off by the filter. Here, like in configuration VI, all the other modes are preserved to avoid performances decay. Examples of rigid segmented mirrors (with bigger dimensions of each segment) are present both in literature, see [34], and in real applications like the fast-steering secondary mirror (FSM) of the Giant Magellan Telescope (see Chapter 1).

6.3 Natural frequencies

An important parameter for the system is the natural frequency of the mirror. In fact it has important consequences on the bandwidth of the control and resistance of the system to external excitations. Typical requirements for space applications involve frequency $f_1 > 150Hz$ to resist launch vibrations. For ground-based telescopes, the frequency must be bigger than the cut off frequency required for adaptive optics, which means $f >\sim 250Hz$.

It is possible to maximize the resonance frequency by a good choice of the feet position (i.e. by acting on the boundary conditions of the system). This is illustrated in a parametric study on the position of the feet in a simplified numerical model: an hexagonal segment with a continuous layer of PZT (it's a conservative approach with respect to f_1). A diagram of the model is depicted in Figure 6.7. The results following this approach are presented in Figure

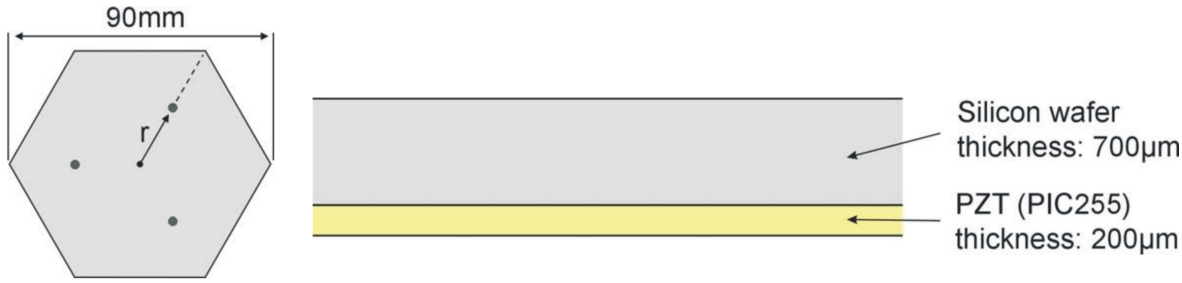

Figura 6.7: The simplified model used for the parametric study on resonance frequencies.

6.8. The optimum in terms of the first natural frequency is when the feet position is in the vicinity of $r/R = 0.4$, where R is the radius of the circumscribed circle. So in what follows, this guideline for the feet position is respected during the simulations[1]. The frequencies calculated with the FE model, for the seven configurations, are reported in Table 6.3.
To validate these results, we compare them to those given by an analytic formula for f_1 found in literature [5]:

$$f = \lambda^2 \frac{1}{2\pi a^2} \left[\frac{Eh^3}{12\gamma(1-\nu^2)} \right]^{1/2} \tag{6.1}$$

[1]Practically speaking there are also other technological requirements. In particular a larger distance between the feet shall improve the stability with respect to launch vibrations (for space telescopes). Moreover the feet should be slightly de-centered on the patch to leave enough space for the electrical connector of the patch. For mechanical robustness, the feet must be glued so as to avoid an overlap between 2 or more patches. In the system described in Chapter 3, feet are located in the interval $r/R = [0.5 - 0.6]$, where the decrease for the first natural frequency is not significant, leading to $f_1 > 500Hz$ for the case depicted in Figure 6.7.

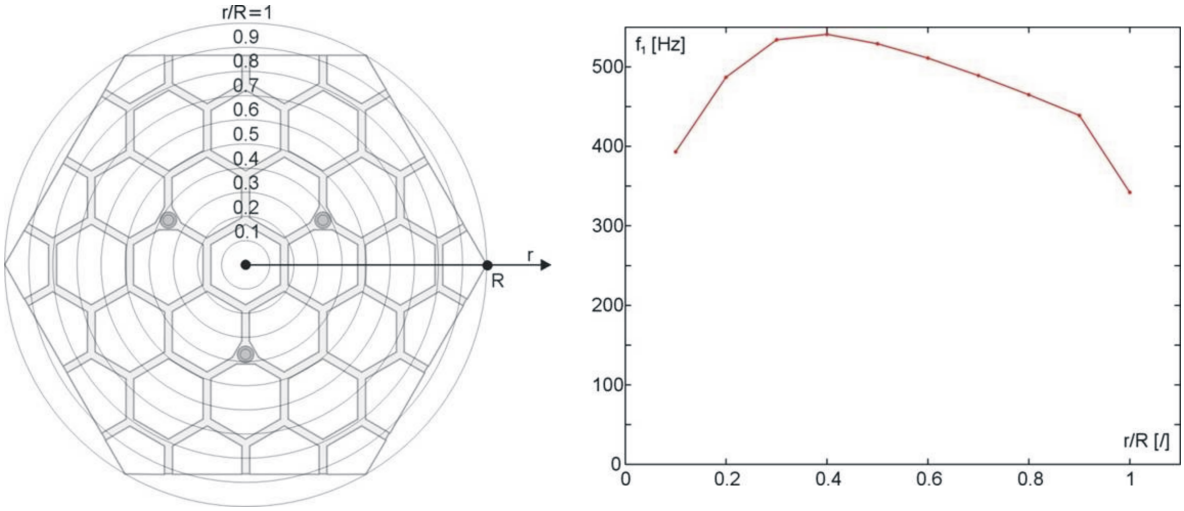

Figura 6.8: Results of the study on natural frequencies changing the feet position. In the graph on the right one can notice that the trend for natural frequency has a maximum in $r/R = 0.4$

Config.	I	II	III	IV	V	VI	VII
Freq [Hz]	32.2	172.1	558.6	1063.6	2701.5	6604.9	9315.2

Tabella 6.3: Values of frequencies for the seven configurations here studied.

where a is the length of a side of the hexagon $[m]$, h is the thickness of the plate $[m]$, E is the Young's modulus $[Pa]$, ν is the Poisson ratio, $\gamma = h\rho$ where ρ is the density of material expressed in $[kg/m^3]$ and λ^2 is a coefficient function of the boundary conditions. The frequencies from the FE and from the analytical model are be compared in Figure 6.9. The comparison shows a good agreement between the 2 models both in terms of trends and order of magnitude. The differences mainly comes from the error induced by considering the same λ^2 for all the configurations, while the position of the feet actually changes a little from a configuration to another. The other significant contribution to the error comes from the fact that Equation 6.1 requires homogenized values of the material properties (E, ρ, ν) because the segment is actually a composite structure, and these quantities actually change from a segment to another and are not homogeneous for configurations I to IV; hence we introduced an error in considering the same characteristics for all the configurations.

6.4 Results

The results of the comparison of the performance of the various configurations are shown in Figure 6.10. The RMS values are normalized with respect to the RMS value of the target surface, $RMS_T = 1.9321e-7$). Also, the values for the voltage ranges are normalized to the maximum positive voltage applicable to the piezoelectric actuators, equal to 400 V. For the purely rigid configuration (VII) the voltage range is not considered, because there are no patches. The natural frequencies plotted are those obtained by the FE model, shown in a semi-logarithmic graph. The RMS error increases as the number of segments increases,

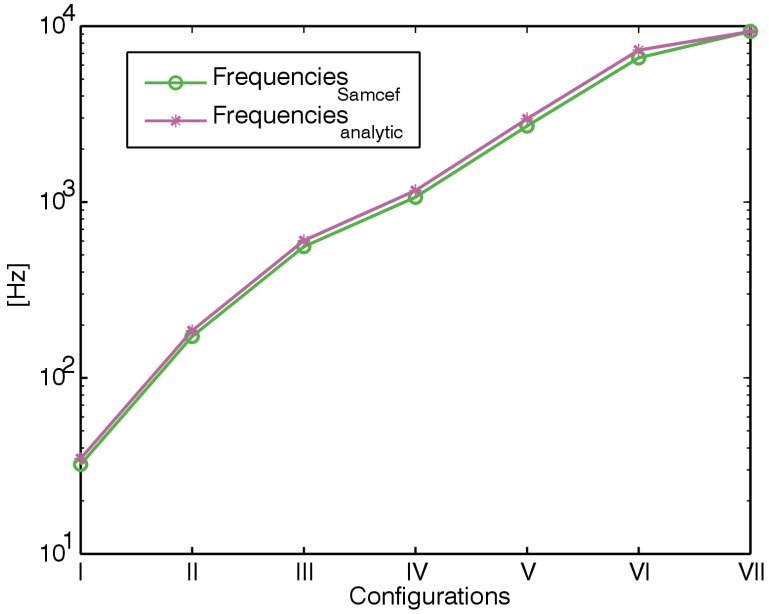

Figura 6.9: Comparison of the results from the FE model and from Equation 6.1 for the different configurations. The trends and orders of magnitude are comparable.

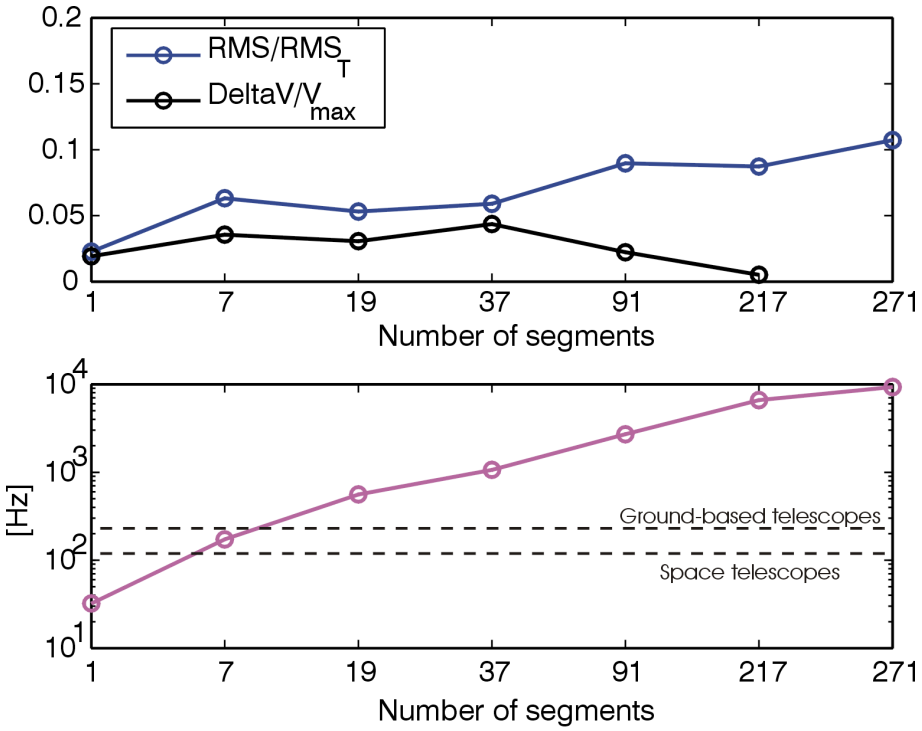

Figura 6.10: Comparison of the performances of the 7 configurations. Top: normalized values of the RMS error and voltage ranges. Bottom: trend of the natural frequencies.

while the voltage range decreases. For the configurations with more then 37 segments, the RMS error reaches 10% of the RMS_T: it is possible to obtain lower values (in general for a slightly larger ΔV) by increasing the number of sensing points of the Shack-Hartmann sensor (for these configurations the grid is already composed of 60 x 60 lenses). The limitations are given by the effective Shack-Hartmann grid available and by the theoretical background of the pseudo-inverse algorithm (see Chapter 4). The first configuration (purely deformable), appears the worse in term of resonance frequencies; configuration II could meet the specifications of ground-based applications, but may be too low for space applications. Configurations III to VII would all meet both requirements[2].

6.5 The Strehl ratio

To deepen the comparison, we consider here the performances in terms of the Strehl ratio. Although based on the RMS error, its physical meaning is less obvious, particularly from a mechanical point of view, but it is widely used to characterize the performances of optical system and subsystems.

Because of the wave nature of light, even a perfect (unaberrated) optical system will not image a point source as a true point, but rather as a bright core surrounded by a halo. This spreading of the light energy is called *diffraction* (see Chapter 2). An optical system is said to be *diffraction-limited* when the aberrations are sufficiently small so that the size of the image point is only limited by diffraction. It is a lower physical boundary to the size of the image spot that a perfect imaging system can produce [1].
The image of a point object formed by an imaging system is called its *Point Spread Function* (PSF): its takes into account both diffraction and aberrations. The image formation is a convolution of each point of the object by the PSF: that is the narrower the PSF, the sharper the image. The PSF of a diffraction-limited imaging system with an unobstructed circular aperture is called the *Airy disk* (Figure 6.11). It consists in a bright core surrounded by concentric rings. 84% of the total light energy of the image surface is contained in the central spot. Its diameter is proportional to λ, the wavelength of light, and to a design parameter called *f-number* $f/\#$, which can be defined for parabolic mirrors as:

$$f/\# = \frac{EFL}{EPD} = \frac{F}{D} \tag{6.2}$$

where the Effective Focal Length (EFL) is defined as the distance over which collimated rays are brought to focus, the Effective Pupil Diameter (EPD) is the diameter of the element that effectively limits the extent of the incoming light flux, F is the focal length and D is the diameter of the mirror[3].

The ratio between the peak intensity of a telescope undergoing aberrations to that of the same telescope working as diffraction-limited is called the *Strehl ratio*, S. Equation 6.3 gives an approximation of S in terms of the RMS output wavefront error (denoted by σ_1 and expressed in meters, for a target surface normalized to $1\mu m$ PV).

$$S = \frac{PSF(peak)_{aberrated}}{PSF(peak)_{unaberrated}} \simeq e^{-(2\,\frac{2\pi\sigma_1}{\lambda}\,\alpha)^2} \tag{6.3}$$

[2]For the last two configurations, applications for MEMS system exist, but the technology behind these systems is different from the one here considered and will not herein treated. For one example see [13].

[3]A more complete discussion can be found in [32]

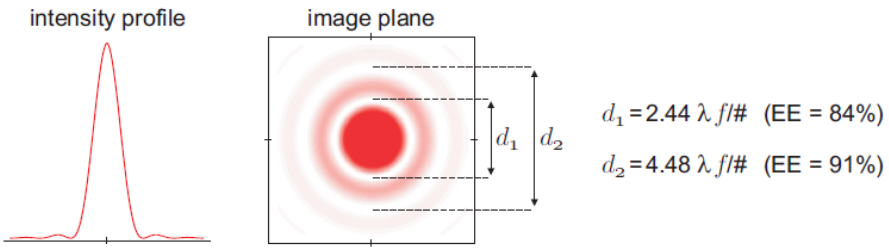

Figura 6.11: Airy disk, diffraction pattern produced by a perfect imaging system with a circular pupil. EE refers to the percentage of encircled energy [1].

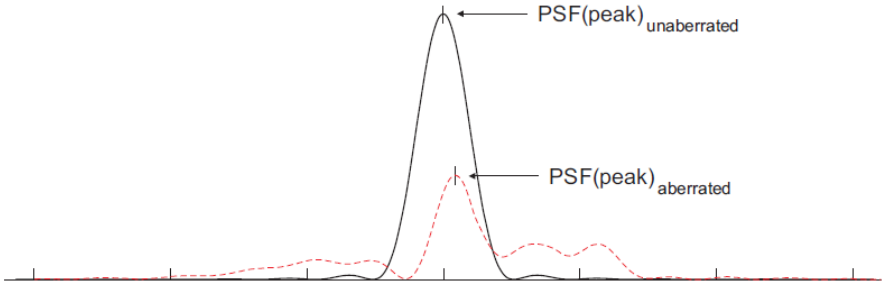

Figura 6.12: Comparison of the PSF of a diffraction-limited (unaberrated) telescope with that of the same telescope undergoing aberrations. The lateral shift is due to tilt [1].

The factor 2 in the exponent transforms the RMS error of the mirror surface to that of the reflected wavefront. The α is a multiplier factor to scale the RMS error to a target surface with an arbitrary amplitude. For $S \geq 0.8$ the telescope is conventionally defined as diffraction-limited, corresponding to a wavefront RMS error less than $\lambda/14$. A value of $S \geq 0.5$ is currently considered good in many applications (see for example [20]). It should be emphasized that this criterion is wavelength-dependent and it gives no information on the shape of the halo. For this study, to be more coherent with the reality, we have scaled the results to realistic values of the target surface for the VLT. In particular an amplitude of $2.74\mu m$ PV for the turbulent screen is chosen (see [30]). We used two wavelengths: at $0.5\mu m$ (*yellow light*) and $1\mu m$. The range of visible light is between these two values of λ (except for the lengths between $0.7\mu m$ and $1\mu m$ that are part of the near-infrared radiation). Figure 6.13 depicts the Strehl ratio as a function of the configuration. Only the purely deformable configuration has a Strehl ratio above 0.8, that is a perfect shape (with $RMS_{error} < \lambda/14$), in both cases. The Strehl number for $\lambda = 1\mu m$ is always above the 0.5 value, and the first 4 configurations can even be considered diffraction-limited. For the case with $\lambda = 0.5\mu m$, the last 3 configurations are below the limit of 0.5 of a good mirror quality. In general, we can say that the first 4 configurations analyzed provide a satisfactory optical quality for the wavefront.

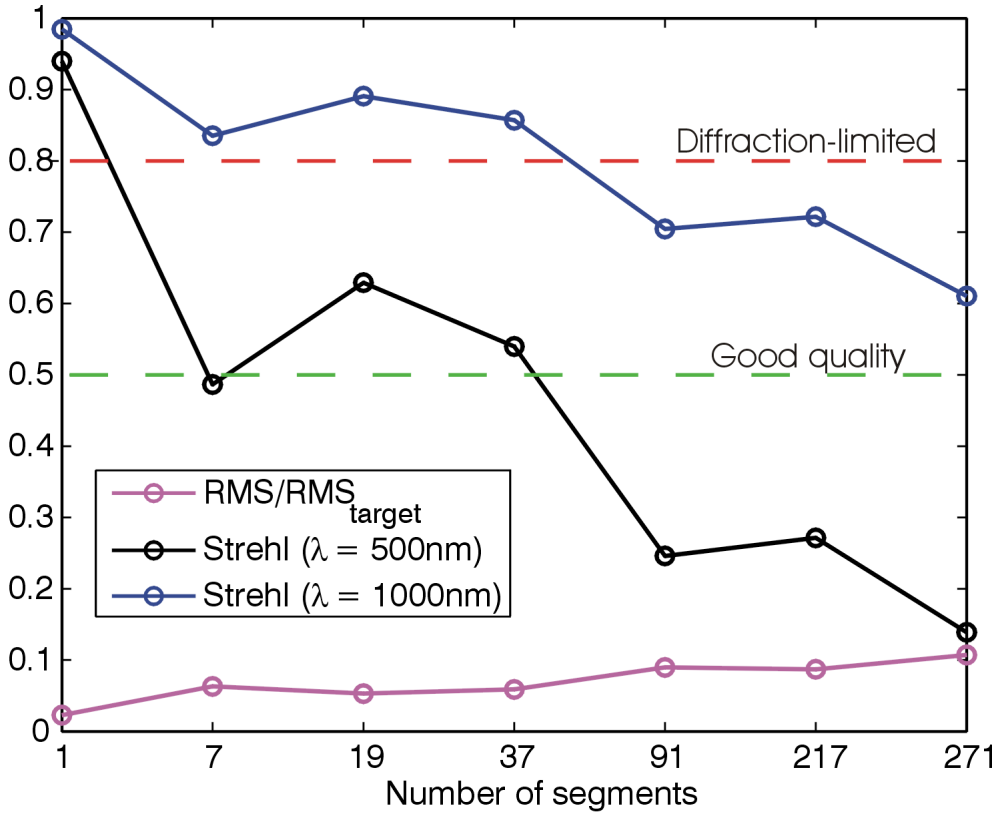

Figura 6.13: Plot of the trend of Strehl ratio for an increasing number of segments and constant diameter of the optical pupil. The curve for normalized RMS error is also provided. Red dotted line is the threshold for mirrors considered diffraction limited, the green one is the lower acceptable limit for the Strehl number.

Appendice A

Zernike Polynomials

They were introduced in 1934 by F. Zernike who deduced them from Jacobi polynomials and slightly modified them for the applications in optics. They are very often used to describe optical aberrations, because they are mathematically well defined and the low order terms are related to the classical aberrations, like astigmatism, coma and spherical aberration [9]. Moreover they can be used to model the effect of atmospheric turbulence on a beam of light, using the Kolmogorov approach e.g. .

Zernike polynomials are a set of polynomials defined on a unit circle. It is useful to use polar coordinates so that the polynomials are a product of angular functions and radial polynomials. The angular functions are the basis functions for the two-dimensional rotation group, and the radial polynomials are developed from the Jacobi polynomials. In [25] these polynomials are normalized in a suitable way for application to Kolmogorov turbulence. In this normalization each polynomial has RMS value over the unit circle equal to one. They form a set of orthogonal polynomials, and it's convenient to write them as a function of ρ and θ:

$$\begin{aligned} Z_{j,even} &= \sqrt{n+1}R_n^m(\rho)\sqrt{2}\cos m\theta, for\ m \neq 0 \\ Z_{j,odd} &= \sqrt{n+1}R_n^m(\rho)\sqrt{2}\sin m\theta, for\ m \neq 0 \\ Z_j &= \sqrt{n+1}R_n^0(\rho), for\ m = 0 \end{aligned} \tag{A.1}$$

where:

$$R_n^m(\rho) = \sum_{s=0}^{\frac{n-m}{2}} \frac{(-1)^s(n-s)!}{s!(\frac{n+m}{2}-s)!(\frac{n-m}{2}-s)!}\rho^{n-2s} \tag{A.2}$$

The values of n and m are always integer and satisfy $m \leq n$, $n-|m| = even$. The index j is a mode ordering number and is a function of n and m. This ordering is convenient, and allows to write the orthogonality relation in this fashion[25]:

$$\int d^2\rho W(\rho) Z_j Z_{j'} = \delta_{j,j'} \tag{A.3}$$

where

$$\begin{aligned} W(\rho) &= 1/\pi \ \ \rho \leq 1 \\ W(\rho) &= 0 \ \ \rho > 1 \end{aligned} \tag{A.4}$$

The polynomial expansion of an arbitrary wavefront $W(\rho, \theta)$ over the unit circle is defined as:

$$W(\rho, \theta) = \sum_{i=1}^{\infty} a_i Z_i(\rho, \theta) \tag{A.5}$$

and the coefficients a_i, using the orthogonality (Equation A.3), are given by:

$$a_i = \int_{aperture} W(\rho, \theta) Z_i(\rho, \theta) \rho d\rho d\theta \tag{A.6}$$

Polynomial	Denomination
1	Piston
$\sqrt{4} r \cos\theta$	Tilt
$\sqrt{4} r \sin\theta$	Tilt
$\sqrt{3}\left(2r^2 - 1\right)$	Defocus
$\sqrt{6}\left(r^2 \sin 2\theta\right)$	Astigmatism
$\sqrt{6}\left(r^2 \cos 2\theta\right)$	Astigmatism
$\sqrt{8}\left(3r^3 - 2r\right)\sin\theta$	Coma
$\sqrt{8}\left(3r^3 - 2r\right)\cos\theta$	Coma
$\sqrt{8} r^3 \sin 3\theta$	Trifoil
$\sqrt{8} r^3 \cos 3\theta$	Trifoil
$\sqrt{5}\left(6r^4 - 6r^2 + 1\right)$	Spherical aberration

Tabella A.1: Zernike polynomials [convention from [44]].

It is possible to write these polynomials with a recurrence relation [16]:

$$k_1 R_{n+2}^m(\rho) = (k_2 \rho^2 + k_3) R_n^m(\rho) + k_4 R_{n-2}^m(\rho) \tag{A.7}$$

where

$$\begin{aligned} k_1 &= 2n(\frac{n+m}{2} + 1)(\frac{n-m}{2} + 1) \\ k_2 &= 2n(n+1)(n+2) \\ k_3 &= -m^2(n+1) - n(n+1)(n+2) \\ k_4 &= -2(\frac{n+m}{2})(\frac{n-m}{2})(n+2) \end{aligned} \tag{A.8}$$

Derivatives of Zernike polynomials can be useful whenever the gradient of a wavefront is required. Again a recurrence relation exists:

$$d_1(\rho) \frac{d}{d\rho} R_n^m(\rho) = d_2(\rho) R_n^m(\rho) + d_3(\rho) R_{n-2}^m(\rho) \tag{A.9}$$

where

$$
\begin{aligned}
d_1(\rho) &= n\rho(\rho^2 - 1) \\
d_2(\rho) &= nm(\rho^2 - 1) + (\frac{n-m}{2})[m + n(2\rho^2 - 1)] \\
d_3(\rho) &= -2(\frac{n+m}{2})(\frac{n-m}{2})
\end{aligned}
\tag{A.10}
$$

The convenience of the Zernike polynomials lies in the property that, following from the Kolmogorov statistics, one can determine individually the power in every single mode like tip-tilt, astigmatism or coma. One can then immediately calculate the residual aberration after correcting a specified number of modes with an adaptive optics system [9]. Another advantage of Zernike polynomials as a basis is not only that results can be obtained in a closed form, but also that the first few modes represent the classical aberrations familiar to opticians.

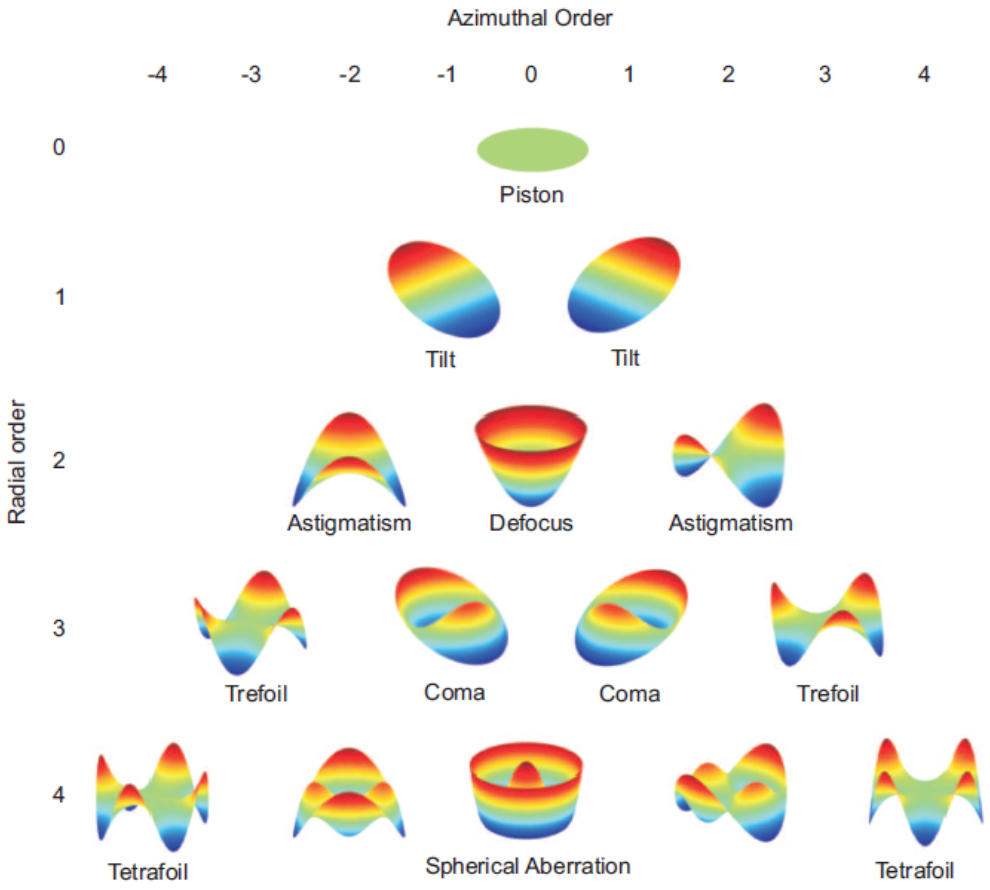

Figura A.1: Zernike polynomials ranked according to their azimuthal and radial orders [1].

Appendice B

Singular Value Decomposition and Pseudo-inverse

This appendix is mainly based on [36, 442 - 451].

B.1 Introduction to SVD

The *Singular Value Decomposition* (SVD) is a particular matrix factorization with many and growing applications. The SVD is closely associated with the eigenvalue - eigenvector factorization of a symmetric matrix: $A = Q\Lambda Q^T$. The following results are valid only if the matrix is *hermitian positive definite* [18]. The eigenvalues are in the diagonal matrix Λ, and the eigenvector matrix is *orthogonal*: $Q^TQ = I$, because eigenvectors of a symmetric matrix could be chosen orthonormal. If we allow Q on the left and Q^T on the right to be *any two orthogonal matrices* -not necessarily transposed of each other- the factorization becomes possible also with rectangular matrices. Furthermore, the diagonal (but rectangular) matrix in the middle can be made non-negative. It will be denoted by Σ, and its positive entries will be $\sigma_1, ..., \sigma_r$: they are the *singular values* of A. They fill the first r values on the main diagonal of σ, where r is the rank of A.

Singular Value Decomposition: any m by n matrix A can be factored into

$$A = Q_1\Sigma Q_2^T = (orthogonal)(diagonal)(orthogonal) \tag{B.1}$$

The columns of Q_1 (m by m) are eigenvectors of AA^T, and the columns of Q_2 (n by n) are eigenvectors of A^TA. The r singular values on the diagonal of Σ (m by n) are the square roots of the nonzero eigenvalues of both AA^T and A^TA.
The SVD is terrific for numerically stable computations, but Σ reveals exactly what is large and what is small in a very easy way: that's one reason of the popularity of this factorization with some important consequences discussed below with some examples.

B.2 Applications of the SVD

Few of the main applications of the SVD algorithm are here described. These examples are useful to really understand the importance of this algorithm and its potentialities. The most

important SVD application for us, that is the calculation of the pseudo-inverse, is discussed in Section B.3.

B.2.1 Image processing

If a satellite takes a picture, containing 1000 by 1000 pixels, after coding the colors in a range between black and white, it has to send back to Earth 1000000 numbers. It's better to find and send only the fundamental information.
The keys are the singular values in Σ (from SVD). Typically some are significant and others are extremely small. We can i.e. keep 60 singular values and throw away 940, then we send only the corresponding 60 columns of Q_1 and Q_2: the other columns are ignored. We can write the relation in this fashion:

$$Q_1 \Sigma Q_2^T = u_1\sigma_1 v_1^T + u_2\sigma_2 v_2^T + ... + u_r\sigma_r v_r^T \tag{B.2}$$

where u_i is a column of Q_1 and v_i is a column of Q_2(so v_1^T is the first row of Q_2^T). Any matrix can be written as the sum of r matrices of rank one. If only 60 terms are kept, we send 60 times 2000 numbers instead of a million.
The more and more singular values are included, the pictures become really striking: at first we see nothing, suddenly we recognize everything.

B.2.2 Rank

By definition, the rank of a matrix is the number of independent rows (or equivalently columns) in a matrix. This is not easy to determine in computation, and i.e. the method of pivots counting is correct only in exact arithmetic.
A more stable method is based on A^TA or AA^T matrices. They have the same rank as A and their singular values are not misleading. The number of singular values above a certain tolerance (based on the accuracy of the data), is the effective rank of the matrix.

B.2.3 Modal Analysis

We suppose that we know the Frequency Response Functions (FRF) of a structure, sampled in N_p spatial points and for N_f frequencies [22]. We can build the following matrix:

$$[H]_{N_f x N_p} = [H_{1k}, H_{2k}, .., H_{N_p k}] \tag{B.3}$$

Applying the SVD to this matrix:

$$[H] = [Q_1]_{N_f \times N_f} \cdot [\Sigma]_{N_f \times N_p} \cdot [V]^T_{N_p \times N_p} \tag{B.4}$$

We can get information about the system from these matrices.
The non-zero singular values in Σ are the number of vibration modes inside our frequency range of study.
The columns of Q_1 contain information on the frequency distribution of these amplitudes.
The columns of Q_2 contain the spatial distribution of amplitudes.

With the SVD decomposition it's possible to define other quantities.

The Principal Response Function (PRF) is:

$$[PRF]_{N_f \times N_p} = [Q_1]_{N_f \times N_f} \cdot [\Sigma]_{N_f \times N_p} \tag{B.5}$$

The columns of PRF contain the same information of FRF, but with some advantages. In fact, plotting these data, two different families of curves stand out (see Figure B.1): the upper ones contain information about the response, the lower ones about the noise level. If the two groups of curves are not well separated, it means that the noise level in the measurement system is too high.

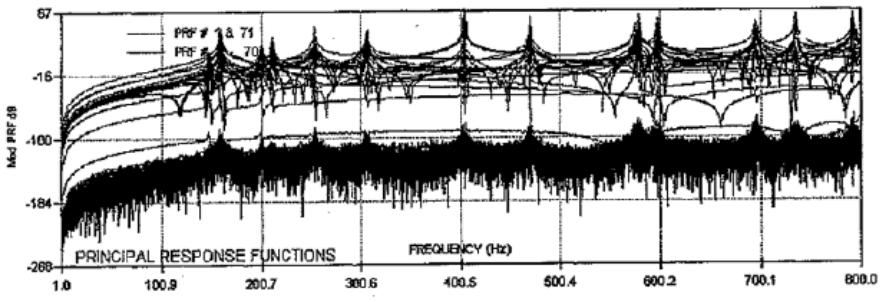

Figura B.1: The two families of curves obtained with the PRF [simulated data [22]].

Other applications of the SVD decomposition are possible and well known. We can recall the Complex Mode Indicator Function (CMIF), useful for detecting coupled vibration modes in MIMO symmetrical structures.

B.3 The pseudo-inverse matrix

The pseudo-inverse matrix is a generalized kind of inverse matrix but applied to rectangular matrices. For a given inconsistent system $Ax = b$, with n unknowns and m equations (so A is a rectangular matrix of (m, n) dimensions), it is possible to reach a (least squares) solution doing:

$$A^T A\bar{x} = A^T b \tag{B.6}$$

If the columns of A are linearly independent, then $A^T A$ is invertible and

$$\bar{x}^+ = (A^T A)^{-1} A^T b = A^+ b. \tag{B.7}$$

The A^+ matrix is called the pseudo-inverse of A and it is possible to demonstrate that it allows to find the optimal solution x^+ to the problem above. The optimal, best approximate solution in this case means that $\bar{x}^+$ minimizes the Euclidean norm $||Ax - b||$ [4].

B.4 Pseudo-inverse matrix and SVD

Suppose that the singular value decomposition of A is $A = Q_1 \Sigma Q_2^T$. Then the pseudoinverse of A is:

$$A^+ = Q_2 \Sigma^+ Q_1^T \tag{B.8}$$

The singular values $\sigma_1, ..., \sigma_r$ are on the diagonal of Σ (m by n), and the reciprocals $1/\sigma_1, ..., 1/\sigma_r$ are on the diagonal of Σ^+ (n by m). The pseudo-inverse of A^+ is $A^{++} = A$.

Appendice C

Piezoelectric systems

This section is mostly based on [28] and [29].

Piezoelectric materials belong to the so-called *smart materials*, or *multi-functional materials*, which have the ability to respond significantly to stimuli of different physical natures. Figure C.1 lists various effects that are observed in materials in response to various inputs: mechanical, electrical, magnetic, thermal, light. The coupling between the physical fields of different types is expressed by the non-diagonal cells in the figure; if its magnitude is sufficient, the coupling can be used to build discrete or distributed transducers of various types, which can be used as sensors, actuators, or even integrated in structures with various degrees of tailoring and complexity (e.g. as fibers), to make them controllable or responsive to their environment (e.g. for shape morphing, precision shape control, damage detection, dynamic response alleviation,...). The direct piezoelectric effect consists in the possibility, for certain crystalline

Output / Input	Strain	Electric charge	Magnetic flux	Temperature	Light
Stress	Elasticity	Piezo-electricity	Magneto-striction		Photo-elasticity
Electric field	Piezo-electricity	Permittivity			Electro -optic effect
Magnetic field	Magneto-striction	Magneto-electric effect	Permeability		Magneto -optic
Heat	Thermal expansion	Pyro-electricity		Specific heat	
Light	Photostriction	Photo-voltaic effect			Refractive index

Figura C.1: Stimulus-Response relations indicating various effects in materials. The smart materials correspond to the non-diagonal cells [28].

materials, to generate an electric charge in proportion to an externally applied force: this effect is used in the transducers. A coupled effect, the inverse one, determines that an external

electric charge generates a force. The piezoelectric effect is anisotropic and can be exhibited only by materials whose crystalline structure has no center of symmetry. It is the case of certain ceramic materials below the so-called *Curie temperature*. In this phase, built-in electrical dipoles are present in the structure, but randomly oriented, that is with a net electric dipole on a macroscopic scale equal to zero. During the poling process, when the crystal is cooled in the presence of a high electric field, the dipoles tend to align, leading to an electric dipole on a macroscopic scale. After cooling and removing of the poling field, the dipoles cannot return to their original position; they remain aligned along the poling direction and the material body becomes permanently piezoelectric, with the ability to convert mechanical energy into electrical energy and vice versa [28]. If the operation temperature exceeds the Curie temperature, or the electric field applied to the transducer in the direction opposed to the poling field is exaggerated, this property will be decayed.
The most popular piezoelectric materials are *Lead-Zirconate-Titanate* (PZT) which is a ceramic, and *Polyvinylidene fluoride* (PVDF) which is a polymer. In addition to the piezoelectric effect, piezoelectric materials exhibit a pyroelectric effect, according to which electric charges are generated when the material is subjected to temperature.

This appendix deals with the analysis of piezoelectric transducers, starting with a one-dimensional discrete one and then switching to piezoelectric laminates.

C.1 Piezoelectric transducer

A transducer made of a one-dimensional piezoelectric material is analyzed here. The constitutive equations are:

$$\begin{aligned} D &= \epsilon^T E + d_{33} T \\ S &= d_{33} E + s^E T \end{aligned} \tag{C.1}$$

where D is the electric displacement (charge per unit area, expressed in $Coulomb/m^2$), E the electric field (V/m), T the stress (N/m^2) and S the strain. ϵ^T is the dielectric constant (permittivity) under constant stress, s^E is the compliance when the electric field is constant (inverse of the Young's modulus) and d_{33} is the piezoelectric constant, expressed in m/V or $Coulomb/Newton$. The reason for the subscript 33 is that, by convention, index 3 is always aligned to the poling direction of the material, and we assume that the electric field is parallel to the poling direction. In general, for the three-dimensional case, the meaning of the subscripts of the constant d_{ij} is: i represent the direction in which the electric field is applied, j is the direction in which the deformation is induced in the material.

It's possible to write the above relations in a more compact way, using matrix notation:

$$\begin{Bmatrix} D \\ S \end{Bmatrix} = \begin{bmatrix} \epsilon^T & d_{33} \\ d_{33} & s^E \end{bmatrix} \begin{Bmatrix} E \\ T \end{Bmatrix} \tag{C.2}$$

where (E,T) are the independent variables and (D,S) are the dependent variables. If (E,S) are taken as the independent variables, we can rewrite:

$$\begin{Bmatrix} D \\ T \end{Bmatrix} = \begin{bmatrix} \epsilon^T(1-k^2) & e_{33} \\ -e_{33} & c^E \end{bmatrix} \begin{Bmatrix} E \\ S \end{Bmatrix} \tag{C.3}$$

where $c^E = 1/s^E$ is the Young's modulus under $E = 0$ (short circuited electrodes), in N/m^2 (Pa); $e_{33} = d_{33}/s^E$, product of d_{33} by the Young modulus, is the constant relating the electric displacement to the strain for short-circuited electrodes (in $Coulomb/m^2$), and also that relating the compressive stress to the electric field when the transducer is blocked ($S = 0$).

$$k^2 = \frac{d_{33}^2}{s^E \epsilon^T} = \frac{e_{33}^2}{c^E \epsilon^T} \tag{C.4}$$

k is the so-called *electromechanical coupling factor* of the material; it measures the efficiency of the conversion of mechanical energy into electrical energy, and vice-versa [28]. Let us assume

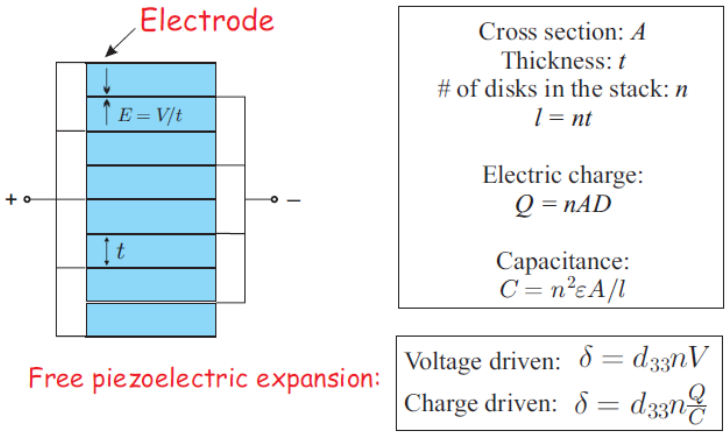

Figura C.2: Piezoelectric linear transducer, with the main parameter specified to the side [29].

a linear transducer formed by a stack of a n disks of thickness t and cross-section A, with all the mechanical and electrical properties uniformly distributed. The constitutive relations are now:

$$\begin{Bmatrix} Q \\ f \end{Bmatrix} = \begin{bmatrix} C(1-k^2) & nd_{33}K_a \\ -nd_{33}K_a & K_a \end{bmatrix} \begin{Bmatrix} V \\ \Delta \end{Bmatrix} \tag{C.5}$$

where $Q = nAD$ is the total electric charge on the electrodes of the transducer, $\Delta = Sl$ is the total extension ($l = nt$ is the length of the transducer), $f = AT$ is the total force and V the voltage applied between the electrodes of the transducer, resulting in an electric field $E = V/t = nV/l$. $C = \epsilon^T An^2/l$ is the capacitance of the transducer with no external load ($f = 0$), $K_a = A/s^E l$ is the stiffness with short-circuited electrodes ($V = 0$) [29].

C.2 Piezoelectric laminates

Let us consider a two-dimensional piezoelectric laminate in a plane (x, y): the poling direction z is normal to the laminate and the electric field is also applied along z. In the piezoelectric orthotropy axes, the constitutive equations are:

$$\{Q\} = [c]\{S\} - \begin{Bmatrix} e_{31} \\ e_{32} \\ 0 \end{Bmatrix} E_3 \tag{C.6}$$

$$D_3 = \{e_{31} e_{32} 0\}\{S\} + \epsilon E_3 \tag{C.7}$$

where

$$T = \begin{Bmatrix} T_{11} \\ T_{22} \\ T_{12} \end{Bmatrix} \tag{C.8}$$

and

$$S = \begin{Bmatrix} S_{11} \\ S_{22} \\ S_{12} \end{Bmatrix} = \begin{Bmatrix} \partial u/\partial x \\ \partial v/\partial y \\ \partial u/\partial y + \partial v/\partial x. \end{Bmatrix} \tag{C.9}$$

are respectively the stress and strain vectors, $[c]$ is the matrix of elastic constants under constant electric field, E_3 is the component of the electric field along z, D_3 is the z component of the electric displacement and ϵ the dielectric constant under constant strain ϵ^S.

Let us now recall the stiffness matrix of a multi-layer elastic laminate. Considering $[c]_k$ the

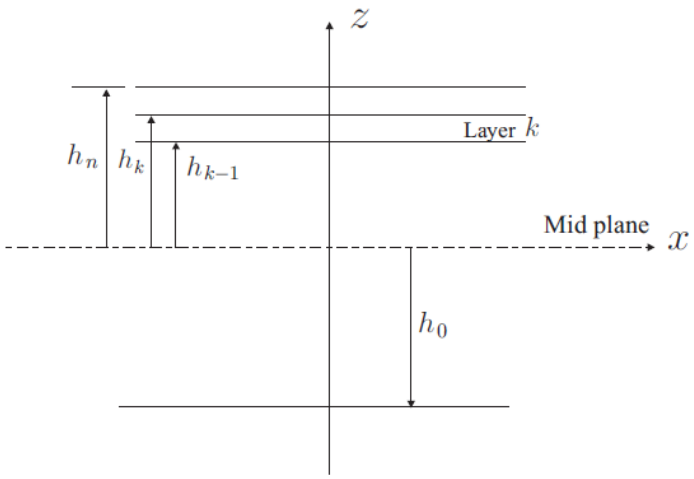

Figura C.3: Geometry of a multilayered laminate [28].

stiffness matrix of the material of the layer k, expressed in global coordinates, the constitutive equation within layer k is:

$$\{T\} = [c]_k \{S^0\} + z[c]_k \{\kappa\} \tag{C.10}$$

By integrating over the thickness of the laminate, one gets:

$$\begin{Bmatrix} N \\ M \end{Bmatrix} = \begin{bmatrix} A & B \\ B & D \end{bmatrix} \begin{Bmatrix} S^0 \\ \kappa \end{Bmatrix} \tag{C.11}$$

where A is the extensional stiffness matrix relating the in-plane resultant forces to the midplane strains; D is the bending stiffness matrix relating the moments to the curvature and B is the coupling stiffness matrix, which introduces coupling between bending and extension in the laminated plate[1].

A multi-layer laminate with **a single piezoelectric layer** of thickness h_p is now considered. Upon integrating over the thickness and assuming that the global axes coincide with the

[1]These coefficient are summations over the n layers of material: each layer contributes with its characteristic stiffness matrix. See [28] for details.

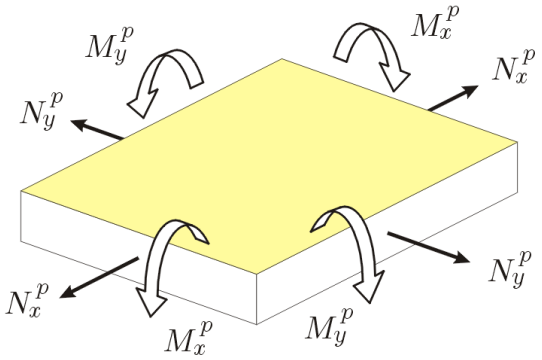

Figura C.4: Resultant forces and moments [2].

orthotropy axes of the piezoelectric layer, and further considering no external loads (N and M vanish), one can get:

$$\begin{bmatrix} A & B \\ B & D \end{bmatrix} \begin{Bmatrix} S^0 \\ k \end{Bmatrix} = - \begin{bmatrix} I_3 \\ z_m I_3 \end{bmatrix} \begin{Bmatrix} e_{31} \\ e_{32} \\ 0 \end{Bmatrix} V \tag{C.12}$$

where V is the difference of potential between the electrodes of the piezoelectric layer ($E_3 = -V/h_p$), z_m is the distance between the midplane of the piezoelectric layer and the midplane of the laminated; I_3 is the unity matrix of rank 3. The right hand side are the equivalent piezoelectric loads. If the material is isotropic, $e_{31} = e_{32}$, and the equivalent piezoelectric loads are hydrostatic (i.e. they are independent of the orientation of the facet within the part covered by the electrode). Overall, they consist of an in-plane force normal to the contour of the electrode, and a constant moment acting on the contour of the electrode (Figure C.5); the force per unit length and moment per unit length are respectively [28]:

$$N_p = -e_{31} V \tag{C.13}$$

$$M_p = -e_{31} z_m V \tag{C.14}$$

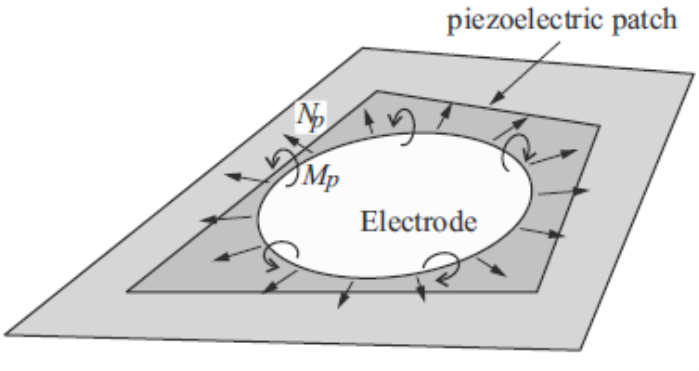

Figura C.5: Equivalent piezoelectric loads [28].

General Bibliography

[1] R. Bastaits. *Extremely Large Segmented Mirrors: Dynamics, Control and Scale Effects.* PhD thesis, Active Structures Laboratory - Université Libre de Bruxelles, June 2010.

[2] R. Bastaits and al. Multi-layer adaptive thin shells for future space telescopes. *Smart Mater. Struct.*, 21, 2012.

[3] P. Y. Bely. *The Design and Construction of Large Optical Telescopes.* Springer, 2003.

[4] F. J. Beutler. The operator theory of pseudo-inverse. *Journal of mathematical analysis and applications*, 10:451–470, 1965.

[5] R. D. Blevins. *Formulas for Natural Frequency and Mode Shapes.* Krieger Publishing Company, 1979.

[6] California Institute of Technology. California Extremely Large Telescope : conceptual design for a thirty-meter telescope. Technical report, 2002. URL `http://celt.ucolick.org/reports/greenbook.pdf`.

[7] ESO. *OWL Concept Design Report - Phase A design report.* European SOuthern Observatory, 2004.

[8] L. B. Freund and S. Suresh. *Thin Film Materials: Stress, Defect Formation and Surface Evolution.* Cambridge University Press, 2003.

[9] A. Glindemann, S. Hippler, T. Berkefeld, and W. Hackenberg. Adaptive optics on large telescopes. *Experimental Astronomy*, 10(1):5–47, 2000.

[10] GMT. The Giant Magellan Telescope website, 2010. URL `{http://www.gmt.org/}`.

[11] R. Hamelinck. *Adaptive Deformable Mirror based on Electromagnetic Actuators.* PhD thesis, Technische Universiteit Eindhoven, June 2010.

[12] J. W. Hardy. *Adaptive Optics for Astronomical Telescopes.* Oxford University Press, 1998.

[13] M. A. Helmbrecht, M. He, T. Juneau, M. Hart, and N. Doble. Segmented mems deformable-mirror for wavefront correction. *Proc. SPIE*, 6376:63760D–63760D–9.

[14] P. Hickson. *Fundamentals of Atmospheric Adaptive Optics.* Unpublished seminar support, 2008.

[15] R. C. et al Jared. W. m. keck telescope segmented primary mirror active control system. July 1990.

[16] E. C. Kintner. On the mathematical properties of the zernike polynomials. *Optical Acta: International Journal of Optics*, 23(8):679–680, 1976.

[17] A. N. Kolmogorov. A refinement of previous hypotheses concerning the local structure of turbulence in a viscous incompressible fluid at high reynolds number. *Handbook of Optics: Fundamentals, techniques, and design - Volume 1 - Chapter 35*, 1961.

[18] S. Lilliu. Algoritmi per la reglarizzazione e il calcolo della SVD - Implementazione e benchmark comparativi, March 2007.

[19] A. E. Long and C. A. Long. Surface approximation and interpolation via matrix svd. *The College Mathematics Journal*, 32, 2001.

[20] P.Y. Madec. Overview of deformable mirror technologies for adaptive optics and astronomy. *Proc. SPIE*, 8447:844705–844705–18, 2012.

[21] D. Malacara. *Optical Shop Testing*. Wiley, 1992.

[22] S. Manzoni. Slides of the course Tecniche di misura avanzate. *Politecnico di Milano*, 2012.

[23] C. Max. Introduction to adaptive optics and its history. 2011.

[24] J.; Kissler-Patig M.; Ramsay S.; Brunetto E.; Dierickx P.; Cassali M. McPherson, A.; Spyromilio. E-ELT update of project and effect of change to 39m design. In *Proceedings - SPIE The Internatinal Society for Optical Engineering 8444; 8444 1F*, 2012.

[25] R. J. Noll. Zernike polynomials and atmospheric turbulence. *Optical Society of America, Journal*, 66:207–211, 1976.

[26] Optical Technologies. What is an optic surface figure?, August 28,2008. URL `http://optical-technologies.info/tag/peak-to-valley-vs-rms/`.

[27] V. Piefort. *Finite Element Modeling of Piezoelectric Active Structures*. 2001.

[28] A. Preumont. *Mechatronics Dynamics of Electromechanical and Piezoelectric Systems*. Springer, 2006.

[29] A. Preumont. *Vibration Control of Active Structures: An Introduction - 3rd edition*. Springer, 2011.

[30] G. Rodrigues. *Adaptive Optics with Segmented Deformable Bimorph Mirrors*. PhD thesis, Active Structures Laboratory - Université Libre de Bruxelles, February 2010.

[31] V. Sacek. Telescope Optics, 2010. URL `{http://www.telescope-optics.net/}`.

[32] D.J. Schroeder. *Astronomical Optics*. Academic Press, 2000.

[33] R. R. Shannon. Optical specifications. *Handbook of Optics: Fundamentals, techniques, and design - Volume 1 - Chapter 35*, 1, 1994.

[34] J. B. Stewart, T. G. Bifano, S. Cornelissen, and al. Design and development of a 331 segment tip tilt piston mirror array for space based adaptive optics. *Sensors and actuators A: Physical*, 138.

[35] G. G. Stoney. The tension of metallic films deposited by electrolysis. *Proceedings of the Royal Society*, May 1909.

[36] G. Strang. *Linear Algebra and its Applications*. Harcourt Brace Jovanovich, 1988.

[37] I. Surdej. *Co-phasing segmented mirrors: theory,laboratory experiments and measurements on sky*. PhD thesis, Fakultät für Physik der Ludwig Maximilians Universität, München, July 2011.

[38] TMT. The Thirty Meter Telescope website, 2010. URL `{http://www.tmt.org/}`.

[39] PAT TROTTA. The optical invariant. *Opt. Photon. News*, 5(7):56–56, Jul 1994. doi: 10.1364/OPN.5.7.000056. URL `http://www.osa-opn.org/abstract.cfm?URI=opn-5-7-56`.

[40] B. H. Walker. *Optical Engineering Fundamentals*. SPIE Press, 1998.

[41] R. N. Wilson. The History and Development of the ESO Active Optics System. *The Messenger*, 113:2–9, September 2003.

[42] R. N. Wilson, F. Franza, and L. Noethe. Active Optics I. A system for optimizing the optical quality and reducing the costs of large telescopes. *Journal of Modern Optics*, 34 (4):485–509, 1987.

[43] J. C. Wyant and K. Creath. Basic Wavefront Aberration Theory for Optical Metrology. In R. R. Shannon and J. C. Wyant, editors, *Applied Optics and Optical Engineering, Volume XI*, volume 11, 1992.

[44] Zemax Corp. *Zemax - Optical Design Program - User's Guide*. Zemax Corp., 2005.